

STRUCTURE AND FUNCTION OF BARTONELLA EFFECTOR PROTEIN 1: TARGET AND INTERDOMAIN INTERACTIONS

Inauguraldissertation

zur

Erlangung der Würde eines Doktors der Philosophie

vorgelegt der

Philosophisch-Naturwissenschaftlichen Fakultät

der Universität Basel

von

Markus Huber

2023

*Originaldokument gespeichert auf dem Dokumentenserver der Universität Basel
edoc.unibas.ch*

This work is licensed under a Creative Commons "Attribution-NonCommercial-ShareAlike 4.0 International" license.



Genehmigt von der Philosophisch-Naturwissenschaftlichen Fakultät auf Antrag
von

Prof. Dr. Christoph Dehio

Prof. Dr. Tilman Schirmer

Prof. Dr. Timm Maier

Prof. Dr. Gudula Schmidt

Basel, den 27. 04. 2021

Prof. Dr. Marcel Mayor

Dekan

Abstract

Abstract

Bartonella are gram-negative facultative intracellular pathogens that follow a stealth infection strategy, to persist in erythrocytes and thereby be ingested by bloodsucking arthropods that serve as vectors. To achieve this persistent infection, most *Bartonella* translocate effector proteins via the VirB4/D4 type IV secretion system into host cells, to modulate responses during their infection cycle.

The majority of *Bartonella* effector proteins (BEPs) is made up by a common domain arrangement, consisting of an essential C-terminal BID domain, carrying the type IV secretion signal, and an N-terminal FIC domain, that usually catalyzes post translational modifications of target proteins, most prominently the transfer of AMP, called AMPylation.

While knowledge about the Fic protein family has grown rapidly in the last decade, only targets for a few of its members could be identified so far.

In this study, I used structural and biophysical methods to characterize Bep1, that consists of the most abundant FIC and BID domain arrangement.

First, I analysed Bep1 from *B. rochalimae* and studied its exquisite target selectivity towards the Rac subfamily of Rho GTPases. For this purpose, I set up a new method for the quantification of AMPylation reactions, called online Ion Exchange Chromatography assay, and developed a python pipeline for automated data processing. I used kinetic studies in combination with mutagenesis to narrow interactions down to two crucial salt-bridges between Bep1 and its targets.

Second, I crystallized the full-length effector Bep1 from *B. clarridgeia* and could identify a fold at the C-terminus, that was previously described as unstructured tail. I was able to combine the structural analysis with hot-spots of sequence conservation, and found interactions that are critical for the shape of *Bartonella* effectors containing a Fic domain. These results might hint at a mechanism for an unfolding process necessary for translocation of these effectors through the T4SS.

Contents

Abstract	i
List of Tables	v
List of Figures	vii
1 Introduction	1
1.1 Rho GTPases	2
1.1.1 Rho GTPase as molecular switches	2
1.1.2 Regulation of Rho GTPases	4
1.1.3 Localization of GTPases	5
1.1.4 Rho GTPases and the cellular immune responses	6
1.1.5 GTPases are major targets for bacterial pathogens	6
1.2 <i>Bartonella</i>	9
1.2.1 Pathogenesis	9
1.2.2 Infection strategy and vector dependence	9
1.2.3 Type IV Secretion Systems as a host adaptability factor	10
1.2.4 Architecture of the T4SS	11
1.2.5 <i>Bartonella</i> effector proteins	13
1.3 BID domains	14
1.4 Fic Proteins	15
1.4.1 Fic structure and function	18
1.4.2 Regulation and classification of Fic proteins	18
1.4.3 Fic target interaction	21
2 Aim of the thesis	23
3 Results	25
3.1 Research article I	26
3.2 Research article II (in revision for Structure)	50

Contents

3.3	Unpublished Results	96
3.3.1	Implementation of a quantitative online AMPylation assay	96
3.3.2	Quantitative analysis of Bep1 mediated AMPylation	100
3.3.3	Bep1 interactions with GTPases in complex with their regulators	104
3.3.4	Methods	111
4	Discussion	119
4.1	The oIEC as new gold standard for AMPylation assays	120
4.2	Two intermolecular Salt bridges are crucial for Bep1-mediated target AMPylation	121
4.3	Secretion of Bep1 full-length requires partial unfolding	122
4.4	A novel fold (CB) structurally links FIC-OB and BID domains	122
4.5	Inhibition relieved anti-toxin could interfere with ATP exchange	123
4.6	Recruitment of GEFs by Beps could be a more general mechanism	123
5	References	125
6	Acknowledgments	149
7	Curriculum Vitae	151

List of Tables

1	Bacterial toxins interfering with GTPase signaling	7
2	Kinetic values for known AMPylators of GTPases	102
3	Bep1 catalyzed AMPylation efficiencies of target variants	104

List of Figures

1	Structure and function of Rho family GTPases	3
2	Multiple sequence alignment of Rho family GTPase	4
3	Regulatory cycle of Rho family GTPases	5
4	Rho GTPase toxins	6
5	Phylogenetic tree of the genus <i>Bartonella</i>	11
6	Architecture of the VirB/VirD4 T4SS	12
7	The VirB/D4 T4SS effector repertoire of <i>Bartonella</i> spp.	13
8	Structure of the BID domain	15
9	Filamentation induced by cAMP	15
10	Topology of selected FIC proteins from eukaryotes, procaryotes and viruses	16
11	Multiple sequence alignment of selected FIC proteins from eukaryotes, procaryotes and viruses	17
12	AMPylation mechanism and inhibition of AMPylation in FIC domain proteins	19
13	The Fic inhibitory motif and Fic classes	20
14	Sequence independent target-dock of Fic proteins	22
15	Phosphate Sensor assay controls	97
16	Separation of products and substrates during oIEC	99
17	oIEC data collection and processing	100
18	Side-reaction during AMPylation assays	101
19	Partial alignment of Bep1 homologs	101
20	Michaelis-Menten plots for the Bep1 _f catalyzed AMPylation of Rac1.	102
21	Bep1 _f catalyzed AMPylation efficiencies of target variants	103
22	Structure model of a potential GTPase-GDI-Bep1 complex	105
23	Partial alignment of RhoGDI-1 from mammalian species	106
24	Purification of Rac1-RhoGDI complex	107
25	Whole protein mass spectrometry of Rac1-RhoGDI complex	107

List of Figures

26	Efficiency of Rac1-GDI complex AMPylation catalyzed by Bep1 . . .	108
27	Structure model of a potential GTPase-GAP-Bep1 complex	109
28	Structure model of a potential GTPase-GEF-Bep1 complex	110
29	Partial alignment of GEF-H1 from mammalian species	110

1 Introduction

Introduction

Bacterial effector proteins are toxins that require an active transport into host cells via secretion systems. Their obvious advantage over exogenously administered toxins is a more controlled administration usually resulting in a more subtle interference with host functions [1].

Many bacterial pathogens have evolved mechanisms to interfere with host signaling through effector proteins thus enabling evasion from the host's innate immune response. Since small GTPases of the Rho family act as key regulators in many signaling pathways they are a major targeted of these toxins [2].

1.1 Rho GTPases

Small GTPases of the Rho (Ras homology) family are signaling proteins of about 21 to 25 kDa, that belong to the superfamily of Ras proteins. As Ras superfamily GTPases, Rho proteins contain the essential G-domain, that is necessary for the binding of GDP and GTP and for hydrolysis of the later. In addition to the core G-domain, Rho GTPases carry a C-terminal tail that is usually post translationally modified by isoprenylation. Furthermore, Rho proteins have a unique Rho insert helix (Figures 1A-B and 2) that distinguishes them from Ras family GTPases and is key for Rho specific signaling [3–13].

1.1.1 Rho GTPase as molecular switches

Rho GTPases are molecular switches that cycle through active GTP-bound ("ON") and inactive GDP-bound ("OFF") states (Figure 3). As such switches, they are usually turned "ON" through incoming extracellular signals to interact with downstream effector proteins, thus coordinating diverse cellular responses [3, 14].

Between the two activation states GTPases undergo major structural rearrangements in two particular regions called switch1 and switch2 (Figure 1). Switching between conformations changes the GTPases affinity for the interaction with effector proteins of their respective signaling pathway [5–8, 13].

Nucleotide binding is facilitated by 5 short GTPase specific fingerprint regions,

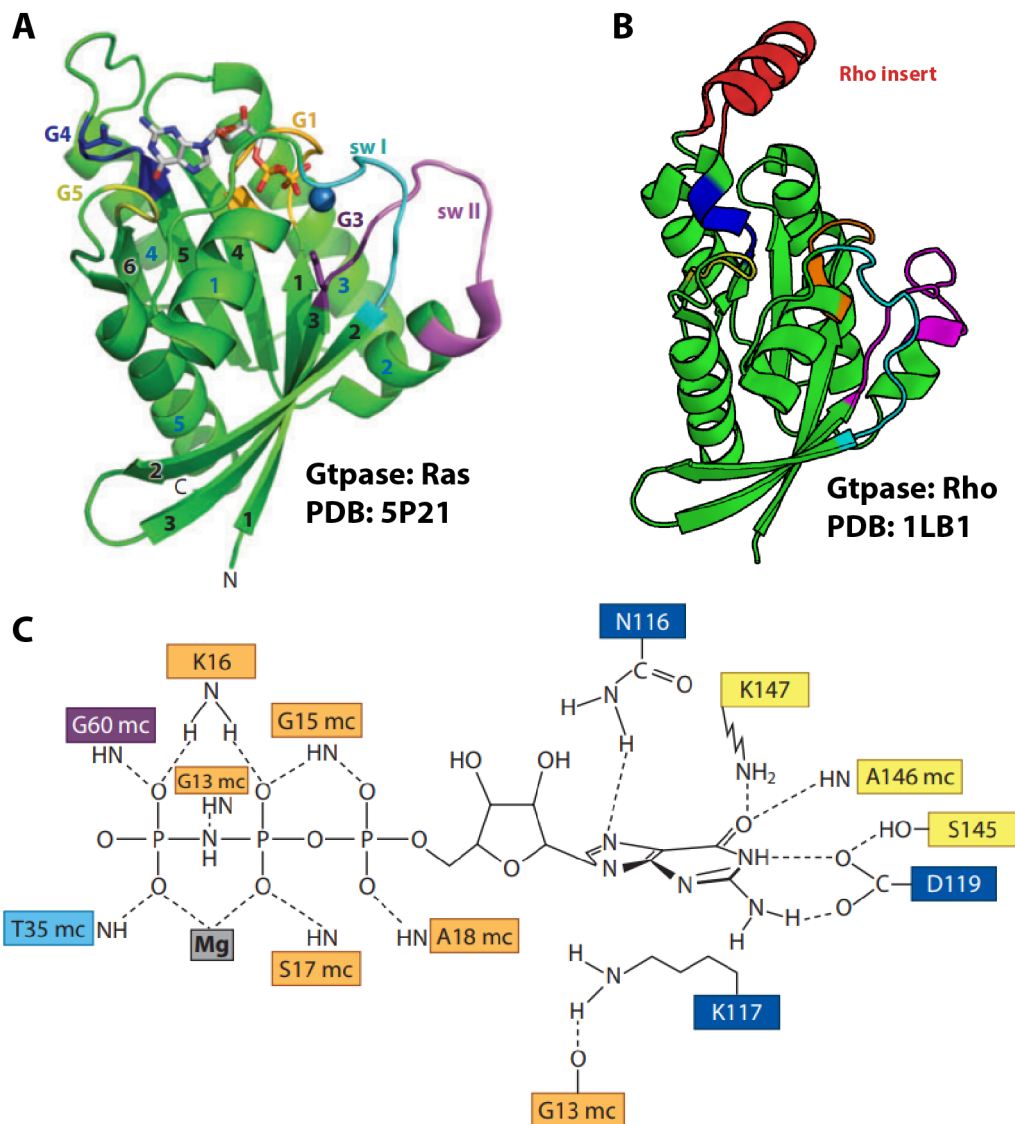


Figure 1: Structure and function of Rho family GTPases - (A) The globular fold of Ras superfamily GTPases consists of 6 *beta*-sheets and 5 *alpha*-helices (black and blue digits, respectively). G-protein binding motifs (G1-G5), responsible for the binding of nucleotides, and conformational switches (sw1, sw2) are colored. Mg^{2+} is shown as blue sphere and locks in the GTP analog GppNHp. (B) The Rho insert helix, unique to Rho family GTPases, is shown in red. G motifs and switches are drawn matching the coloring scheme of (A). (C) Scheme of G-motif interactions with the adenine base and phosphates of the nucleotide as observed in PDB 5P21. Coloring is concurrent to the Ras/Rho models. (adapted from [13])

G1-G5, with G4-G5 involved in binding the adenine base and G1-G3 interacting with the phosphates. Since switch1 (G1) and switch2 (G2) are interacting with the

1 Introduction

γ -phosphate of the nucleotide, an exchange of GDP for GTP triggers the conformational change of these switches (Figures 1C and 2) [3–8, 13].

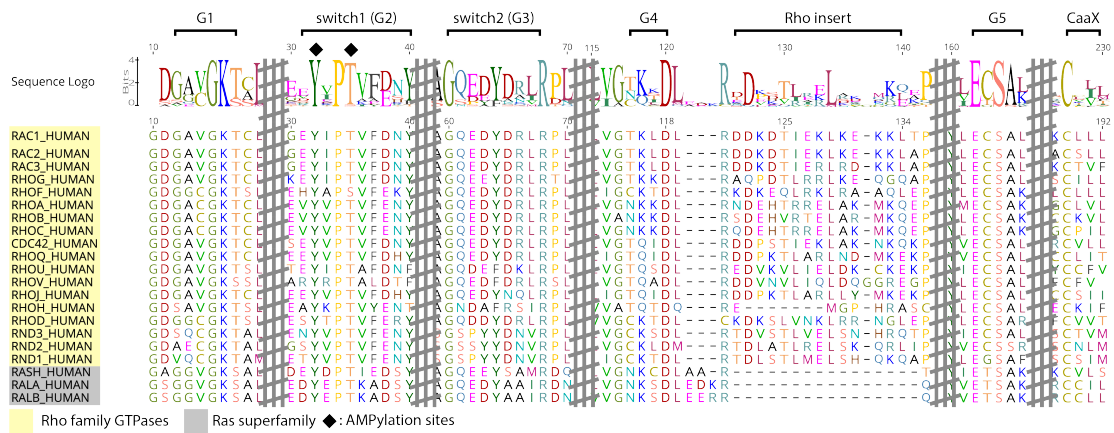


Figure 2: Multiple sequence alignment of Rho family GTPase - Multiple sequence alignment of human Rho family GTPases and 3 Ras superfamily GTPases for comparison. The G-nucleotide binding motifs, G1-G5, switch areas, the CaaX motif and the Rho insert helix are indicated.

1.1.2 Regulation of Rho GTPases

The G-domain has an intrinsic activity to hydrolyse GTP, that is catalyzed by GAPs (GTPase-accelerating proteins) and puts the GTPase in an "OFF"-state (Figure 3). For this purpose, GAPs stabilize the switch 1 and 2 regions and provide an arginine finger for proper positioning of the nucleotide to activate the GTP for a nucleophilic attack of a water molecule. [7, 13, 15].

To switch GTPases back into their "ON"-state, thus enabling them to interact with their downstream effectors, they depend on so called GEFs (Guanine nucleotide-exchange factors). GEFs destabilize the interaction between a critical magnesium ion and the GTPase, essentially breaking the "lock" that holds the nucleotide in place (Figures 1A and 3). The exchange of nucleotides is driven by diffusion and the molar ratio of GDP to GTP, which greatly favors GTP binding during physiological cell conditions [7, 8, 13, 16–18].

Another layer of GTPase regulation is facilitated by GDIs (Guanosine nucleotide dissociation inhibitors), that extract GTPases from membranes and solubilize them

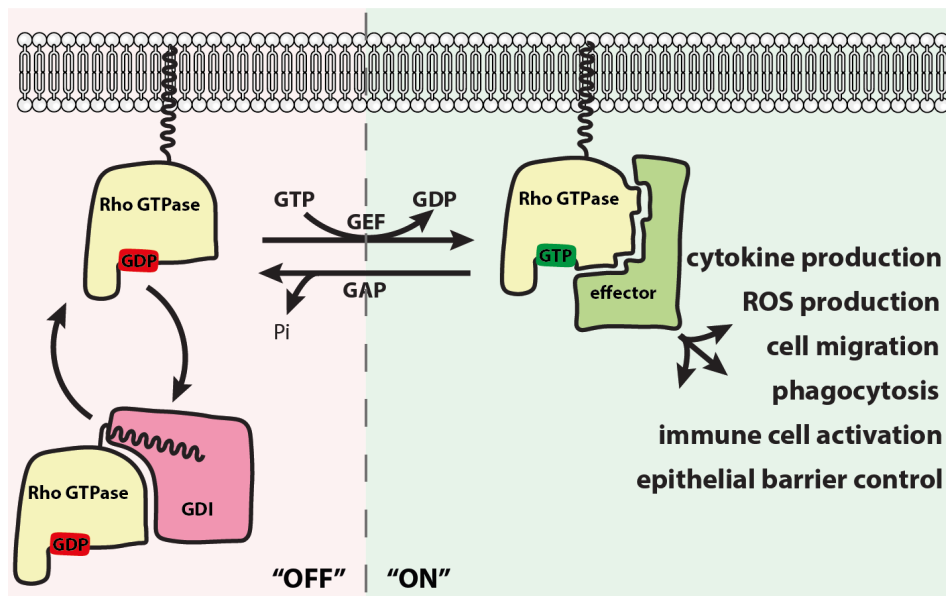


Figure 3: Regulatory cycle of Rho family GTPases - GTPases are drawn as yellow sketches with the isoprenyl-moiety in zigzag. Bound nucleotides are indicated in red (GDP) or green (GTP). GDIs and effectors are shown as sketch drawings (red and green, respectively). Nucleotide exchange and hydrolysis by GEFs and GAPs is drawn as arrows. Protuberances of GTPases indicate different switch conformations.

by shielding their isoprenyl moiety from the cytosol (Figure 3). GDI-complexed Rho-GTPases comprise the majority of GTPases and provide a GTPase depot and the means for shuttling of GTPases between cell membranes. [4, 13, 16, 17, 19]

1.1.3 Localization of GTPases

Although a majority of Rho GTPases is solubilized in an inactive state in the cytosol by GDIs, Rho GTPases exert their primary function at membranes and need to be localized accordingly, to relay signals to their downstream effectors.

For this purpose, the C-terminus of Rho GTPases is usually post-translationally isoprenylated with a geranylgeranyl moiety at the cysteine residue of a trailing CaaX motif (Cysteine-aliphatic-aliphatic-any amino acid). Isoprenylation is then followed by the cleavage of the last 3 residues "aaX". This multi-step modification is crucial for anchoring the GTPase to cell membranes. [3–13]

1.1.4 Rho GTPases and the cellular immune responses

Rho GTPases are involved in a great variety of cellular functions including cell migration, control of the epithelial barrier, phagocytosis, immune cell signaling, cytokine production, production of reactive oxygen species and they are well-known sensors for inflammation [20–34]. The most thoroughly studied representatives are the three main family branches Rho, Rac and Cdc42, that are best known for their involvement in the assembly of focal adhesions and actin stress fibre formation (Rho) [22], regulation of the formation of lamellipodia (Rac) [23] and their importance for polarized cell growth (Cdc42) [35].

Because Rho GTPases are important regulators of the cellular immune response and transduce incoming extracellular signals to downstream signaling pathways, they are a major target for pathogens, that strive to modulate these cellular functions to their advantage (Figure 4) [2, 3, 20, 36–38].

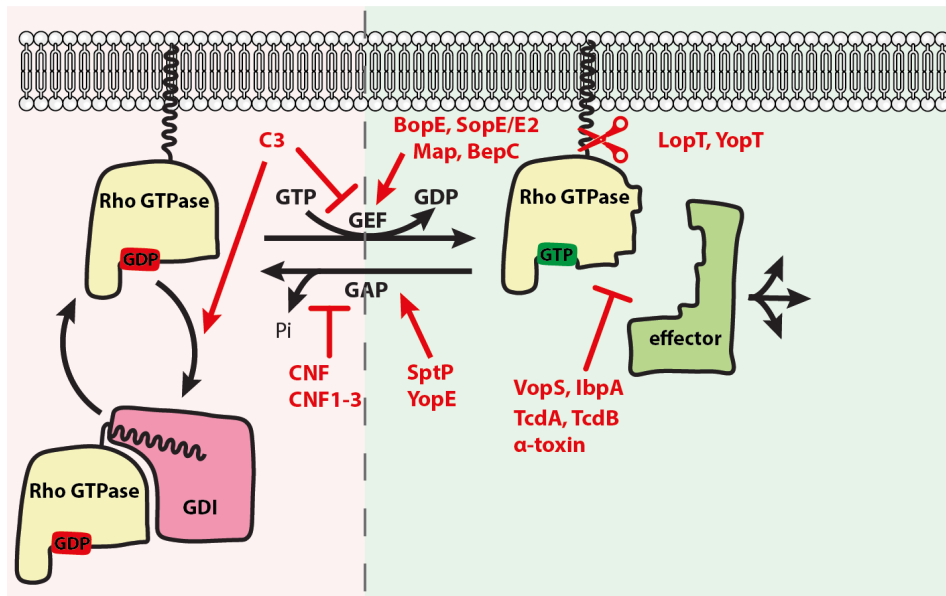


Figure 4: Rho GTPase toxins - Regulatory cycle of Rho family GTPases and toxins interfering with the cycle. Enhancing effects are shown as arrows. T-bars indicate inhibition of the respective function and scissors depict proteolysis.

1.1.5 GTPases are major targets for bacterial pathogens

Bacterial pathogens have found various ways on how to exploit GTPase cycles to their own benefit, including the activation [39–51] or deactivation [52–56] of

GTPases and the interference with effector proteins [56–61].

Although the physiological consequence of these modulations is in many cases similar, the underlying mechanisms are often quite different (Table 1 and Figure 4).

Table 1: Bacterial toxins interfering with GTPase signaling

Toxin action	Target GTPase	Organism	Toxin
<i>Activation of GTPases</i>			
GEF	Rac [*] , Cdc42	<i>B. pseudomallei</i>	BopE [39]
	Rac [*] , Cdc42	<i>S. enterica</i>	SopE, SopE2 [40, 41]
	Cdc42	<i>E. coli</i> (EHEC)	Map [42, 43]
GEF recruitment	RhoA	<i>Bartonella spp.</i> (L3)	BepC [44, 45]
Deamidation	RhoA	<i>Y. pseudotuberculosis</i>	CNF [46]
	Rho [*] , Rac [*] , Cdc42	<i>E. coli</i>	CNF1, CNF2, CNF3 [47–50]
<i>Deactivation of GTPases</i>			
ADP-ribosylation	RhoA, RhoB, RhoC	<i>C. botulinum</i>	C3 [52, 53]
		<i>C. limosum</i>	C3 [52, 53]
GAP	Rac [*] , Cdc42	<i>S. typhimurium</i>	SptP [54]
	Rho [*] , Rac [*] , Cdc42	<i>Y. pseudotuberculosis</i>	YopE [55, 56]
<i>Interference with effector binding</i>			
Proteolysis	Rho-family	<i>P. luminescens</i>	LopT [57]
	Rho-family	<i>Y. pseudotuberculosis</i>	YopT [56]
Glucosylation	Rho-family	<i>C. difficile</i>	TcdA, TcdB [58]
	Rho-family	<i>C. novyi</i>	α -toxin [59]
Adenylation	Rho-family	<i>H. somni</i>	IbpA [60]
	Rho-family	<i>V. parahaemolyticus</i>	VopS [61]

GTPases marked with * indicate targeting of the whole branch

Activation of GTPases in a GEF-like manner has been shown for BopE from *Burkholderia pseudomallei* and SopE/SopE2 from *Salmonella enterica* [39–41]. A similar mechanism of nucleotide exchange is facilitated by Map from enterohemorrhagic *E. coli* (EHEC) and other members of the family of WxxxE-effectors [42, 43].

A recently discovered bacterial effector of *Bartonella henselae*, BepC, recruits GEF-H1 and localizes it to the plasma membrane to modulate RhoA signaling,

1 Introduction

essentially hijacking the host cells regulatory system for its own advantage [44, 45].

CNF1-3 from *E. coli* have developed another mechanism to keep Rho GTPases in their active state. They convert a crucial glutamine to glutamate by deamidation and subsequently block GTP hydrolysis. The same mechanism is applied by CNF from *Yersinia pseudotuberculosis* [46–50].

Conversely, some toxins modulate the GTPase cycle to put their targets into their "OFF"-state. ADP-ribosylation of C3-like toxins from *Clostridium botulinum* and *Clostridium limosum* results in a reduced nucleotide exchange by GEFs and a tight binding to GDIs, effectively keeping the targets inactive [52, 62–66].

Other toxins, like SptP from *Salmonella typhimurium* and YopE from *Yersinia pseudotuberculosis*, mimic the GAP function by providing an arginine finger for rapid GTP hydrolysis and thus turn their targets "OFF" [55, 56].

A few bacterial toxins interfere with GTPases effector binding, instead of modulating the GTPase cycle. LopT from *Photobacterium luminescens* and YopT from *Yersinia pseudotuberculosis* indirectly interfere with effector interactions. Both toxins act as cysteine proteases, that proteolytically cleave the isoprenyl-moiety of their targets, thus dissociating them from the membrane [56, 57, 67].

TcdA/TcdB from *Clostridium difficile* modulates cell signaling in a more direct manner, by interfering with effector binding through glucosylation of a threonine residue in the switch1 region [58]. The same mechanism is applied by α -toxin from *Clostridium novyi* [59].

Interference with effector protein binding is also achieved by AMPylation of target hydroxyl side chains in the switch1 region, catalyzed by bacterial effectors IbpA from *Histophilus somni* and VopS from *Vibrio parahaemolyticus* [60, 61]. Recent findings have shown, that interference with the GTPase-effector interaction through AMPylation might be induced by steric clashes with the AMP-moiety directly, but could also be due to altered conformational GDP and GTP states for AMPylated Rho-proteins, compared to non-modified GTPases [68].

1.2 *Bartonella*

Bartonella spp. are gram-negative facultative intracellular pathogens. The first reports of *Bartonella* infections were from HIV patients in the 1980s [69] who developed cutaneous lesions that became later known as bacillary angiomatosis (BA) [70]. Subsequent isolation and study of BA-linked pathogens (at that time known as genus *Rochalimaea*) revealed their close genetic relationship to *B. bacilliformis* and led to the consolidation under the genus *Bartonella* [71–75].

1.2.1 Pathogenesis

Today numerous *Bartonella* species have been identified that can cause several diseases including BA, relapsing bacteremia, bacillary peliosis, endocarditis and urban trench fever [71, 72, 74, 76–78]. Nevertheless, *Bartonella* spp. are well adapted to their reservoir hosts (Figure 5) and cause a generally asymptomatic persistent infection of erythrocytes with reoccurring infection waves as their hallmark symptom in their respective hosts. [79–86].

Three *Bartonella* species, *B. quintana* (trench fever), *B. bacilliformis* (Carrion's disease) and *B. ancashensis* (isolated from patients with Verruga Peruana) are linked to human hosts today. However, coincidental infections with species not adapted to humans, like the zoonotic *B. henselae* (cat scratch disease), are well documented [86–90].

1.2.2 Infection strategy and vector dependence

Bartonellae are transmitted through blood-feeding arthropods (lice, fleas and ticks) or biting diptera (e.g. sand flies) either by direct blood contact or by inoculation from arthropod feces through skin lesions. Because the vector ecology has a major impact on the host specificity, more health concerning *Bartonella* species like *B. bacilliformis* have been confined to certain areas, although climate change might result in a further spread of these species in the future [91–93]. Thus, of clinical importance today are infections with *B. henselae* and re-emerging infections with *B. quintana* [76, 90, 94–96]

Once inside the host organism, *Bartonellae* have to reach their blood-seeding

1 Introduction

infection niche, most likely cells of the vascular endothelium [79–81, 97–102].

Migration is probably facilitated by infection of dendritic cells and subsequent transport [103], however there is also some evidence that lymphocytes or mononuclear phagocytes of the lymphatic system might play a role. [98, 104, 105]. Once *Bartonella* have infected the vascular endothelium, they are seeded into the blood stream in reoccurring waves, where they can re-infect their primary niche and infect and persist in erythrocytes. Infection and persistence in erythrocytes likely helps them to be taken up from their arthropod vectors [79–81, 101, 106, 107].

The persistent infection, requires the evasion of the immune system and as such a "stealth" infection strategy. This strategy is facilitated by the intervention of a repertoire of VirB/D4 T4SS-linked *Bartonella* effector proteins on various levels during host infection [80, 81, 108, 109].

1.2.3 Type IV Secretion Systems as a host adaptability factor

Bacterial T4SS are involved in bacterial conjugation, DNA uptake from and release to the extracellular milieu and the secretion of protein toxins. The ability to translocate bacterial effector proteins into host cells, allows pathogens to adapt host responses, that would otherwise be unfavourable to their colonization [111–114].

Almost all currently known *Bartonella* spp. acquired at least one type of Type IV secretion system (T4SS) during speciation events, the sole exception being *B. bacilliformis* [110, 115]. Phylogeny of *Bartonella* based on an alignment of 509 core genes from *Bartonella* and 5 rhizobial outgroup species, revealed 4 lineages of *Bartonella* radiating from a common ancestor (Figure 5) [108, 110]. This rapid radiation is attributed by no small measure to the uptake of type IV secretion systems, encompassing the Vbh and VirB/D4 T4SS, used for the translocation of effector proteins [81, 108, 116], and the Trw T4SS, that facilitates interactions with erythrocytes [108, 116, 117] exclusively in *Bartonella* spp. of lineage 4. However, the remarkably strong diversification and the high adaptability towards *Bartonella*'s mammalian hosts in lineages 3 and 4 is owed largely to the acquisition of the VirB/D4 secretion system. [81, 94, 108, 110, 115, 118]

Current knowledge suggests that there have been 3 independent horizontal events of VirB/D4 T4SS uptake and consequent diversification of the genus *Bartonella*

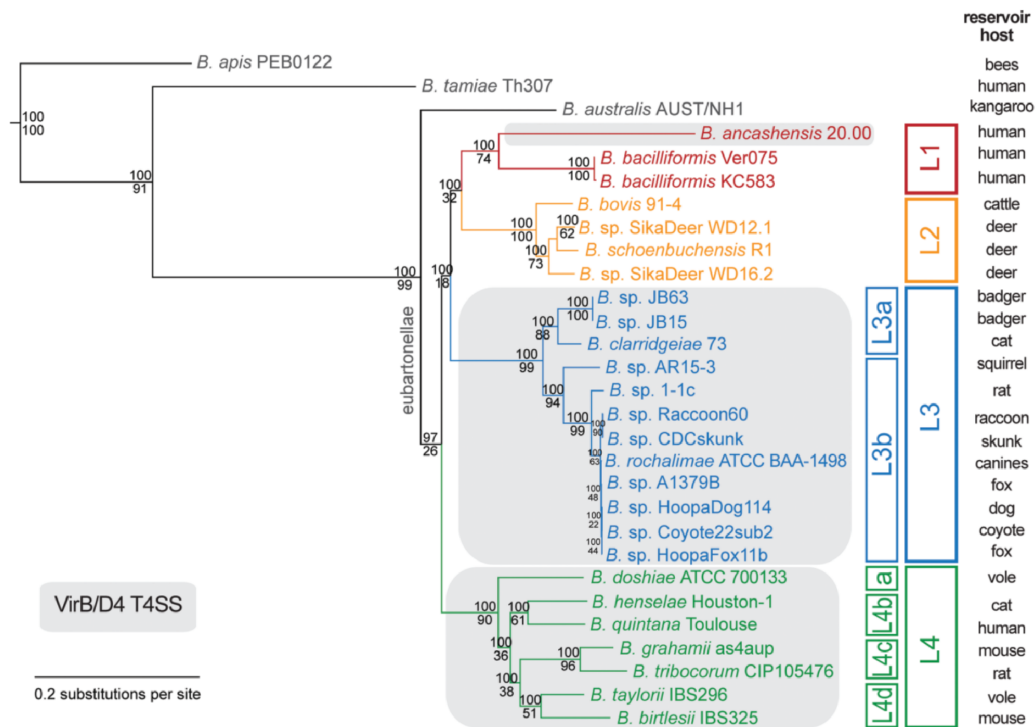


Figure 5: Phylogenetic tree of the genus *Bartonella* - Phylogenetic tree of *Bartonella*, based on an alignment of 509 core genes of *Bartonella* and 5 rhizobial outgroup species, with bootstrap and % support indicated as numbers at the top and bottom of the branches, respectively. Lineages, sublineages and respective reservoir hosts are indicated on the right. Species encoding the VirB/D4 T4SS are highlighted in grey. Note that *B. australis* couldn't be assigned to any of the 4 lineages. (taken from [110]).

[108, 110, 115]. The importance of the VirB/D4 T4SS as a pathogenesis factor has been shown by VirD4 and VirB4 deletion mutants in *B. tribocorum*, that were unable to cause intraerythrocytic bacteremia. [79, 116]

1.2.4 Architecture of the T4SS

The best understood type IV secretion system is the VirB/VirD4 T4SS from *Agrobacterium tumefaciens*, consisting of 11 VirB subunits that build up the envelope spanning core complex and the coupling protein VirD4, responsible for guiding and docking of effectors to the inner membrane pore (Figure 6).

VirB3, B6 and B8 are anchored in the inner membrane of the cell envelope and build a base for the stalk consisting of VirB7, VirB9 and VirB10. The stalk spans the periplasma and connects inner and outer membrane through a channel.

1 Introduction

A pilus formed by VirB2 and VirB5 is connected to VirB10 subunits, that also comprise the outer membrane core complex.

VirB1 is essential for assembly of the T4SS and for pilus formation, while VirB4 and VirB11, together with the coupling protein VirD4 are ATPases, that provide energy for the translocation of effectors. [119–123].

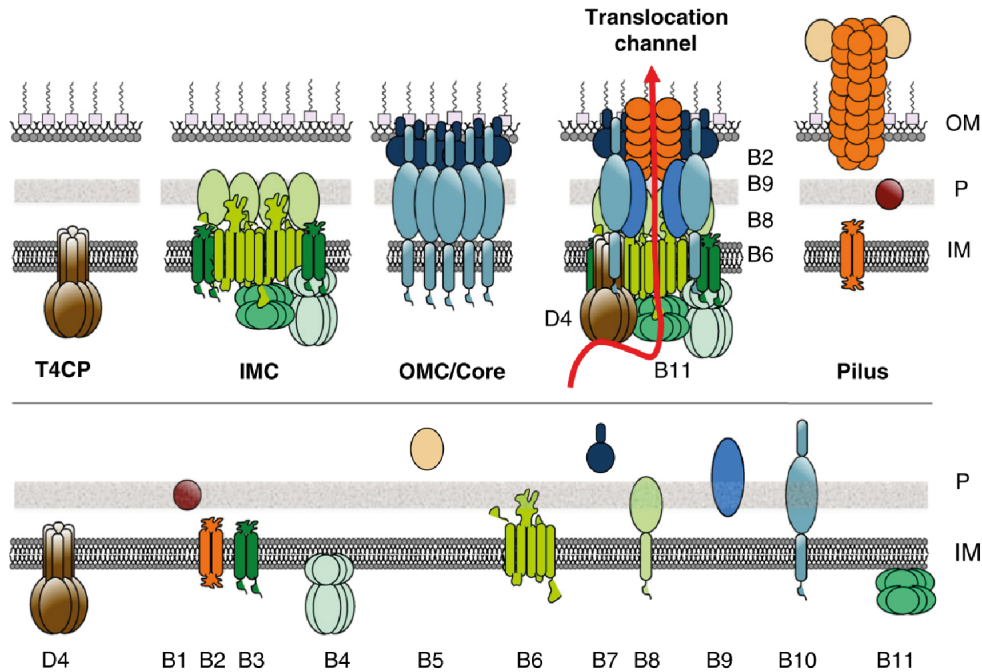


Figure 6: Architecture of the VirB/VirD4 T4SS - The 12 subunits of a typical VirB/D4 T4SS from *A. tumefaciens* are shown as schematics at the bottom. Symmetries and positions of the subunits in the inner membrane (IM), outer membrane (OM) or periplasma (P) are depicted at the top. The complete translocation channel comprises the type IV coupling protein (T4CP) VirD4, an inner membrane complex (ICM), an outer membrane complex (OMC) and the pilus. (taken from [123]).

Inner diameters for the translocation channel are known from structural analysis of the Trw T4SS from the conjugational plasmid R388 and show a 55 Å wide hole in the inner membrane that narrows down to 10 Å at the outer membrane opening. Rearrangements upon active secretion might increase the inner diameter, however it is apparent that T4SS effectors might need to be partially unfolded for secretion [120, 122, 123].

1.2.5 *Bartonella* effector proteins

Parallel evolution of *Bartonella* effector proteins (Beps) associated with the VirB/D4 T4SS of *Bartonella* lineages 3 and 4 resulted in an arsenal of effectors which are translocated inside host cells upon infection (Figure 7) [108,124]. These proteins contain a C-terminal *Bartonella* intracellular delivery (tBID) domain with a positively charged C-terminus that acts as a bipartite translocation signal for the VirB/D4 T4SS [125,126]. In addition, they might have one or more functional domains fused N-terminally from the tBID domain [108,126].

Additional non-C-terminal BID domains (see Section BID domains) can harbour specific functions, as has been shown for the BID domains of BepA, BepF and BepC [126–129].

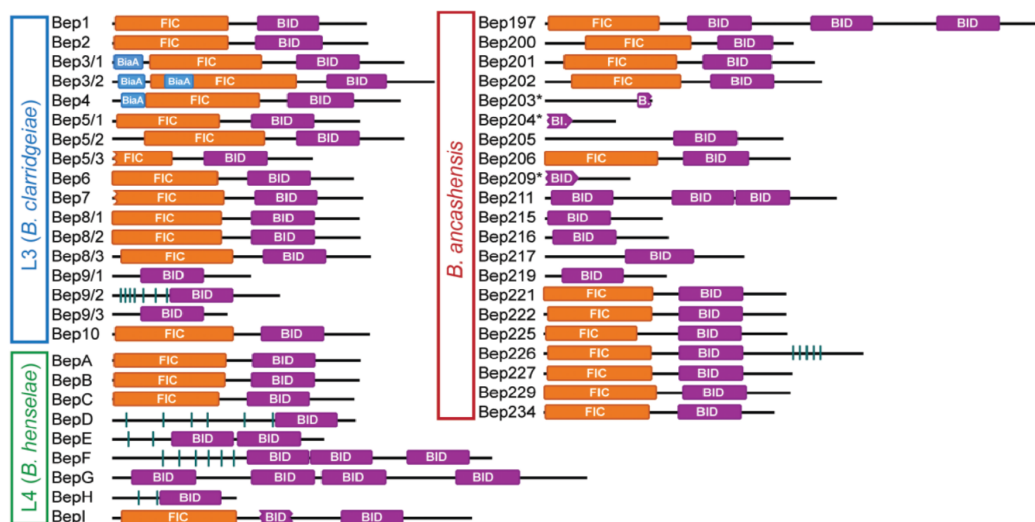


Figure 7: The VirB/D4 T4SS effector repertoire of *Bartonella* spp. - The domain architecture of *Bartonella* effector proteins from L3 (*B. clarridgeiae*), L4 (*B. henselae*) and for *Bartonella ancashensis* of L1. FIC and BID domains are shown in orange and violet, respectively. Fused anti-toxins are colored in blue. Green tick marks represent predicted tyrosine phosphorylation sites. (taken from [110])

Besides the omnipresent BID domains, Beps can also harbour other domains including tyrosine phosphorylation motifs or FIC domains. Whereas tyrosine phosphorylation motifs, like those in BepD, function as a hub for SH2 domain containing signaling proteins [110,130,131], FIC domains often possess enzymatic activities [60,132–134]. They are the most abundant N-terminal extension of Beps (Figure 7).

All known Bep FIC domains are C-terminally fused with an oligonucleotide/oligosaccharide binding fold (OB-fold), that was first discovered as a conserved structural element, that binds oligonucleotides and oligosaccharides. Since then it was also shown to interact with DNA, RNA and proteins [135–137]. However, the function of the OB-fold in Beps is not well understood and has not been the focus of previous studies.

1.3 BID domains

BID domains are secretion signals known from Beps and relaxases. They are closely linked to the VirB/D4 T4SS secretion system, that is used by bacteria and archaea for interkingdom DNA and protein transfer [123, 125]. In both, Beps and relaxases, the terminal BID domain (called tBID_x, with x as an index of the BID domain from the N-terminus) is coupled with a positively charged C-terminus. Jointly, BID domain and C-terminus build a complex bipartite secretion signal necessary for interaction with the coupling protein VirD4 and consecutive secretion of the effector by the VirB/D4 T4SS. [94, 125, 126].

Some BID domains of Beps have shown diverse phenotypes in *in vitro* infection studies with HUVECs (human umbilical vein endothelial cells) and HeLa cells. Since these non-terminal BID domains (BID_x) lack the selection pressure to interact with the coupling protein, duplication and diversification apparently drove BID domains to facilitate ever new effector functions. [103, 126, 130, 138]

Structural analysis of BID domains from 3 effectors (Bep6, Bep9 and BepE) showed an elongated antiparallel four-helix bundle (Figure 8) with a conserved core (RMSD of 1.15 Å and 1.76 Å for 95 core C α -Atoms) and place the potential VirD4 interaction site directly at the tip of the BID domain [126, 139].

BID domains show an overall low sequence conservation, except for some hot-spots like the P₃₆₈xxxxxL₃₇₄[A/R/K]G₃₇₆ motif at the tip of the BID-hook. In sub-classes, for example the class of FIC-OB associated ancestral tBIDs, conserved hot-spots are more prominent and include the L₂₉₈IPxE₃₀₂ motif. These conservation islands allow speculations about inter-domain interaction sites and interaction sites with VirD4 [126].

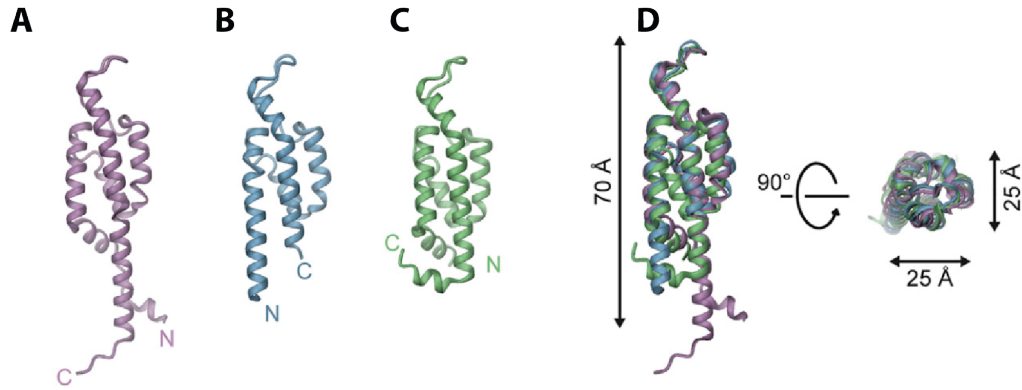


Figure 8: Structure of the BID domain - Structures of (A) Bep6_tBID1 from *B. rochalimae*, (B) Bep9tBID1 from *B. clarridgeiae* and (C) BepE_{BID1} from *B. henselae* side by side. (D) Superposition shows a conserved core structure with RMSDs of 1.15 Å (A-B) and 1.76 Å (A-C). (taken from [126])

1.4 Fic Proteins

The first Fic (filamentation induced by cyclic AMP) protein was discovered in the early 1980s in an *E. coli* mutant that showed impaired cell division during growth conditions under high temperature with cAMP present in the growth media. [140].

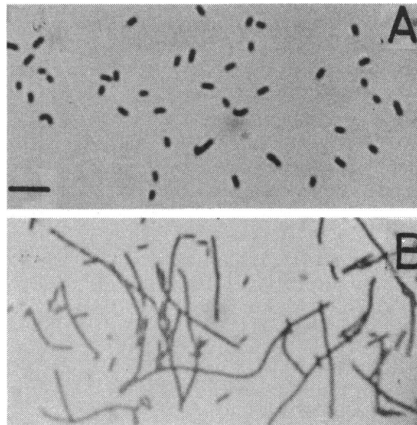


Figure 9: Filamentation induced by cAMP - *E. coli* incubated in LB at 43°C supplemented with 10 mM cAMP. Bacteria in (A) grow normal, while FIC-mutants in (B) are unable to separate and grow into filaments. (taken from [140])

It took nearly 30 years until the cause of this phenotype was discovered, when it was shown that VopS, from the gram-negative, halophilic bacteria *Vibrio para-*

1 Introduction

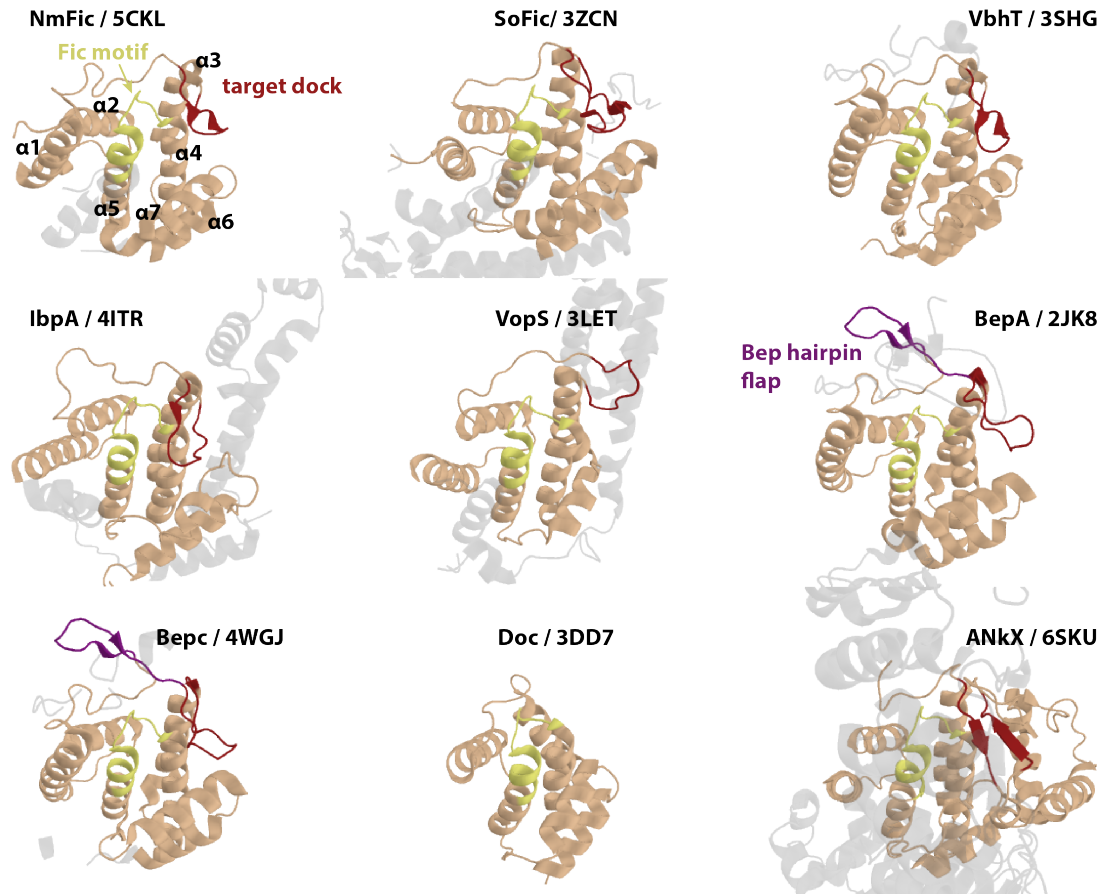


Figure 10: Topology of selected FIC proteins from eukaryotes, prokaryotes and viruses - Fic proteins are shown with a core of 7 α -helices (in beige). The conserved signature motif between helices α 4 and α 5 is drawn in yellow. The β -hairpin flap, for registration of target hydroxyl, is indicated in red. An additional hairpin loop, directly preceding the Fic flap, unique to Beps, is drawn in purple. Additional structure elements of respective Fic proteins are indicated as grey shadows.

haemolyticus, was carrying out a modification called adenylylation, also known as AMPylation. [61]. AMPylation or adenylylation reactions describe the covalent addition of AMP to a protein by using ATP as substrate ($\text{ATP} + \text{target} \xrightarrow{\text{FIC}} \text{target-AMP} + \text{PPi}$). Stable adenylylation had already been reported in the 1960s for glutamine synthetase adenylyltransferase [141, 142] and transient AMPylations of C-terminal glycines or lysines had been shown for ubiquitin-like proteins and during DNA/RNA ligation [143, 144]. However, Fic proteins show no similarities to those GS-ATases and polynucleotide ligases. In fact, adenylylation as a PTM just re-emerged with the discovery of VopS and IbpA [60, 61, 145].

Since then, the Fic/Doc protein superfamily has grown rapidly and includes proteins from eukaryotes, bacteria, archaea and viruses (<http://pfam.xfam.org/family/Fic>) [60, 132, 134, 146, 147] that carry out NMPylation, phosphorylation and phosphocholination (Figure 11) [148–151].

The superfamily is defined by an all helical topology of generally 7 α -helices and shares a common signature motif, in the most general annotation HPFX(D/E)GNGR, in its catalytic centre (Figures 11 and 10). The majority of Fic proteins show an overall low sequence identity and contain additional helices of considerable variation [133, 149–155].

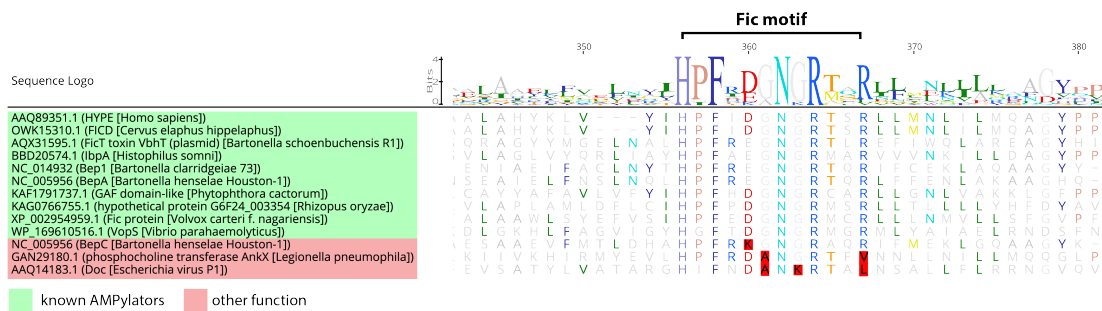


Figure 11: Multiple sequence alignment of selected FIC proteins from eukaryotes, procaryotes and viruses - Accession numbers, names and species are shown at the left. Fic proteins containing the conserved signature motif, HxFx[D/E]GNGRxxR, are shown with green background color. Proteins with a deteriorating motifs are shown with a red background color and critical deviations from the consensus are highlighted in red.

The importance of the Fic signature motif becomes clear when observing the function of Fic/Doc proteins with deteriorated motifs, like Doc from *Escherichia* virus P1 (P1 Phage) and AnkX from *Legionella pneumophila* that carry out different catalytic abilities (see Figure 11). Although the conformation of the Fic loop is nearly identical to other Fic proteins, Doc and AnkX phosphorylate and phosphocholinate their targets, respectively [150, 151]. Fic proteins carrying out AMPylations can be discriminated from other members of the Fic/Doc superfamily and usually show an extended signature motif, HPFX(D/E)GNGRxxR [133, 149, 152, 154, 156].

1.4.1 Fic structure and function

Most residues of the Fic signature motif, HPFX(D/E)GNGR₁xxR₂, have been studied in detail (Figure 12A), with mutations showing significantly diminished AMPylation activity. In detail, the GNG motif builds an anion hole that accommodates the α -phosphate of the nucleotide co-factor, while the phenylalanine side chain anchors the catalytic Fic loop to the hydrophobic core. Mg²⁺, necessary for the AMPylation reaction, is positioned by either the aspartate or glutamate residue of the motif (D/E). The Mg²⁺, coordinates the α - and β -phosphates of the nucleotide and stabilizes the transition state during catalysis. Additionally, R₁ interacts with the β -phosphate of the co-factor. The other arginine (R₂), present only in Fic proteins that catalyze AMPylations, binds the γ -phosphate in an adenylation competent conformation. The catalytic histidine functions as a general base, thus deprotonating the target hydroxyl side chain and priming it for a nucleophilic attack on the α -phosphate of the co-factor [60, 61, 133, 149, 152, 157, 157–159].

1.4.2 Regulation and classification of Fic proteins

Most Doc/Fic superfamily proteins are tightly regulated by an inhibitory element, that interferes with binding or positioning of the nucleotide co-factor. This inhibitory element might be fully or partly unfolded but usually adopts an α -helical fold upon interacting with the FIC domain [154–156, 160]. While Phd, the anti-toxin that contains the inhibitory α -helix of Doc, obstructs the binding of the nucleotide more extensively [151, 160], a short central (S/T)XX(I/L)EG motif is responsible for the inhibitory effect on the catalytic function in the majority of Fic proteins [154, 156].

Although, complete deletion of the inhibitory α -helix obviously releases the inhibition of the adenylation function, single point mutations of the inhibitory motif have shown, that the glutamate is of special importance.

Mutagenesis of NmFic from *Neisseria meningitidis* and SoFic from *Shewanella oneidensis* showed, that a single glutamate to glycine mutation is sufficient to release the inhibition of the FIC domain. Similar mutations of VbhA, the anti-toxins of the *Bartonella schoenbuchensis* toxin VbhT, that represses the catalytic activity of VbhT, showed the same effect. [154, 161, 162]

Structural studies of Fic proteins revealed a common inhibitory mechanism, were

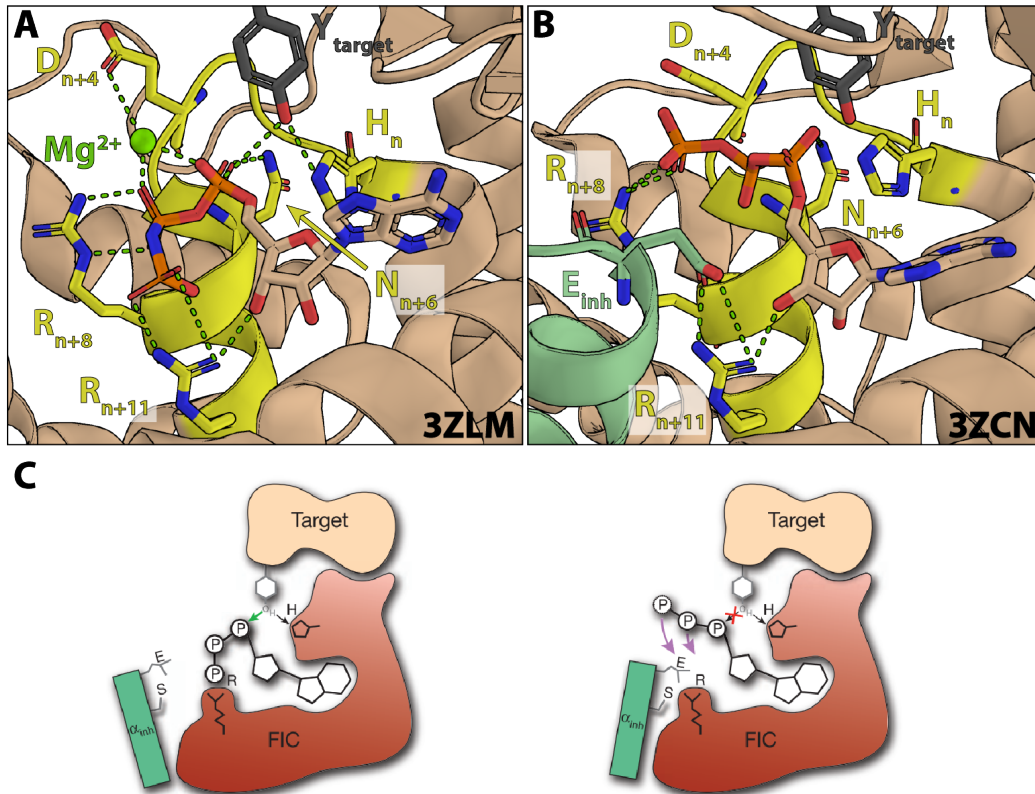


Figure 12: AMPylation mechanism and inhibition of AMPylation in Fic domain proteins - (A) The Fic domain of NmFic from *Neisseria meningitidis* with the non-hydrolysable ATP analog AMPPNP in its AMPylation competent conformation (in beige). The Fic motif is drawn in yellow and important residues are shown as sticks. Indices from the motif start (H) are indicated as numbers. A hypothetical target tyrosine is shown in grey. Mg^{2+} is represented as green sphere. Interactions are drawn as green dashed lines. (B) The Fic domain of SoFic from *Shewanella oneidensis* with ATP (in beige) and the N-terminal inhibitory α -helix (in green). (C) Cartoon of the Fic AMPylation and inhibition mechanism corresponding to (A) and (B). (cartoon taken from [154])

the glutamate of the inhibitory motif forms a salt-bridge with the trailing arginine of the Fic motif. This prevents optimal placement of the nucleotides β - and γ -phosphates and leads to a non-competent positioning of the α -phosphate, thus preventing a successful nucleophilic attack from the target hydroxyl side chain (Figure 12B) [156].

Based on the position of the inhibitory α -helix, Fic proteins can be divided into 3 classes: Class I Fic proteins like VbhT contain the inhibitory element on a separate

1 Introduction

molecule, VbhA, and are classical toxin-antitoxin modules [124, 154, 158, 163, 164]. An N-terminal inhibitory α -helix, like in SoFic, classifies as a Class II Fic proteins and class III, containing NmFic, is defined by a C-terminal inhibitory α -helix (Figure 13). [88, 154, 162].

In contrast to the toxin-antitoxin modules of class I, class II and III Fic proteins seem to have evolved primarily for the regulation of cellular functions. Huntington yeast-interacting protein E (HYPE), also called FICD, is a class II Fic protein present in higher eukaryotes, that is involved in the unfolded protein response (UPR). [60, 153, 154]. For this purpose, FICD is able to AMPylate (deactivate) and de-AMPylate (activate) the major ER chaperone BiP, thus matching BiPs activity to the burden of unfolded proteins [153, 165–169].

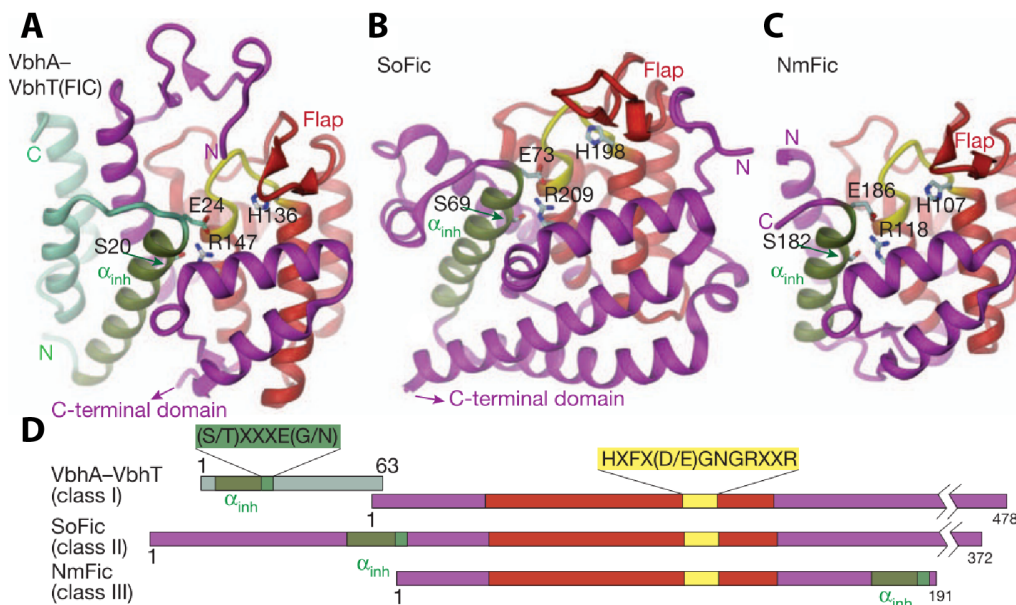


Figure 13: The Fic inhibitory motif and Fic classes - VbhT\VbhA, SoFic and NmFic as representatives for the Fic classes I, II and III, respectively. (taken from [156])

The class III Fic protein NmFic of *Neisseria meningitidis* has been shown to AMPylate the B-subunit of DNA gyrase (GyrB). This catalytic activity of NmFic is tightly regulated through a complex mechanism of tetramerization and cis-autoadenylation which results in a concentration and time dependent activation/de-activation of GyrB. This suggests, that the strongly conserved class III Fic proteins might function as intrinsic molecular timers [155, 156].

Intriguingly, auto-modification has been found in almost all currently known Fic proteins, which raises the question of whether the activation of FIC domains is generally depending on autoadenylation [133, 134, 149, 153, 154, 156, 170, 171].

1.4.3 Fic target interaction

VopS was the first member of the growing Fic protein family and found to AMPylate GTPases of the Rho family. It harbours a canonical FIC domain at its C-terminus, that is preceded by an additional 10 α -helices folding into an elongated arm domain. This arm domain plays a crucial role for VopS-target binding during the AMPylation of a threonine residue (Thr35 in Cdc42) in the switch1 region of Rho family GTPases [60, 61, 148, 149, 152].

Target recognition has been shown to be similar for the C-terminal FIC domain of Immunoglobulin-binding protein A (IbpA) from *Histophilus somni*, a major cause of poisoning from undercooked shellfish, that causes a collapse of the actin cytoskeleton in host cells. IbpA modifies Rho GTPases at a tyrosine side chain (Tyr32 in Cdc42) in the the switch1 region, in contrast to VopS [60, 148, 149].

Catalysis of AMPylation seems to be independent of the GTPases activation state, as IbpA is able to target GDP and GTP bound Rho-family GTPases and has been found to even modify Rho GTPases in complexes with their GDI [148]. The difference of an adenylation at the tyrosine (IbpA) or threonine (VopS) residue is yet unclear, since both modifications are in the switch1 loop and block downstream signaling [3, 13, 60, 61].

Switch2 triple mutants of Cdc42, Rac and RhoA (Tyr₆₄Ala, Leu₆₇Glu, Leu₇₀Glu in Cdc42 and corresponding residues in Rac and RhoA) could not be modified by either VopS or IbpA, pointing out the importance of the interaction between the effector arm domain and switch2 region of target Rho-family GTPases for effective adenylation [149].

Structural analysis of the catalytically compromised IbpA_{Fic2} mutant IbpA_{Fic2,H317A} in complex with Cdc42 revealed further interactions with the switch1 region of target GTPases. Three main chain - main chain hydrogen bonds are made between residues of switch1 of the GTPase (Val33 to Thr35) and a short flap of IbpA preceding the Fic signature motif (Asn3667 to Thr3669), resulting in a three-stranded β -sheet. A "clamp" formed by Leu3668 and Lys3670 locks the target hydroxyl side-chain in an

1 Introduction

AMPylation-competent orientation (Figure 14A) [149, 152, 156].

Intriguingly, β -sheet augmentations, as found in the IbpA-target complex structure, are not restricted to arm domain coupled Fic proteins. Instead, the "target dock", including the hydroxyl "clamp", seems to be a conserved, sequence independent mechanism in Fic proteins for proper positioning of the target side chain (Figures 14A-C) [133, 149, 152–155].

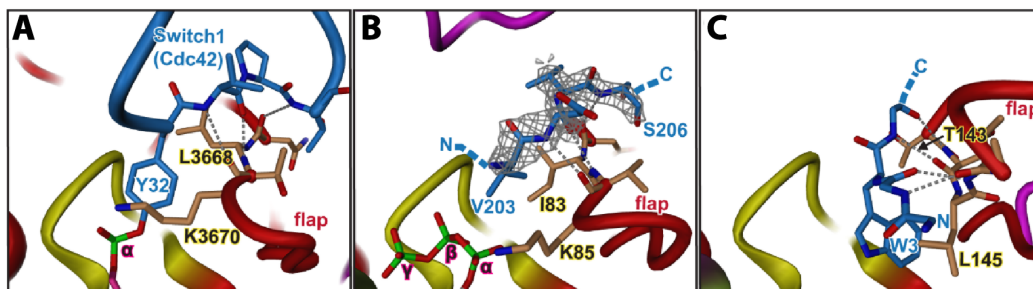


Figure 14: Sequence independent target-dock of Fic proteins - The Fic β -hairpin flap of canonical Fic proteins in (A) IbpA, (B) VbhT, and (C) SoFic. Fic motifs indicated in yellow. The flap (in red) forms main chain – main chain hydrogen bonds (grey dashed lines) with the registered sequence (blue). A "clamp" (brown, residues indicated) locks down the target hydroxyl side chain. (taken from [156])

2 Aim of the thesis

2 Aim of the thesis

The functional characterization of Fic proteins has been the focus of research for several years and led to a rapidly growing field.

Currently, PFAM (<http://pfam.xfam.org/family/Fic>) lists 11775 different protein sequences in the Fic/Doc superfamily.

The mechanism of AMPylation by FIC domains has already been well described. However, very few targets have been found for the various PFAM entries. For those Fic-target interactions that have been studied in more detail, interactions depend on extensive secondary domains (IbpA [60], VopS [61]). The majority of Beps from *Bartonella* spp. contain Fic domains with a canonical Fic motif, but lack any comparable arm-element for target interactions [110,133]. The arsenal of *Bartonella* effector proteins in L3 and L4 provide a vast playground to study interaction partners of Fic proteins and search for common binding motifs.

During my PhD, I was looking for Bep FIC domain targets and I was trying to shine light on how the interaction between these Fic domains and their targets is facilitated.

The main aim of my thesis was, to analyze the target specificity of the FIC domain containing *Bartonella* effector Bep1 by using biophysical and biochemical assays. In this context, I was supposed to set up an assay to determine kinetic parameters of the catalyzed AMPylation reaction. Furthermore, I was aiming to crystallize Bep1 and its homologs in complex with potential eukaryotic target proteins.

Although crystallization of a complex structure did not work during my thesis, I was able to get a full length structure of Bep1. Thus, an additional goal was to find important intramolecular interactions, that might explain how an unfolding process, prior to T4SS translocation could be facilitated.

3 Results

3.1 Research article I

Structural basis for selective AMPylation of Rac-subfamily GTPases by Bartonella effector protein 1 (Bep1)

Nikolaus Dietz, Markus Huber, Isabel Sorg, Arnaud Goepfert, Alexander Harms,
Tilman Schirmer, and Christoph Dehio

PNAS, Volume 118, Issue 12

Statement of the own participation

I contributed to this publication by performing and analyzing qualitative (autoradiography) and quantitative (oIEC) AMPylation assays with Bep1_{FIG}* from *B. rochalimae* and target variants. Constructs were cloned by Nikolaus Dietz and myself. The complex was modeled by Nikolaus Dietz and autoradiography with the complete Rac-family GTPase panels were done by Isabel Sorg. The project is based on analysis of Arnaud Goepfert and Alexander Harms, who first found Rho GTPases as targets of Bep1. The manuscript was written by Nikolaus Dietz and me.



Structural basis for selective AMPylation of Rac-subfamily GTPases by *Bartonella* effector protein 1 (Bep1)

Nikolaus Dietz^{a,1}, Markus Huber^{a,1}, Isabel Sorg^a, Arnaud Goeppfert^{a,2}, Alexander Harms^a, Tilman Schirmer^{a,3}, and Christoph Dehio^{a,3}

^aBiozentrum, University of Basel, 4056 Basel, Switzerland

Edited by Ralph R. Isberg, Tufts University School of Medicine, Boston, MA, and approved February 8, 2021 (received for review November 8, 2020)

Small GTPases of the Ras-homology (Rho) family are conserved molecular switches that control fundamental cellular activities in eukaryotic cells. As such, they are targeted by numerous bacterial toxins and effector proteins, which have been intensively investigated regarding their biochemical activities and discrete target spectra; however, the molecular mechanism of target selectivity has remained largely elusive. Here we report a bacterial effector protein that selectively targets members of the Rac subfamily in the Rho family of small GTPases but none in the closely related Cdc42 or RhoA subfamilies. This exquisite target selectivity of the FIC domain AMP-transferase Bep1 from *Bartonella rochalimae* is based on electrostatic interactions with a subfamily-specific pair of residues in the nucleotide-binding G4 motif and the Rho insert helix. Residue substitutions at the identified positions in Cdc42 enable modification by Bep1, while corresponding Cdc42-like substitutions in Rac1 greatly diminish modification. Our study establishes a structural understanding of target selectivity toward Rac-subfamily GTPases and provides a highly selective tool for their functional analysis.

AMPylation | structure function | FIC domain | RhoGTPases | *Bartonella* effector protein

Small GTPases of the Ras-protein superfamily are molecular switches that control fundamental cellular functions in eukaryotes by cycling between GTP-bound “on” and GDP-bound “off” conformational states of their switch regions 1 (Sw1) and 2 (Sw2) (1, 2). Members of the Ras-homology (Rho) protein family function as signaling hubs and regulate cytoskeletal rearrangements, cell motility, and the production of reactive oxygen species (3, 4). The defining element in Rho-family GTPases is the presence of a Rho insert, a highly variable, 13-residue-long, α -helical insert close to the C terminus. The Rho insert has previously been implicated in the wiring of Rho-family GTPases to their specific biological functions (5, 6). Six members of the Rho-protein family closely related to Cdc42 share an altered amino acid sequence in the G4 nucleotide binding motif with a glutamine residue instead of lysine in the second position.

Due to their central role in eukaryotic cell signaling, especially in the immune response, Rho-family GTPases are targeted by a plethora of bacterial virulence factors, including secreted bacterial toxins that autonomously enter host cells and effector proteins that are directly translocated from bacteria into host cells via dedicated secretion systems (7, 8). By means of these virulence factors, pathogens established ways to stimulate, attenuate, or destroy the intrinsic GTPase activity of Rho-family GTPases, either directly through covalent modification of residues in the Sw1 or Sw2 regions (8) or indirectly by mimicking guanine nucleotide exchange factor (GEF) or GTPase-activating protein (GAP) function. However, the structural basis for selective targeting of Rho-family GTPase subfamilies has remained unknown (7).

The bacterial genus *Bartonella* comprises a rapidly expanding number of virtually omnipresent pathogens adapted to mammals, many of which have been recognized to cause disease in humans

(9). The stealth infection strategy of *Bartonella* spp. (10) rely to a large extent on translocation of multiple *Bartonella* effector proteins (Beps) via a dedicated type 4 secretion system. Strikingly, the majority of the currently known several dozens of Beps contains enzymatic FIC domains (9, 11), indicating that *Bartonella* spp. successfully utilize this effector type in their lifestyle. In order to gain more insights into the function of FIC domain-containing Beps we have here investigated Bep1 of *Bartonella rochalimae* originally described by Harms et al. (11).

Filamentation induced by cyclic AMP (FIC) domain-containing effector proteins belong to the ubiquitous FIC domain family with a conserved molecular mechanism for posttranslational modification of target proteins. FIC domains consist of six helices with a common HxFx(D/E)GNGRxxR motif between the central helices 4 and 5 (12). Some of the FIC domain-containing effector proteins have been recognized to modify Rho-family GTPases by catalyzing transfer of the AMP moiety from the ATP substrate to specific target hydroxyl side chains (12, 13). Prototypical examples are the effector proteins IbpA from *Histophilus somni* and VopS from *Vibrio parahaemolyticus*, which both target a wide range of Rho-family GTPases and AMPylate (adenylylate) a conserved tyrosine or

Significance

Mammalian cells regulate diverse cellular processes in response to extracellular cues. Small GTPases of the Rho family act as molecular switches to rapidly regulate discrete cellular activities, such as cytoskeletal dynamics, cell movement, and innate immune responses. Numerous bacterial virulence factors modulate the function of Rho-family GTPases and thereby manipulate intracellular signaling. For many of these virulence factors we have gained detailed understanding how they covalently modify individual Rho-family GTPases to reprogram their activities; however, their mechanisms of selective targeting of distinct subsets of Rho-family GTPases remained elusive. Using a combination of structural biology and biochemistry, we demonstrate for the effector protein Bep1 exclusive specificity for Rac-subfamily GTPases and propose the underlying mechanism of target selectivity.

Author contributions: N.D., M.H., I.S., A.H., T.S., and C.D. designed research; N.D., M.H., I.S., A.G., and A.H. performed research; N.D., M.H., A.G., A.H., T.S., and C.D. analyzed data; and N.D., M.H., T.S., and C.D. wrote the paper.

The authors declare no competing interest.

This article is a PNAS Direct Submission.

This open access article is distributed under Creative Commons Attribution-NonCommercial-NoDerivatives License 4.0 (CC BY-NC-ND).

¹N.D. and M.H. contributed equally to this work.

²Present address: Ichnos Sciences Biotherapeutics SA, 1066 Epalinges, Switzerland.

³To whom correspondence may be addressed. Email: tilman.schirmer@unibas.ch or christoph.dehio@unibas.ch.

This article contains supporting information online at <https://www.pnas.org/lookup/suppl/doi:10.1073/pnas.2023245118/-DCSupplemental>.

Published March 15, 2021.

threonine residue of Sw1, respectively (14–16). Both modifications result in abrogation of downstream signaling, causing collapse of the cytoskeleton of the host cell and subsequent cell death (17). Here we show that the FIC domain of *Bartonella* effector protein 1 of *B. rochalimae* (Bep1) AMPylates the same Sw1 tyrosine residue as IbpA, while the target spectrum is strictly limited to the Rac subfamily of Rho GTPases. Employing a combination of structural analysis, modeling, biochemistry, and mutational analysis, we identify the structural determinants of this remarkable target selectivity. Our findings highlight the potential of Bep1 as a tool for dissecting Rho-family GTPase activities and provide a rationale for the redesign of its target selectivity.

Results

Bep1 Selectively AMPylates Rac-Subfamily GTPases. Bep1 is composed of a canonical FIC domain followed by an oligosaccharide binding (OB) fold and a C-terminal BID domain (11). The latter domain is implicated in recognition and translocation by the type 4 secretion system VirB/VirD4 of *Bartonella* (18, 19).

In search for Bep1 targets we performed AMPylation assays by incubating lysates of *Escherichia coli* expressing Bep1 with eukaryotic cell lysates and α - 32 P-labeled ATP and observed a radioactive band migrating with an apparent molecular weight of 20 kDa (SI Appendix, Fig. S1A), consistent with modification of Rho-family GTPases as previously described for IbpA and VopS (15, 16). To investigate further, we explored the target spectrum of Bep1 and compared it to those of the FIC domains of IbpA (IbpA_{FIC2}) or VopS (VopS_{FIC}) by selecting 19 members of the Ras superfamily (Fig. 1A) with an emphasis on members of the Rho family. While AMPylation activity of all three enzymes was strictly confined to Rho-family GTPases, their target selectivity spectra differed markedly: while Bep1 modified exclusively members of the Rac subfamily (i.e., Rac1/2/3 and RhoG), the target spectrum of IbpA_{FIC2} comprised all Rho GTPases with the exception of RhoH/U/V and the Rnd subfamily, and VopS_{FIC} was found to be fully indiscriminate (Fig. 1A, summarized in Fig. 1D).

Next, we designed a minimal Bep1_{FIC} construct (residues 13 to 229) that proved sufficient for selective target modification. Bep1

belongs to the class I of FIC proteins that are regulated by a small regulatory protein, here BiaA, that inhibits FIC activity by inserting a glutamate residue (E33) into the ATP binding pocket (20). In order to improve expression level and stability, we coexpressed Bep1_{FIC} with an inhibition relieved mutant (E33G) of BiaA, yielding the stabilized minimal AMPylation-competent Bep1_{FIC}/BiaA_{E33G} complex, in short, Bep1_{FIC}^{*}.

Bep1_{FIC}^{*} efficiently AMPylates its targets, and the activity depends on the presence of the catalytic histidine (H170) of the signature motif (Fig. 1B), consistent with the canonical AMPylation mechanism (20). Bep1_{FIC}^{*}, in contrast to VopS_{FIC}, does not AMPylate Rac1_{Y32F} (Fig. 1C), indicating that Bep1_{FIC}^{*} modifies Y32 of the Rac1 Sw1 as confirmed by mass spectrometry (SI Appendix, Fig. S1C). Thus, Bep1_{FIC}^{*} catalyzes the equivalent modification as IbpA_{FIC2} (15, 21), whereas VopS modifies T35 (16).

In contrast to the GDP form, GTP-loaded GTPases may not be amenable to FIC-mediated modification of Y32 since this residue is known to be involved in GTP binding via interaction with the γ -phosphate group (22) (SI Appendix, Fig. S2D). Indeed, exchanging GDP against GTP efficiently protected the GTP hydrolysis deficient mutant Rac1_{O61L} from modification, and the same effect was observed when replacing GDP bound to wild-type Rac1 with nonhydrolyzable GTP γ S (SI Appendix, Fig. S2C). Thus, we conclude that GDP-loaded GTPases are the physiological targets of Bep1-mediated AMPylation.

The Crystal Structure of Bep1_{FIC} Reveals an Extended Target Recognition Flap.

To reveal the structural basis of target selectivity, we solved the crystal structure of Bep1_{FIC}^{*} to 1.6 Å resolution. The structure (Fig. 2) closely resembles those of other FIC domains with AMPylation activity such as VbhT (20), IbpA (21), and VopS (23), featuring the active site defined by the conserved signature motif encompassing the α 4– α 5 loop and the N-terminal part of α 5. Comparison with the apo crystal structure of the close Bep1 homolog from *Bartonella clarridgeiae* (Protein Data Bank [PDB] ID 4nps) shows that the presence of the small regulatory protein mutant BiaA (E33G) in Bep1_{FIC}^{*} does not affect the structure of the FIC domain (SI Appendix, Fig. S2B).

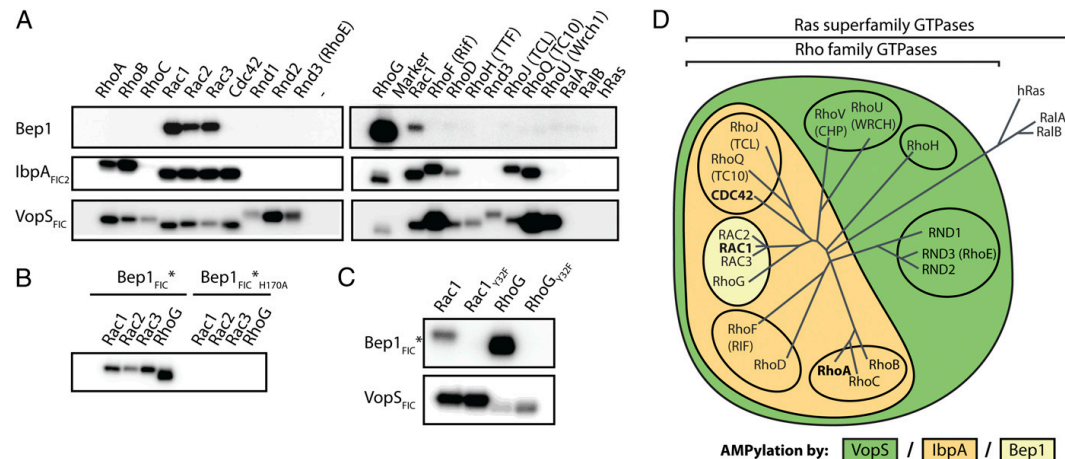


Fig. 1. Bep1 selectively targets Rac-subfamily GTPases. (A) 32 P-autoradiograms of in vitro AMPylation reactions using the indicated purified and GDP-loaded Rho-family GTPases display exquisite selectivity of full-length Bep1 for Rac-subfamily GTPases in contrast to the broader target spectrum of IbpA_{FIC2} and VopS_{FIC}. (B) The FIC domain of Bep1 in complex with the regulatory protein BiaA (Bep1_{FIC}^{*}) is sufficient for the recognition of Rac-subfamily GTPases and the catalytic H170 is required for AMPylation. (C) Bep1_{FIC}^{*} AMPylates residue Y32 of Rac1 and RhoG since the respective Y32F mutants are not modified. AMPylation by the T35-specific VopS_{FIC} indicates structural integrity of the analyzed GTPases and their Y32F mutants. (D) Venn diagram showing AMPylation target selectivity of tested FIC domains, overlaid to the phylogenetic relation of Rho-family GTPases (4).

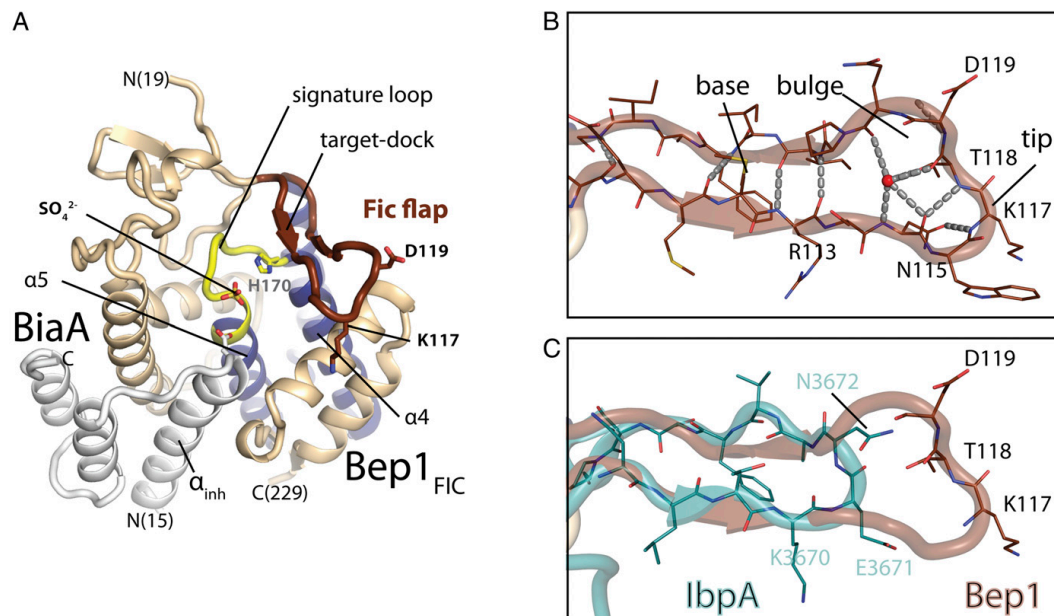


Fig. 2. Crystal structure of Bep1_{FIC}* reveals extended flap. (A) Cartoon representation of the crystal structure of the Bep1_{FIC}:BiaA complex (Bep1_{FIC}*) determined in this work. The regulatory protein BiaA is shown in light gray. The FIC domain fold is shown in light brown, with the central FIC helices ($\alpha 4$ – $\alpha 5$) in blue. The FIC signature loop with the catalytic H170 is shown in yellow, and the FIC flap covering the active site is shown in dark brown. (B) Detailed view of the Bep1 flap region (PDB 5eu0; this study). Structural flap elements are stabilized by an H-bonding network involving main chain and side chain groups. H bonds are shown by gray dashed lines. The base of the flap forms a two-stranded β -sheet, with the N-terminal part constituting the target dock. The tip of the flap forms an $i + 1 + 3$ turn between N115 and T118, which is further stabilized by the side chain of N115. The tip is followed by a bulge and a conserved proline residue and stabilized by interactions of the backbone with a central water (in red). This arrangement suggests that the well-defined structure of the flap orients side chains K117 and D119 for target interaction. (C) Overlay of flaps from Bep1_{FIC} (brown) and IbpA_{FIC2} (turquoise). Residues at the tips of both flaps are indicated. Compared to Bep1, the flap of IbpA is six residues shorter amounting to 8 Å (SI Appendix, Fig. S2A).

The active site is partly covered by a β -hairpin flap (Fig. 2A) that serves to register the segment carrying the modifiable side chain (here Sw1) to the active site via β -sheet augmentation, as has been inferred from bound peptides (16, 24), observed directly in the IbpA_{FIC2}:Cdc42 complex (21), and discussed elsewhere (17). Strikingly, the flap of Bep1 and its orthologs in other *Bartonella* species (SI Appendix, Fig. S2A) is considerably longer than in other FIC structures (e.g., of IbpA_{FIC2}) and features a well-defined bulge at its tip (Fig. 2B and C).

Bep1_{FIC}:Target Model Suggests That Charged Residues of the Flap Determine Target Selectivity. The complex structure of an FIC enzyme with a small GTPase target and the mechanism of FIC catalyzed AMPylation reaction has been elucidated for IbpA_{FIC2} in complex with GDP-loaded Cdc42 (21) (Fig. 3B). The detailed view in Fig. 3D shows that the Sw1 segment of Cdc42 exhibits an extended conformation and forms antiparallel, largely sequence-independent, β -sheet interactions with the flap of the FIC enzyme, thereby aligning the modifiable Y32 with the active site. Considering the close structural homology of the catalytic core of Bep1_{FIC} with IbpA_{FIC2} (rmsd = 1.0 Å for 32 C α atoms in the active site helices) and of Rac-subfamily GTPases with Cdc42 (rmsd = 0.44 Å for 175 C α positions), we reasoned that computational assembly of a Bep1_{FIC}:Rac complex could provide a structural basis for an understanding of Bep1 target selectivity.

Fig. 3A shows the assembled Bep1_{FIC}:Rac2 complex that was obtained by individual superposition of 1) the Bep1_{FIC} active site helices and the flap with the corresponding elements in IbpA_{FIC2}

and 2) the Sw1 loop of Rac2 with that of Cdc42. Thereby, we assumed implicitly that the interaction between these central segments should be very similar since both FIC enzymes utilize a homologous set of active residues to catalyze AMP transfer to a homologous residue (Y32) on Sw1.

The local structural alignment resulted in a virtually identical relative arrangement of the FIC core to the GTPase as in the template structure (compare Fig. 3A and B) and caused no steric clashes. Conspicuously, the extended Bep1_{FIC} flap is accommodated in a groove formed by Sw1 (residues 31 to 40), the GDP-loaded nucleotide binding G4 motif [T(K/Q)xD, residues 115 to 118] (25), and the following Rho-insert helix (Rac2 residues 121 to 133) (Fig. 3C and SI Appendix, Fig. S2E).

The manually created complex model was used as input for an adapted Rosetta modeling protocol to allow for sampling of backbone and side chain torsion angles in the interface of the complex, as described in *Materials and Methods* (26, 27). Consistent with the low affinity of the complex *in vitro* (see below), the models confirm the relatively small interface area of ~ 800 Å². Common to all top scoring models we find that the modifiable residue Y32 is pointing toward the active site of Bep1, where it is held in place by a main chain-mediated interaction between the base of the flap and the Sw1 loop of the GTPase (SI Appendix, Fig. S3A), indicating that the configuration of active site residues and the modifiable tyrosine side chain is, indeed, most likely the same as in the template complex.

However, in the IbpA_{FIC2}:Cdc42 complex, the aforementioned GTPase groove on the nucleotide binding face is not utilized for

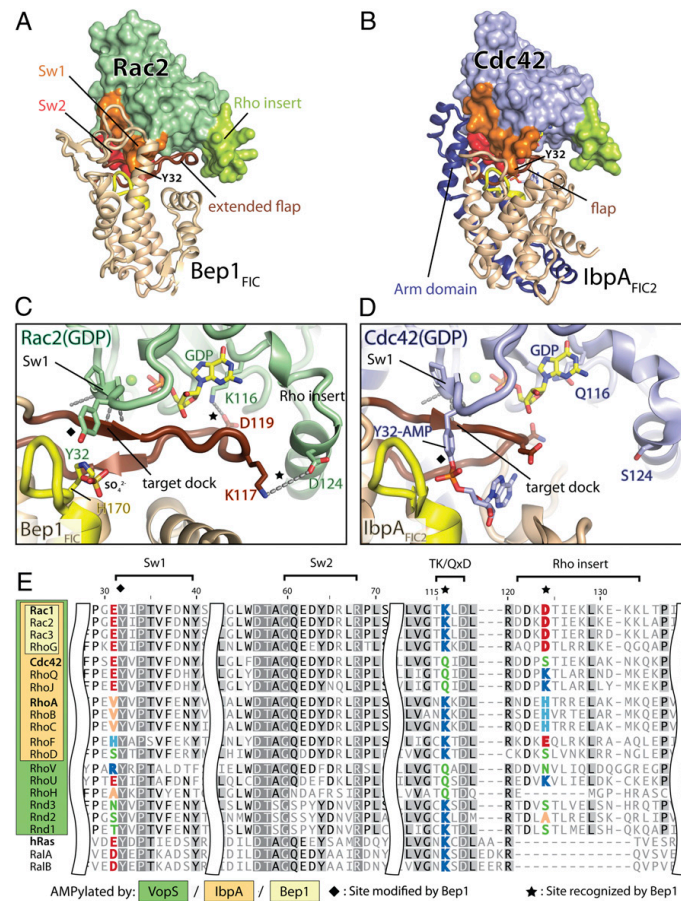


Fig. 3. Bep1_{FIC}:Rac2 complex model suggests charged interactions between FIC flap and targets. Side-by-side view of (A) Bep1_{FIC}:Rac2 complex model and (B) IbpA_{FIC2}:Cdc42 crystal structure (PDB 4itr). The FIC fold is shown in light brown. The FIC signature loop with the catalytic H170 is shown in yellow, and the FIC flap covering the active site is shown in brown. GTPases are shown as surface representation with indicated structural elements distinguished by color: Switch 1 (Sw1) in orange, Switch 2 (Sw2) in red, and Rho insert in green. The extension of the Bep1_{FIC} flap is accommodated in a groove formed by the TK(Q)xD motif and the Rho insert (B), whereas the arm domain of IbpA (in blue) contacts the effector binding regions, Sw1 and Sw2, of the GTPase. Comparison of intermolecular interactions in (C) the Bep1_{FIC}:Rac2 model and (D) the IbpA_{FIC2}:Cdc42 complex. H-bonding and electrostatic interactions are indicated by dashed lines in gray. The tip of the Bep1_{FIC} flap is accommodated in a groove, with K117 and D119 in favorable position to interact with D124 and K116 of Rac2, respectively. (D) In the IbpA_{FIC2}:Cdc42 complex the Rho insert region is not involved in such interaction. (E) Structure-guided sequence alignment of the GTPases of the Rho, Ras, and RalA/B families. The K116/D124 configuration (marked with a star) is unique to Rac1/2/3 and RhoG (light yellow). Residue numbers refer to Rac1, and names of representative members of Rho subfamilies are indicated in bold.

the contact (Fig. 3D). Instead, the so-called arm domain of IbpA_{FIC2} (Fig. 3B) constitutes a major part of the interface and contacts the highly conserved Sw2 loop of Cdc42. This rationalizes the broad target spectrum of arm domain-containing FIC AMP transferases like IbpA and VopS (12, 23). In turn, residues of the groove predicted to get recognized exclusively by Bep1_{FIC} are likely to be important for the limited target range of Bep1. Conspicuously, the top scoring models revealed two potential salt bridges between the Bep1 flap and the Rac2 groove, namely, D119(Bep1)–K116(Rac2) and K117(Bep1)–D124(Rac2) (Fig. 3C and *SI Appendix*, Fig. S3A). Since the combination of K116 and D124 is exclusively found in the Rac subfamily as revealed by sequence alignment of Rho-family GTPases (Fig. 3E), we reasoned

that these residues may contribute significantly to the specific recognition of Rac GTPases by Bep1 (Fig. 14).

Two Salt Bridges between Flap and Target Are Crucial for Selective Interaction of Bep1_{FIC} with Rac-Subfamily GTPases. The relevance of the two identified salt bridges in the Bep1_{FIC}:Rac2 complex (Fig. 3C) for affinity and selectivity was tested by single and double replacements of the constituting residues 116 and 124 in a Bep1 target and a nontarget GTPase. For Rac1, we tested if substitutions at these residues with corresponding amino acids of Cdc42—a nontarget of Bep1 with the highest conservation in regions flanking the proposed interaction sites (Fig. 3E)—influence target recognition (loss-of-function approach; see interaction

schemes in Fig. 4A). In addition, we tested whether Cdc42 can be converted to a Bep1 target by reciprocal substitution(s) of these sites with the corresponding Rac1 residues (gain-of-function approach; Fig. 4B).

First, we applied, as for Fig. 1A, the autoradiography end-point assay with ^{32}P - α -ATP as substrate. Compared to wild-type Rac1, mutant D124S showed no significant difference in the amount of AMPylated target, whereas AMPylation of mutant K116Q and, even more, of the double mutant was found drastically reduced (Fig. 4C and *SI Appendix*, Fig. S4A). Conversely, in the gain-of-function approach, Cdc42 mutant S124D did not convert the GTPase to a Bep1 target, while mutant Q116K and the double mutant showed low but significant AMPylation (Fig. 4D and *SI Appendix*, Fig. S4B). In a fairly indiscriminating way, IbpA_{FIC2} modified all investigated GTPase variants (*SI Appendix*, Fig. S4C and D) indicating their proper folding. Together, the semiquantitative radioactive end-point assay demonstrated a major role of K116 in target recognition by Bep1_{FIC*}, while a contribution of D124 could not be demonstrated.

To overcome the limitations of the radioactive end-point assay and to characterize target AMPylation quantitatively, we developed an online ion exchange chromatography (oIEC) assay (*Materials and Methods*) which allows separation of reaction components (Fig. 4E) and efficient acquisition of enzymatic progress curves to determine initial velocities, v_{init} (see, for instance, *SI Appendix*, Fig. S4F, Inset). For AMPylation of Rac1 by Bep1_{FIC*}, titration experiments yielded K_M values of 0.52 and 1.4 mM for the substrates

ATP and Rac1, respectively, and a k_{cat} of 1.9 s^{-1} . The comparison with published values on other Fic AMP transferases (*SI Appendix*, Table S1) shows that the K_M values are comparable to IbpA but that k_{cat} is smaller by about two orders of magnitude.

Considering the physiological conditions in the cell with an ATP concentration above K_M , Bep1 can be expected to be saturated with ATP and only partially loaded with the target (target concentration $\ll K_{M, \text{target}}$). In such a regime, the AMPylation rate will be given by

$$v = \frac{k_{\text{cat}}}{K_{M, \text{target}}} \times [E_0] \times [\text{target}]$$

(28), i.e., will depend solely on the second order rate constant $k_{\text{cat}}/K_{M, \text{target}}$ (efficiency constant), which is, thus, the relevant parameter for enzyme comparison.

Next, we determined the efficiency constants for all GTPase variants. In the loss-of-function series, the single mutants reduced the efficiency constant by 2- and 6-fold, and the double mutant reduced the efficiency constant by about 30-fold (Fig. 4E and *SI Appendix*, Table S1).

Under the assumptions that 1) k_{cat} is not changed upon the mutations, since they affect sites on the target that are distant from the catalytic center, and 2) K_M is equal to the K_D of the enzyme-target complex, as is warranted for a slow enzyme, the difference in the measured efficiency constants can be attributed to an altered stability of the Michaelis-Menten complex.

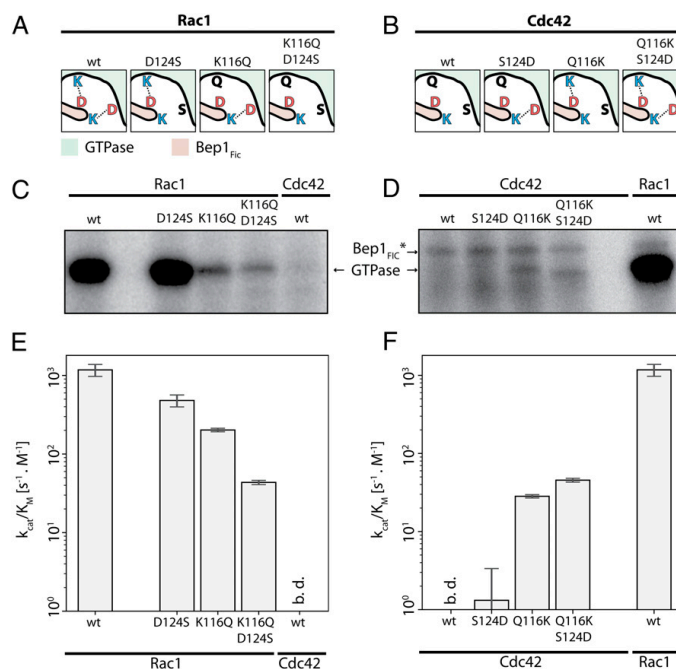


Fig. 4. Two salt bridges are crucial for Rac-subfamily selective AMPylation. (A) Schematic view of the two intramolecular Bep1_{FIC}:Rac1 salt bridges (Left) and their partial disruption upon site-directed Rac1 mutagenesis, yielding Rac1 loss-of-function mutants (Right). (B) Absence of ionic interactions in the predicted Bep1_{FIC}:Cdc42 interface (Left) and partial establishment of salt bridges in Cdc42 gain-of-function mutants (Right). (C and D) AMPylation of the variants given in A and B as measured by autoradiography. Note that due to the employed higher Bep1_{FIC*} concentration (*Material and Methods*), the experiments in D also revealed auto-AMPylation of Bep1_{FIC*}. (E and F) Enzymatic efficiency constants, k_{cat}/K_M , for Bep1_{FIC*} catalyzed AMPylation of the GTPase variants shown in A and B as derived from the oIEC measurements shown in *SI Appendix*, Fig. S4. b.d., below detection limit. Error bars indicate standard deviation of reaction efficiencies.

Furthermore, the change of the free energy of binding upon mutation ($\Delta\Delta G$) can be derived from the measured efficiency constants of wild-type and mutant target under these assumptions. The calculations given in *SI Appendix, Table S2*, show that the $\Delta\Delta G$ of the double mutant is larger by only about 25% compared to the $\Delta\Delta G$ sum of the single mutants, suggesting that the contributions of the two salt bridges are largely independent.

In the gain-of-function series, wild-type Cdc42 showed no and mutant S124D only marginal modification, while mutant Q116K showed a significant (about 30-fold larger than that of S124D) effect. Again, as in the previous series, the double mutant showed the largest effect (Fig. 4F and *SI Appendix, Table S1*).

Summarizing, the quantitative oIEC assay confirmed the prominent dependence of Bep1_{FIC}* catalyzed target modification on the type of residue in target position 116 that had already been revealed by the radioactive endpoint assay and predicted by modeling (*SI Appendix, Fig. S3A*) but also demonstrated a significant influence of the residue in position 124, such that both salt bridges appear to be crucial for efficient Bep1-mediated AMPylation of Rac-subfamily GTPases.

Discussion

Single residue alterations in the effector loop (switch I region) of Ras-family GTPases can alter the specificity for interaction with downstream effectors in cellular signaling cascades (29). Several protein interaction modes have been described for Rho-family GTPases (30, 31), even though the basis of discrimination between these structurally conserved but functionally diverse GTPases remained elusive. The highly divergent Rho insert has been linked to a number of biological effects, such as membrane ruffling, Rho kinase activation by RhoA (32, 33), or the interaction of Rac with the NADPH oxidase complex (34). However, these studies relied on deletion of the Rho insert, and it is unclear if respective mutant proteins were properly folded. More recent structural work on complexes between Formins (mDia and FMNL2) and RhoC (35) or Cdc42 (36, 37) show the direct involvement of the C-terminal residues of the Rho insert in complex formation. While the Rho insert contributes only marginally to RhoC:mDia complex formation (35), it is crucial for interaction specificity in the FMNL2:Cdc42 complex (36). Our structure–function analysis substantially augments this body of work and demonstrates that target selectivity of Bep1 for Rac-subfamily GTPases is encoded by intermolecular interaction with a different set of Rho-family specific structural elements: Bep1 interacts with N-terminal residues of the Rho-insert helix as well as the G4 motif residues. The observation that Cdc42 cannot be converted fully to a Rac1-like Bep1 target by the respective residue substitutions suggests additional, yet unknown, structural or dynamic features that contribute to efficient AMPylation.

Remarkably, Bep1's selectivity is based by and large on a short insert of six residues in the conserved lid loop of the FIC domain (Fig. 2C). This simple, yet elegant, evolutionary treat equips *Bartonella* with a precise molecular tool to interfere specifically with host signaling. As such, Bep1 is the first bacterial effector to selectively target Rac-subfamily GTPases without affecting the Rho or Cdc42 GTPase subfamilies. Insertions of few amino acids in loop regions as exemplified by Bep1 are found in other Fic proteins; however, their functional consequences are hard to predict based on sequences alone. However, it is conceivable that they contribute to the specificity for different target spectra. Targeting a broad range of Rho GTPases seems to require a more complex addition to the FIC domain as exemplified by the arm domain found in IbpA or VopS (Fig. 3A and B).

We speculate that in the infection process of *Bartonella*, the selective inactivation of Rac-subfamily GTPases plays a critical role for the evasion of the innate immune response, without causing the collateral damage and activation of the immune system associated with effectors that target a broad-spectrum of

Rho GTPases, such as VopS or IbpA. In fact, Rac-subfamily selective AMPylation does not trigger a response of the innate immune system via activation of the pyrin inflammasome, which has been shown to accompany RhoA inactivation by covalent modification in the Sw1 region (38). Thus, avoiding RhoA inactivation may provide a substantial benefit for *Bartonella* to establish a largely asymptomatic chronic infection in their host.

Patients with impaired signaling of Rac-subfamily GTPases cannot clear bacterial infections due to diminished ability for ROS production in immune cells, as seen in patients suffering from chronic granulomatous disease or case studies from patients with dysfunctional Rac2 genes resulting in neutrophil immunodeficiency syndrome (39, 40). Along these lines, we speculate that selective targeting of GDP-complexed Rac-subfamily GTPases provides the additional benefit that protein levels of GDP-bound Rac are not down-regulated via proteasomal degradation (41), resulting in a stable pool of inactive Rac subfamily GTPases that would subdue Rac-mediated immune responses effectively.

Beyond providing a molecular understanding for target selectivity among Rho-family GTPases, the narrow target spectrum of Bep1 for Rac-subfamily GTPases also provides a unique tool for dissecting their specific functions in cellular processes, such as cytoskeletal rearrangements related to the Rac1-dependent formation of membrane ruffles, the Rac2/RhoG-dependent production of reactive oxygen in immune cells, or the role of Rac1 in carcinogenesis.

Considering the simple topology and small size of the FIC domain, we find a surprisingly modular division of functions. While the conserved catalytic core allows efficient AMPylation of a target hydroxyl residue located in an extended loop that registers to the active site via β -strand augmentation, target affinity and thereby selectivity is encoded separately in a short loop insertion. The modular nature and amenable size of this structural framework appears well suited for the rational design of synthetic Rho-subfamily selective FIC domain AMP transferases with novel physiological activities and beyond.

Materials and Methods

Protein Expression and Purification. The FIC domain of Bep1 was cloned, expressed and purified in complex with the inhibition-relieved regulatory protein BiaA_{E33G} as described for the crystallization construct and is subsequently referred to as Bep1_{FIC}*. For the generation of cleared bacterial lysate, the bacterial pellet was resuspended in reaction buffer (50 mM Tris-HCl, pH 8.0, 150 mM NaCl, 5 mM MgCl₂) supplemented with protease inhibitor mixture (complete EDTA-free mini, Roche) and lysed by sonication. After clearing the lysates by centrifugation (120,000 × g for 30 min at 4 °C), the supernatant was directly used in the assays or stored at –20 °C. Protein expression and purification of GST- or HIS-tagged GTPases and GST-tagged FIC domains of VopS and IbpA followed standard GST- or HIS-fusion-tag protocols. In short, *E. coli* BL21 or BL21 AI (Invitrogen) were transformed with expression plasmids and used for protein expression. Bacteria were grown in LB medium supplemented with appropriate antibiotic on a shaker until A₆₀₀ = 0.6 to 0.8 at 30 °C. Protein expression was induced by addition of 0.2 mM isopropyl- β -D-thiogalactopyranoside (IPTG) (AppliChem GmbH) or 0.1% wt/vol arabinose (Sigma-Aldrich) for 4 to 5 h at 22 °C.

Bacteria were harvested by centrifugation at 6,000 × g for 6 min at 4 °C, resuspended in lysis buffer (20 mM Tris-HCl, pH 7.5, 10 mM NaCl, 5 mM MgCl₂, 1% Triton X-100, 5 mM DTT and protease inhibitor mixture [protease Mini EDTA-free, Roche]), and lysed using a French press (Thermo Fisher). After ultracentrifugation at 120,000 × g for 20 min at 4 °C the cleared lysate of GST-tagged GTPases was added to equilibrated glutathione-Sepharose resin (Genescript) and incubated for 1 h at 4 °C on a turning wheel. After four washing steps with wash buffer (20 mM Tris-HCl, pH 7.5, 10 mM NaCl, 5 mM MgCl₂) the bound protein was eluted with wash buffer supplemented with 10 mM reduced glutathione (Sigma-Aldrich).

Cleared lysate of HIS-tagged GTPases was injected on HisTrap HP columns (GE Healthcare) after equilibration with binding buffer (50 mM Hepes, pH 7.5, 150 mM NaCl, 5 mM MgCl₂, 20 mM imidazole). Washing with 10 column volumes of binding buffer was followed by elution with 5 column volumes of elution buffer (50 mM Hepes, pH 7.5, 150 mM NaCl, 5 mM MgCl₂, 500 mM imidazole). HIS-tagged GTPases were incubated with 50 mM EDTA and further

purified by size exclusion chromatography (HiLoad 16/600 Superdex 75 pg, GE Healthcare) with SEC buffer (50 mM Hepes, pH 7.5, 150 mM NaCl, 5 mM MgCl₂, 50 mM EDTA). EDTA was removed by buffer exchange (50 mM Hepes, pH 7.5, 150 mM NaCl, 5 mM MgCl₂) and the protein used for quantitative AMPylation assays.

Nucleotide Loading of GTPases. To preload purified GTPases with the respective nucleotide, 50 μM protein was incubated with 3 mM nucleotide (GDP, GTP, GTPγS, or GMP-PNP) and 8 mM EDTA in reaction buffer (50 mM Tris-HCl, pH 8.0, 150 mM NaCl, 5 mM MgCl₂) for 20 min at room temperature. Then 16 mM MgCl₂ was added to stop the nucleotide exchange. The protein was then used for both in vitro AMPylation assays.

Radioactive AMPylation Assay. The in vitro AMPylation activity was assayed using either cleared bacterial lysates expressing full-length Bep1 or purified FIC domains of Bep1, VopS, and IbpA.

To analyze the AMPylation activity of Bep1, Bep1_{FIC}^{*}, VopS_{FIC}, and IbpA_{FIC2}, 10 μM purified GTPase, preloaded with respective nucleotide, was incubated in presence of the respective AMPylator with 10 μCi [³²P]-ATP (Hartmann Analytic) in reaction buffer (50 mM Tris-HCl, pH 8.0, 150 mM NaCl, 5 mM MgCl₂ containing 0.2 mg/mL RNaseA) for 1 h at 30 °C. The reaction was stopped by addition of SDS-sample buffer and heating to 95 °C for 5 min. Samples were separated by SDS-PAGE and subjected to autoradiography.

For AMPylation of Rac1, Cdc42, and their mutant variants, 5 μM of purified HIS-tagged GTPases, preloaded with GDP, were incubated with Bep1_{FIC}^{*} (1 and 5 μM in Rac1 and Cdc42 variants, respectively) in the presence of [³²P]-ATP (Hartmann Analytic) for 40 min in reaction buffer (50 mM Tris-HCl, pH 8.0, 150 mM NaCl, 5 mM MgCl₂) at 20 °C.

Quantitative AMPylation Assay. We employed an oEC assay, monitoring the UV absorption of GTPase targets at 260 nm. The observed increase in absorbance due to AMPylation could be readily quantified and resulted in progress curves that yielded reaction velocities and in turn AMPylation efficiencies (k_{cat}/K_M).

A 1-mL Resource Q column (GE Healthcare) was equilibrated with loading buffer (20 mM Tris/HCl, pH 8.5 or 6.5 for Rac1 or Cdc42, respectively). The purified GTPase variant was mixed with Bep1_{FIC}^{*} in reaction buffer (50 mM Tris-HCl, pH 7.5, 150 mM NaCl, 5 mM MgCl₂) in a large volume (200 μL), and the reaction was started at $t = 0$ by addition of 3.2 mM ATP (final concentration, supplemented with 6.4 mM MgCl₂). A small fraction (20 μL) of the reaction mixture was injected automatically on the column at intervals of 6 min. After washing with loading buffer, a gradient of elution buffer [1 M (NH₄)₂SO₄ in loading buffer] was applied, yielding a chromatogram for each injection.

Reaction progress was monitored by quantification of GTPase peak area measured at 260 nm from each chromatogram by numerical peak integration. Note that this peak comprised both native and AMPylated GTPase. A heuristic quadratic function was fitted to the progress curves to yield the initial velocity. Calibration with ATP samples of known concentrations allowed to derive absolute AMPylation velocities. Enzymatic K_M and k_{cat} parameters were derived from $v_{initial}(S)$ type Michaelis-Menten plots (SI Appendix, Fig. S4 F and G). Depending on the activity, Bep1_{FIC}^{*} concentrations were chosen such that the enzyme velocities were kept within a similar range (SI Appendix, Fig. S4 H and I). Nominal GTPase concentrations were corrected based on the back-extrapolated peak absorbance at $t = 0$. Fitting of single-substrate kinetic measurements by the Michaelis-Menten equation was developed in python 3 with standard modules provided in the Anaconda distribution.

Crystallization and Structure Determination. The full-length *biaA* gene that codes for the small ORF directly upstream of *bep1* gene and part of the *bep1* gene from *B. rochalimae* encoding the FIC domain (amino acid residues 13 to 229) were PCR amplified from genomic DNA. The PCR products for *biaA* and the fragment of *bep1* were cloned into the vector pRSF-Duet1. pRSF-Duet1 containing *biaA* or *bep1* were introduced into *E. coli* BL21 (DE3) by transformation. The constructs were expressed and purified as described for VbhA/VbhT(FIC) (20) with the difference that 5 mM DTT was additionally used throughout the purification procedure. Fractions were pooled and concentrated to 13.6 mg mL⁻¹ for crystallization.

Crystals were obtained at 4 °C using the hanging-drop vapor diffusion method upon mixing 1 μL protein solution with 1 μL reservoir solution. The reservoir solution was composed of 0.2 M Hepes (pH 7.5), 2.3 M ammonium sulfate, and 2% vol/vol PEG 400. For data collection, crystal was frozen in liquid nitrogen without additional cryoprotectant. Diffraction data were

collected on beam-line X065A (PXIII) of the Swiss Light Source ($\lambda = 1.0 \text{ \AA}$) at 100 K on a MAR CCD detector. Data were processed with XDS and the structure solved by molecular replacement with Phaser (42) using the VbhA/VbhT(FIC) structure (PDB 3SHG) as search model. Several rounds of iterative model building and refinement were performed using Coot (43) and Buster (44), respectively. The final structure shows high similarity to the VbhA/VbhT(FIC) structure (rmsd 1.44 Å for 183 C α positions). Crystallographic data are given in SI Appendix, Table S3. Figs. 2 A–C and 3 A–D and SI Appendix, Figs. S2 B and D–F and S3A have been generated using Pymol (45).

Homology Modeling of the Bep1:Target Complex and Generation of Structure-Based Sequence Alignments. The input structure for homology modeling was chosen from all available Rac-subfamily structures (i.e., Rac1-3 and RhoG). In total, 43 PDB entries were analyzed (SI Appendix, Table S4). Cdc42 (chain D) of the IbpA-Cdc42 complex served as reference for all superimpositions. The superimposition was carried out in two steps: a global superimposition over all C α atom positions and a second, local superimposition using all atom positions of residues 27 to 37 (Sw1) of Cdc42. Both steps used the align-algorithm implemented in Pymol (version 1.8) with standard settings.

We observed high structural agreement between Rac-subfamily GTPase structures in the PDB and the reference chain with an average C α rmsd below 0.5 Å. In contrast, we noticed large variations in the all-atom rmsds of residues in the Sw1 region that correlate with the nucleotide state of the GTPase. In order to find the most suitable PDB for homology modeling we searched for the smallest coordinate deviations to the Sw1 conformation of the Cdc42 reference chain: three GDP-loaded GTPase structures display an rmsd of coordinates to the template below 1 Å (SI Appendix, Table S4). Two of these structures are complexes of the Rho-GDP-dissociation inhibitor (RhoGDI) with either Rac1 (PDB ID 1hh4) or Rac2 (PDB ID 1ds6) representing the cytosolic storage form of the GTPases. The third structure is the Zn²⁺-bound trimeric form of Rac1 (PDB: 2P2L), in which Sw1 is involved in the Zn²⁺-mediated trimer interface. From these candidate PDBs, we chose 1ds6 as the most appropriate for homology modeling since it represents a physiological state of a Rac-GTPase (in contrast to 2P2L). Further, 1ds6 features a fully resolved Sw1 region and a higher resolution compared to entry 1hh4. To correspond closely to the reference structure, we built an alternative standard rotamer for the solvent-exposed Y32 of Rac2 in the PDB 1ds6 (Fig. 3C). The FIC domains of Bep1 and IbpA were superimposed using the C- α atom positions of flap residues that adopt β -sheet-like conformations in order to mimic the catalytically active conformation of the IbpA:Cdc42 complex. Superimposing IbpA_{FIC2} residues 3,667 to 3,670 and 3,673 to 3,677, corresponding to Bep1 residues 110 to 113 and 122 to 126, respectively, yields an rms error of 0.87 Å for 9 CA pairs.

Modeling of the complex structure was carried out using the manually selected, superimposed, and curated model described above as starting structure for an adapted flexDDG protocol (26) implemented in the Rosetta package. In short, ligands (GDP and hydrated Mg²⁺) and ordered water molecules (as found in PDB entry 1ds6, as well as one water molecule in the center of the Bep1 flap, shown in Fig. 2B) that are part of the protein complex interface were parameterized for the use in Rosetta and included in the modeling process to increase precision and validity of the resulting models. The selected small molecules had been refined with B factors that are comparable to neighboring main chain atoms in the respective PDB entries (1ds6 and 5eu0). Next, the curated input model is subjected to a global minimization of backbone and side chain torsions in Rosetta (Minimize step) followed by local sampling of backbone and side chain degrees of freedom for all residues with C- β atoms within 10 Å distance of Rac2 residue D124 (Backrub step). The side chains of the resulting models are optimized globally (Packing step), and backbone and side chain torsion energies are minimized globally (Minimize step 2). Finally, models are scored on the all-atom level using the suggested *talariis_2014* function (26), and best scoring models were analyzed visually. The recommended total of 35 independent simulations is calculated for the complex with a maximum number of 5,000 minimization iterations (convergence limit score 1.0) and 35,000 backrub trial steps each.

Structure guided multiple sequence alignments (MSA) were generated by manual adjustment of MSA generated using the ClustalW algorithm as implemented in the GENEIOUS software package (46) version 7.1.7.

Quantification and Statistical Analysis. Statistical parameters are given in SI Appendix, Tables S1 and S2. Error bars in quantitative AMPylation assays show the SD of reaction efficiencies (k_{cat}/K_M) derived from the least-square minimization of the fitting routine.

Dietz et al.

Structural basis for selective AMPylation of Rac-subfamily GTPases by *Bartonella* effector protein 1 (Bep1)

PNAS | 7 of 8
https://doi.org/10.1073/pnas.2023245118

Data and Software Availability. Data analysis of oIEC was performed with python3 scripts made available under https://github.com/FicTeam/HuberDietz_PNAS21. Protein structure data have been deposited in Protein Data Bank under accession number 5EU0.

ACKNOWLEDGMENTS. We thank the laboratories of Klaus Aktories, Kim Orth, and Seema Mattoo for providing expression constructs of Rho-family

GTPases, VopS, and IbpA, respectively. We thank the beamline staff at the Swiss Light Source in Villigen for expert help in data acquisition. Rosetta modelling calculations were performed at scICORE (<https://scicore.unibas.ch/>) scientific computing core facility at University of Basel. This work was supported by grant 310030A_173119 from the Swiss National Science Foundation (<http://www.snf.ch/en/Pages/default.aspx>) and advanced grant 340330 (FicModFun) from the European Research Council, both to C.D.

- J. Didsbury, R. F. Weber, G. M. Bokoch, T. Evans, R. Snyderman, *rac*, a novel ras-related family of proteins that are botulinum toxin substrates. *J. Biol. Chem.* **264**, 16378–16382 (1989).
- K. Wennerberg, K. L. Rossman, C. J. Der, The Ras superfamily at a glance. *J. Cell Sci.* **118**, 843–846 (2005).
- A. B. Jaffe, A. Hall, Rho GTPases: Biochemistry and biology. *Annu. Rev. Cell Dev. Biol.* **21**, 247–269 (2005).
- S. J. Heasman, A. J. Ridley, Mammalian Rho GTPases: New insights into their functions from in vivo studies. *Nat. Rev. Mol. Cell Biol.* **9**, 690–701 (2008).
- G. M. Bokoch, B. A. Diebold, Current molecular models for NADPH oxidase regulation by Rac GTPase. *Blood* **100**, 2692–2696 (2002).
- A. E. Karnoub, M. Symons, S. L. Campbell, C. J. Der, Molecular basis for Rho GTPase signaling specificity. *Breast Cancer Res. Treat.* **84**, 61–71 (2004).
- K. Aktories, Bacterial protein toxins that modify host regulatory GTPases. *Nat. Rev. Microbiol.* **9**, 487–498 (2011).
- K. Aktories, Rho-modifying bacterial protein toxins. *Pathog. Dis.* **73**, ftv091 (2015).
- A. Wagner, C. Dehio, Role of distinct type-IV-secretion systems and secreted effector sets in host adaptation by pathogenic *Bartonella* species. *Cell. Microbiol.* **21**, e13004 (2019).
- A. Harms, C. Dehio, Intruders below the radar: Molecular pathogenesis of *Bartonella* spp. *Clin. Microbiol. Rev.* **25**, 42–78 (2012).
- A. Harms et al., Evolutionary dynamics of pathoadaptation revealed by three independent acquisitions of the VirB/D4 type IV secretion system in *Bartonella*. *Genome Biol. Evol.* **9**, 761–776 (2017).
- A. Harms, F. V. Stanger, C. Dehio, Biological diversity and molecular plasticity of Fic domain proteins. *Annu. Rev. Microbiol.* **70**, 341–360 (2016).
- C. Hedberg, A. Itzen, Molecular perspectives on protein adenylylation. *ACS Chem. Biol.* **10**, 12–21 (2015).
- S. Mattoo et al., Comparative analysis of *Histophilus somni* immunoglobulin-binding protein A (IbpA) with other fic domain-containing enzymes reveals differences in substrate and nucleotide specificities. *J. Biol. Chem.* **286**, 32834–32842 (2011).
- C. A. Worby et al., The fic domain: Regulation of cell signaling by adenylylation. *Mol. Cell* **34**, 93–103 (2009).
- M. L. Yarbrough et al., AMPylation of Rho GTPases by *Vibrio* VopS disrupts effector binding and downstream signaling. *Science* **323**, 269–272 (2009).
- C. R. Roy, J. Cherfils, Structure and function of Fic proteins. *Nat. Rev. Microbiol.* **13**, 631–640 (2015).
- R. Schulein et al., A bipartite signal mediates the transfer of type IV secretion substrates of *Bartonella henselae* into human cells. *Proc. Natl. Acad. Sci. U.S.A.* **102**, 856–861 (2005).
- A. Wagner, C. Tittes, C. Dehio, Versatility of the BID domain: Conserved function as type-IV-secretion-signal and secondarily evolved effector functions within *Bartonella*-infected host cells. *Front. Microbiol.* **10**, 921 (2019).
- P. Engel et al., Adenylylation control by intra- or intermolecular active-site obstruction in Fic proteins. *Nature* **482**, 107–110 (2012).
- J. Xiao, C. A. Worby, S. Mattoo, B. Sankaran, J. E. Dixon, Structural basis of Fic-mediated adenylylation. *Nat. Struct. Mol. Biol.* **17**, 1004–1010 (2010).
- K. Lapouge et al., Structure of the TPR domain of p67phox in complex with Rac.GTP. *Mol. Cell* **6**, 899–907 (2000).
- P. Luong et al., Kinetic and structural insights into the mechanism of AMPylation by VopS Fic domain. *J. Biol. Chem.* **285**, 20155–20163 (2010).
- A. Goepfert, F. V. Stanger, C. Dehio, T. Schirmer, Conserved inhibitory mechanism and competent ATP binding mode for adenylyltransferases with Fic fold. *PLoS One* **8**, e64901 (2013).
- A. Wittinghofer, I. R. Vetter, Structure-function relationships of the G domain, a canonical switch motif. *Annu. Rev. Biochem.* **80**, 943–971 (2011).
- K. A. Barlow et al., Flex ddG: Rosetta Ensemble-based estimation of changes in protein-protein binding affinity upon mutation. *J. Phys. Chem. B* **122**, 5389–5399 (2018).
- G. T. Gapp et al., Control of protein signaling using a computationally designed GTPase/GEF orthogonal pair. *Proc. Natl. Acad. Sci. U.S.A.* **109**, 5277–5282 (2012).
- A. G. Marangoni, *Enzyme Kinetics: A Modern Approach* (Wiley, Hoboken, NJ, 2002).
- C. Herrmann, Ras-effector interactions: After one decade. *Curr. Opin. Struct. Biol.* **13**, 122–129 (2003).
- I. R. Vetter, A. Wittinghofer, The guanine nucleotide-binding switch in three dimensions. *Science* **294**, 1299–1304 (2001).
- R. Dvorsky, M. R. Ahmadian, Always look on the bright side of Rho: Structural implications for a conserved intermolecular interface. *EMBO Rep.* **5**, 1130–1136 (2004).
- A. E. Karnoub, C. J. Der, S. L. Campbell, The insert region of Rac1 is essential for membrane ruffling but not cellular transformation. *Mol. Cell. Biol.* **21**, 2847–2857 (2001).
- H. Zong, K. Kaibuchi, L. A. Quilliam, The insert region of RhoA is essential for Rho kinase activation and cellular transformation. *Mol. Cell. Biol.* **21**, 5287–5298 (2001).
- J. L. Freeman, J. D. Lambeth, NADPH oxidase activity is independent of p47phox in vitro. *J. Biol. Chem.* **271**, 22578–22582 (1996).
- R. Rose et al., Structural and mechanistic insights into the interaction between Rho and mammalian Dia. *Nature* **435**, 513–518 (2005).
- S. Kühn et al., The structure of FMNL2-Cdc42 yields insights into the mechanism of lamellipodia and filopodia formation. *Nat. Commun.* **6**, 7088 (2015).
- M. Lammers, S. Meyer, D. Kühlmann, A. Wittinghofer, Specificity of interactions between mDia isoforms and Rho proteins. *J. Biol. Chem.* **283**, 35236–35246 (2008).
- H. Xu et al., Innate immune sensing of bacterial modifications of Rho GTPases by the Pyrin inflammasome. *Nature* **513**, 237–241 (2014).
- D. R. Ambruso et al., Human neutrophil immunodeficiency syndrome is associated with an inhibitory Rac2 mutation. *Proc. Natl. Acad. Sci. U.S.A.* **97**, 4654–4659 (2000).
- A. G. Kurkchubasche, J. A. Panepinto, T. F. Tracy, Jr, G. W. Thurman, D. R. Ambruso, Clinical features of a human Rac2 mutation: A complex neutrophil dysfunction disease. *J. Pediatr.* **139**, 141–147 (2001).
- E. A. Lynch, J. Stall, G. Schmidt, P. Chavrier, C. D'Souza-Schorey, Proteasome-mediated degradation of Rac1-GTP during epithelial cell scattering. *Mol. Cell. Biol.* **17**, 2236–2242 (2006).
- A. J. McCoy et al., Phaser crystallographic software. *J. Appl. Cryst.* **40**, 658–674 (2007).
- P. Emsley, B. Lohkamp, W. G. Scott, K. Cowtan, Features and development of Coot. *Acta Crystallogr. D Biol. Crystallogr.* **66**, 486–501 (2010).
- G. Bricogne et al., BUSTER version X.Y.Z. Cambridge (Global Phasing Ltd., United Kingdom, 2016).
- J. Siebourg-Polster et al., NEMix: Single-cell nested effects models for probabilistic pathway stimulation. *PLoS Comput. Biol.* **11**, e1004078 (2015).
- M. Kearse et al., Geneious Basic: An integrated and extendable desktop software platform for the organization and analysis of sequence data. *Bioinformatics* **28**, 1647–1649 (2012).

Supplementary Information for

**Structural basis for selective AMPylation of Rac subfamily GTPases by
Bartonella effector protein 1 (Bep1)**

Nikolaus Dietz^{a,1}, Markus Huber^{a,1}, Isabel Sorg^a, Arnaud Goepfert^{a,2}, Alexander Harms^a,
Tilman Schirmer^{a,3}, and Christoph Dehio^{a,3}

^aBiozentrum, University of Basel, Basel, Switzerland

¹N.D. and M.H. contributed equally to this work

²Present address: Ichnos Sciences Biotherapeutics SA, Epalinges, Switzerland.

³To whom correspondence should be addressed.

Email: christoph.dehio@unibas.ch or tilman.schirmer@unibas.ch

This PDF file includes:

Supplementary text and detailed Materials and Methods

Figures S1 to S4

Tables S1 to S4

Supplementary information References

2

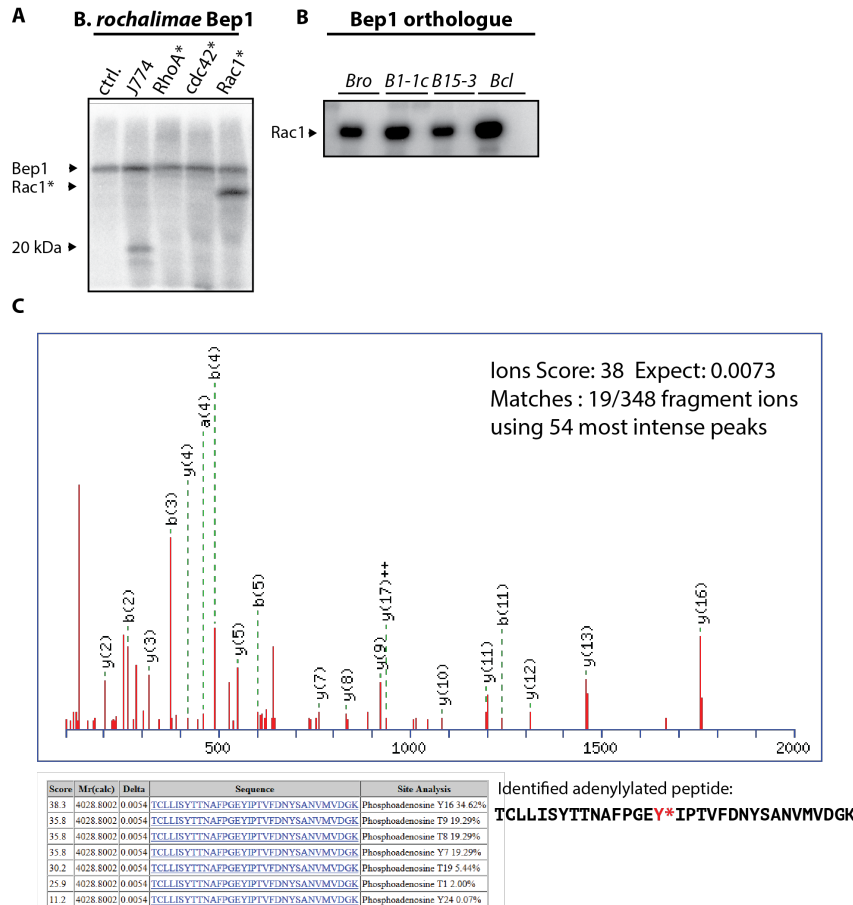


Figure S1. Figure S1 (A) Autoradiograms of Bep1 AMPylation reactions with [α - 32 P] labelled ATP. Bep1 AMPylates an approximately 20 kDa target in J774 cell lysate, indicative of modification of a small GTPase. Lane labelled ctrl. shows no signal for Bep1 only. Incubation E coli lysate containing Bep1 with E coli lysate containing GST-fusions of small GTPases (RhoA*, cdc42* and Rac*, 50kD) show incorporation of radioactive ATP in Rac* only. Automodification of Bep1 is detected at 70kD. **(B)** *In vitro* AMPylation activity showing

conserved function in Bep1 orthologues of *B. rochalimae* (*Bro*), *Bartonella* sp. 1-1c (*B1-1c*), *Bartonella* sp. AR15-3 (*B15-3*), *Bartonella clarridgeiae* (*Bcl*). **(C)** Identification of the modified peptide by mass spectrometry. Sequence of the identified peptide after tryptic digestion carrying the AMPylation site. The modification is located at tyrosine 16 of the peptide (in red and indicated by an asterisk), corresponding to tyrosine 32 of Rac1.

4

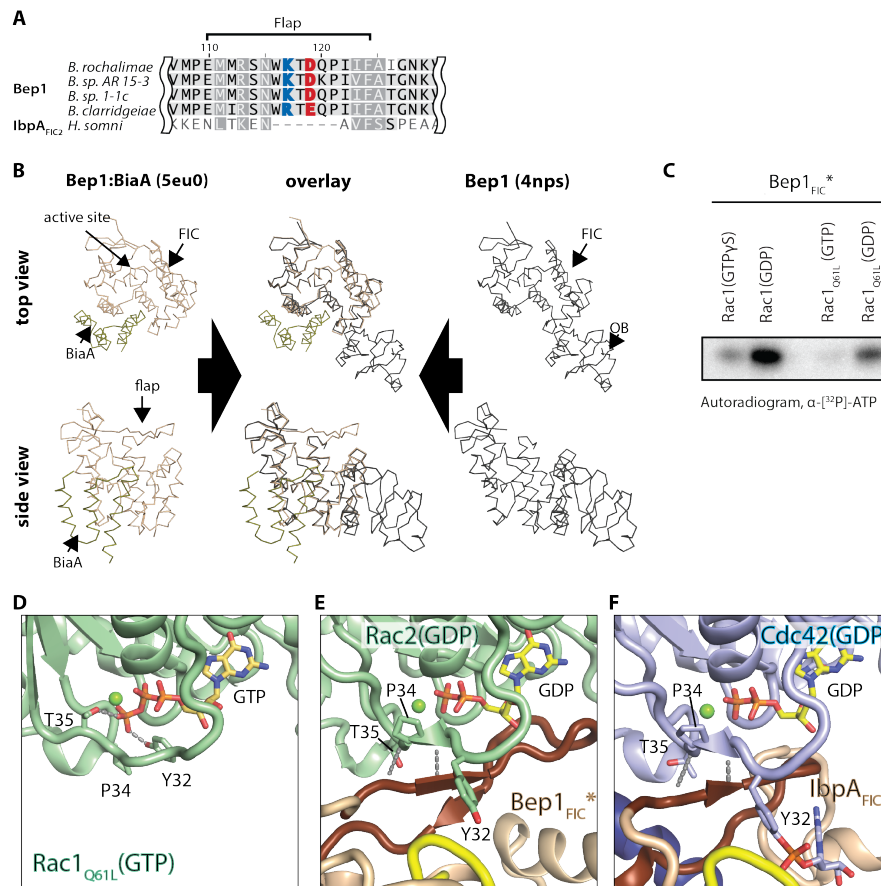


Figure S2. Bep1_{FIC}* conformation is not influenced by BiaA binding and allows interaction with GDP-loaded targets. (A) Sequence alignment of flaps found in Bep1 orthologues and IbpA_{FIC2}. **(B)** Analysis of BiaA-induced conformational changes in Bep1_{FIC}*. Binding of BiaA_{E22G} to Bep1 does not result in detectable conformational changes in the FIC domain as indicated by very small coordinate differences between free (PDB ID: 4nps of *B. clarridgeiae*) and BiaA-bound Bep1 (PDB ID: 5eu0 of *B. rochalimae*): CA-Coordinate differences for the entire FIC core comprising helices 1 - 5 is 0.37Å (151 CA pairs in residues 42-192) with a even smaller deviation the catalytic core (residues 151-191 comprising FIC

helices 4-5, RMSD: 0.23Å, 41 CA pairs). **(C)** Nucleotide dependence of FIC-mediated Rho GTPase AMPylation. Significant Bep1-mediated AMPylation is observed for GDP-loaded Rac1, but not for GTPγS-loaded Rac1 or GTP-loaded, hydrolysis deficient, Rac1_{Q61L} mutant (crystal structure shown in panel (D)). Conformation of the switch 1 (Sw1) loop in crystal structures of **(D)** GTP-bound Rac1_{Q61L} and **(E)** GDP-bound Rac2 modelled in complex with Bep1 (GTPase PDB codes are 1e96 and 1ds6, respectively). Notably, Sw1 is in an inward facing conformation in the GTP-bound state shown in (D). Y32 (black diamond) is coordinated by the γ-phosphate of the GTPase-bound nucleotide (hydroxyl groups in hydrogen-bonding distance) and is thus inaccessible for modification. In contrast, Sw1 adopts an outward facing conformation in the GDP-bound state shown in (E), rendering Y32 solvent accessible. **(F)** Conformation of Sw1 in the product complex between IbpA_{FIC2} and Cdc42 in the GDP-bound state that permits the interaction.

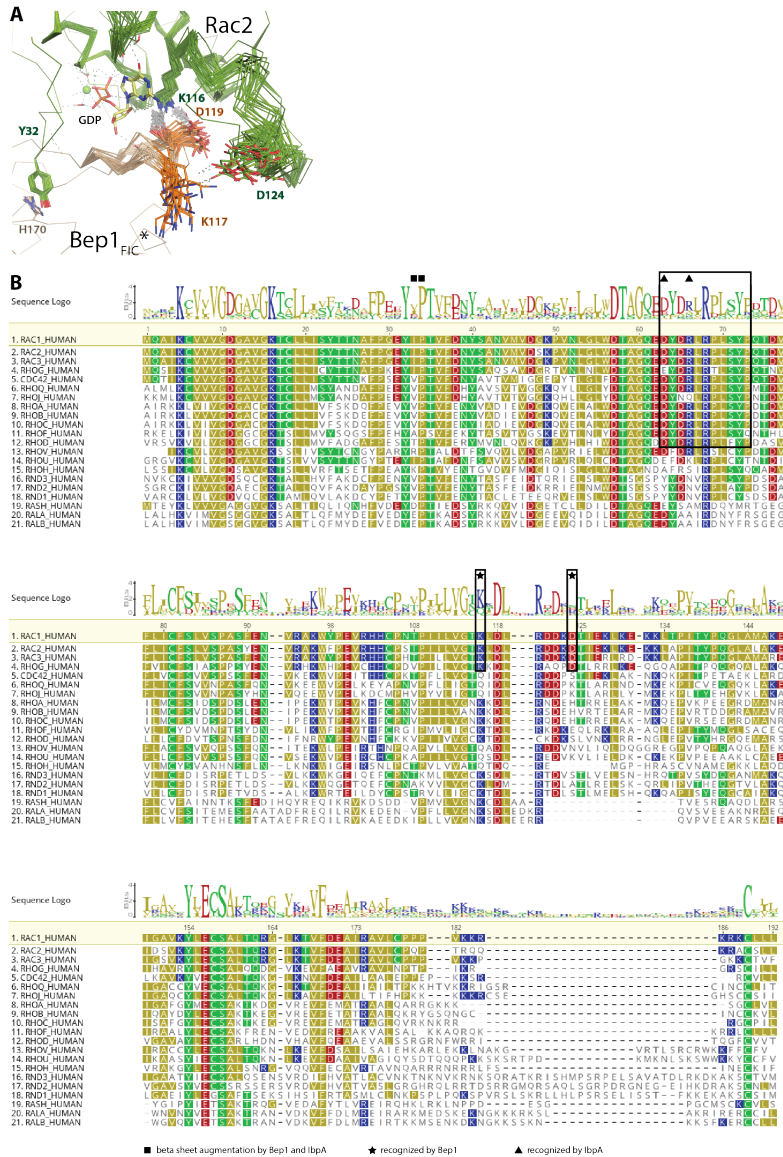


Figure S3. Proposed Rac subfamily GTPase interaction sites for Bep1-mediated AMPylation. (A) Ensemble of Bep1_{FIC}:Rac2 models. Bep1_{FIC} (beige) and Rac2 (green) backbones are drawn as wires. Important residues are drawn as sticks. Salt-bridges

between Bep1_{D119}:Rac1_{K116} and Bep1_{K117}:Rac1_{D124} are indicated as dotted lines (grey). 25 representative calculations are shown. **(B)** Structure based protein sequence alignment of Rho-GTPases. Side-chain specific interactions with IbpA and Bep1 are indicated by triangles and asterisks, respectively. Interfaces between IbpA and Bep1 and their targets are illustrated as rectangular frames. Residues involved in β -sheet augmentation are marked with squares. Rac1 is set as reference sequence. Polar residues are coloured in green, negatively charged residues in red, positively charged residues in blue and hydrophobic residues in olive.

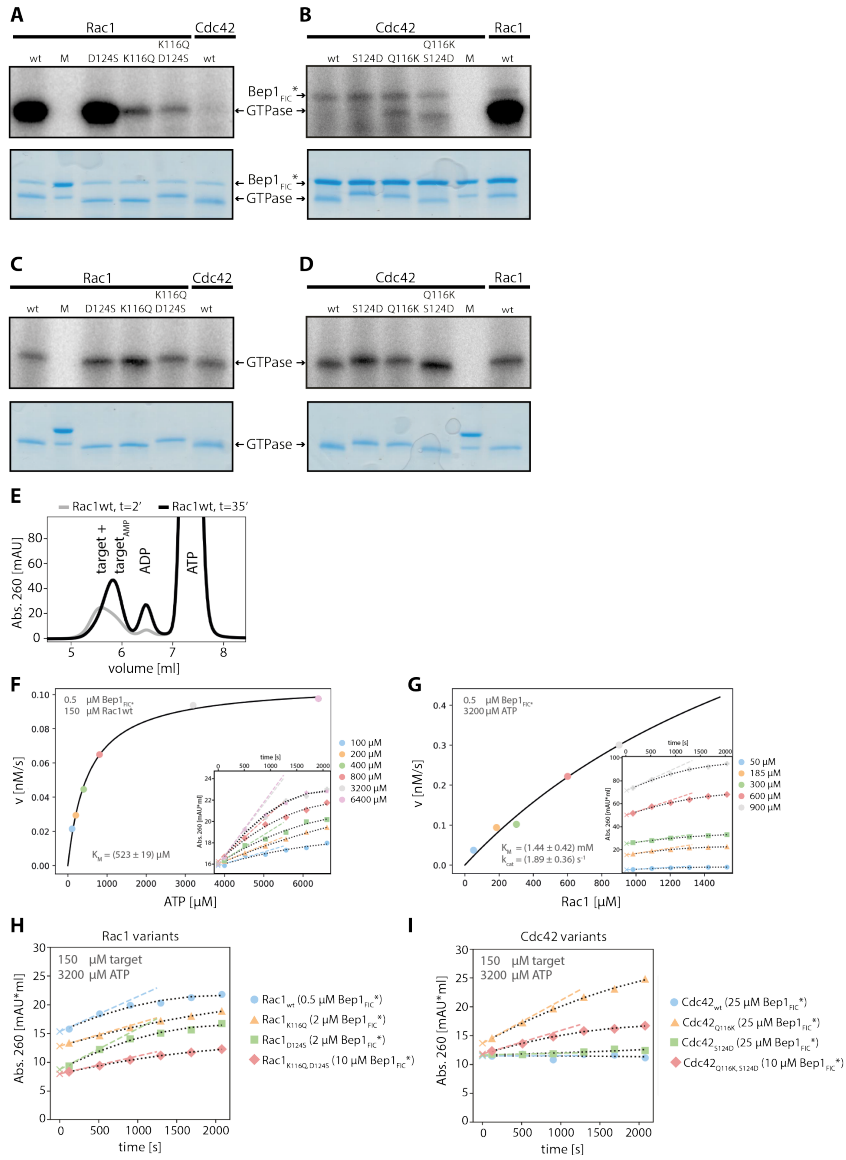


Figure S4. Bep1-mediated AMPylation of GTPase variants as measured by autoradiography and oIEC. (A – D) Autoradiograms and SDS-gels of Rac1 and Cdc42 variants after incubation with ³²P-α-ATP and respective AMP-transferases for 40 minutes.

(A) Rac1 variants and (B) Cdc42 variants after incubation with Bep1_{FIC}*. (C) Rac1 variants and (D) Cdc42 variants after concurrent incubation with lbpA_{FIC2}. 25 kDa and 20 kDa bands of Precision Plus Protein Standard (Bio-Rad) are visible in all SDS-gels between Rac1_{wt} and the rest of the GTPase variants (lanes labeled 'M'). (E) Ion exchange elution profiles for wild-type Rac1 (Rac1_{wt}) at t = 2' (grey) and t = 35' (black), demonstrating the increase in target/target-AMP absorption with time. (F, G) Michaelis-Menten plots for the Rac1 + ATP → Rac1-AMP + PPi reaction. Initial reaction rates as a function of ATP and Rac1 concentration are shown in panels (F) and (G), respectively. Initial velocities have been derived from the progress curves shown in the insets. (H, I) Progress curves of Bep1_{FIC}* mediated AMPylation of Rac1 (H) and Cdc42 (I) variants. Data points show the absorbance at 260 nm of the target/target-AMP peak during the time course. Heuristic fits are indicated as dotted lines (black). Initial velocities are derived from the first derivatives of the fit-function back-extrapolated to t = 0 and drawn as dashed lines in respective colors.

Table S1: Efficiency values for FIC-mediated AMPylation of Rho-GTPase variants.

Enzyme	Target	$k_{cat}/K_{M, target}$ [s ⁻¹ mM ⁻¹]	$K_{M, ATP}$ [mM]	$K_{M, target}$ [mM]	k_{cat} [s ⁻¹]
VopS_{FIC}	Cdc42_{Q61L}	100 ± 25 ¹	0.160 ± 0.02 ²	0.180 ± 0.04 ²	18 ± 1.5 ²
IbpA_{Fic2}	Cdc42_{Q61L}	162 ± 19 ¹	0.73 ± 0.04 ³	1.57 ± 0.15 ³	255 ± 15 ³
Bep1_{Fic}[*]	Rac1_{wt}	1.31 ± 0.46 ¹	0.52 ± 0.02 ⁴	1.44 ± 0.42 ⁴	1.89 ± 0.36 ⁴
	Rac1_{wt}	1.18 ± 0.20 ⁵			
	Rac1_{D124S}	0.481 ± 0.067 ⁵			
	Rac1_{K116Q}	0.202 ± 0.009 ⁵			
	Rac1_{K116Q, D124S}	0.043 ± 0.002 ⁵			
	Cdc42_{Q116K, S124D}	0.046 ± 0.003 ⁵			
	Cdc42_{Q116K}	0.028 ± 0.002 ⁵			
	Cdc42_{S124D}	0.001 ± 0.002 ⁵			
	Cdc42_{wt}	below detection			

¹ derived from k_{cat} and $K_{M, target}$

² taken from (1)

³ taken from (2)

⁴ derived from Figs. S4G and F

⁵ derived from v_{init} values measured by oIEC (see Figs. S4H and I).

Table S2: Relative change in free energy of Bep1_{Fic}* - Rac1 binding upon Rac1 mutation.

Target	k_{cat}/K_M ¹⁾ [s ⁻¹ ·mM ⁻¹]	$\Delta\Delta G = \Delta G_{wt} - \Delta G_{mut}$ ²⁾ [J·mol ⁻¹]	$\Delta\Delta G_{double\ mut} / \sum(\Delta\Delta G_{single\ mut})$
Rac1_{wt}	1.18 ± 0.20	0	
Rac1_{D124S}	0.481 ± 0.067	2225 ± 765	1.24 ± 0.33
Rac1_{K116Q}	0.202 ± 0.009	4375 ± 531	
Rac1_{K116Q, D124S}	0.043 ± 0.002	8210 ± 535	

¹⁾ taken from Table S1

$$\Delta\Delta G = \Delta G_{mut} - \Delta G_{wt} = R \times T \times \ln(K_{M,mut}) - R \times T \times \ln(K_{M,wt})$$

Since $K_{M,x} = \frac{K_{M,x}}{k_{cat,x}} \times k_{cat,x}$,

$$\ln(K_{M,x}) = \ln\left(\frac{K_{M,x}}{k_{cat,x}}\right) + \ln(k_{cat,x}) = -\ln\left(\frac{k_{cat,x}}{K_{M,x}}\right) + \ln(k_{cat,x})$$

Therefore,

$$\Delta\Delta G = R \times T \times \left[-\ln\left(\frac{k_{cat,mut}}{K_{M,mut}}\right) + \ln(k_{cat,mut}) + \ln\left(\frac{k_{cat,wt}}{K_{M,wt}}\right) - \ln(k_{cat,wt}) \right],$$

which, under the assumption of $k_{cat,mut} = k_{cat,wt}$, simplifies to

$$\Delta\Delta G = R \times T \times \left[-\ln\left(\frac{k_{cat}}{K_{M,mut}}\right) + \ln\left(\frac{k_{cat}}{K_{M,wt}}\right) \right] = R \times T \times \ln\left(\frac{\frac{k_{cat}}{K_{M,wt}}}{\frac{k_{cat}}{K_{M,mut}}}\right)$$

$$T = 298.15\ K$$

Table S3: Crystallographic data collection and refinement statistics of Bep1_{FIC}:BiaA complex

Bep1 _{FIC} :BiaA (5eu0)	
Data collection	
Space group	P 4 ₃ 2 ₁ 2
Cell dimensions	
<i>a</i> , <i>b</i> , <i>c</i> (Å)	73.13, 73.13, 130.15
α , β , γ (°)	90, 90, 90
Resolution (Å)	29.7 - 1.6 (1.7 - 1.6) ^a
<i>R</i> _{sym}	14.0% (164.5%)
<i>I</i> / σ (<i>I</i>)	16.52 (1.43)
<i>CC</i> _{1/2}	1.0 (0.53)
Completeness (%)	100% (99.0%)
Redundancy	11.6 (9.9)
Refinement	
Resolution (Å)	29.7 - 1.6
No. reflections	47278
<i>R</i> _{work} / <i>R</i> _{free}	0.189 (0.211)
No. atoms	
Protein	2166
Ion	10
Water	271
<i>B</i> factors	
Protein	23.99
Ion	40.54
Water	34.37
R.m.s. deviations	
Bond lengths (Å)	0.014
Bond angles (°)	0.88

^a Values in parentheses are for highest-resolution shell.

Table S4: Global and local structural alignment of Rac-subfamily GTPases to AMPylated Cdc42 in the IbpA bound complex (chain B of PDB entry 4ITR).

Chain A of PDB entry 1DS6 was chosen for complex modelling.

NUCLEOTIDE (ANALOGUE)	PDB ID	GLOBAL RMSD (CA)[Å]	# PAIRS (CA)	USED	LOCAL RMSD (SW1) [Å]	# PAIRS (ATOMS)	USED
GDP	1HH4	0.534	177	158	0.526	85	61
GDP	2P2L	0.420	172	133	0.781	91	72
GDP	1DS6	0.439	175	151	0.827	91	65
GDP	2H7V	0.453	175	139	1.050	91	75
GDP	2W2T	0.412	173	144	1.867	81	68
GDP	2G0N	0.335	175	133	1.891	82	67
GDP	2C2H	0.411	165	132	1.955	48	42
GDP	1I4D	0.517	172	135	2.419	91	72
GDP	1I4L	0.613	173	152	2.511	91	77
GDP	1RYF	0.392	161	124	3.693	89	87
GSP	2W2V	0.383	171	138	1.973	91	74
GSP	2W2X	0.558	167	135	3.546	87	77
GSP	4GZM	0.492	174	139	4.116	91	89
GSP	2FJU	0.391	173	130	4.169	91	87
GNP	2IC5	0.357	175	133	1.608	88	66
GNP	1I4T	0.595	173	147	2.520	91	74
GNP	1RYH	0.405	162	126	2.759	79	68
GNP	1MH1	0.576	174	144	3.191	81	72
GNP	3SU8	0.633	176	152	3.449	91	79
GNP	3RYT	0.652	173	154	3.488	91	80
GNP	3SUA	0.607	176	148	3.505	91	79
GNP	3SBD	0.416	172	134	3.531	91	82
GNP	3TH5	0.373	168	134	3.960	91	87
GNP	4GZL	0.449	168	132	4.359	82	82
GTP	2WKP	0.428	168	143	3.317	91	78
GTP	1E96	0.435	176	136	3.408	91	79
GTP	5HZH	0.463	130	113	3.515	78	71
GTP	2WKQ	0.434	168	138	3.522	87	77
GTP	3SBD	0.416	172	134	3.531	91	82
GTP	2WKR	0.438	175	143	3.703	91	82
GTP	1G4U	0.602	172	146	3.770	91	84
GTP	1HE1	0.486	172	142	3.912	91	86
GTP	4GZM	0.492	174	139	4.116	91	89
GTP	4GZL	0.449	168	132	4.359	82	82
GCP	2QME	0.517	175	138	3.802	87	80
GCP	2OV2	0.466	172	129	4.316	91	91
APO	2NZ8	0.397	168	122	1.625	91	78
APO	1FOE	0.483	169	131	1.651	91	79
APO	2VRW	0.443	169	133	1.691	91	78
APO	5FI0	0.489	169	141	1.694	91	79
APO	4YON	0.388	167	125	1.765	91	82
APO	3BJI	0.682	168	138	1.871	85	80
APO	2YIN	0.547	161	139	3.476	91	73
APO	3B13	0.472	161	137	3.645	91	75

Supplementary information References

1. Luong P, *et al.* (2010) Kinetic and structural insights into the mechanism of AMPylation by VopS Fic domain. *J Biol Chem* 285(26):20155-20163.
2. Mattoo S, *et al.* (2011) Comparative analysis of *Histophilus somni* immunoglobulin-binding protein A (IbpA) with other fic domain-containing enzymes reveals differences in substrate and nucleotide specificities. *J Biol Chem* 286(37):32834-32842.

3.2 Research article II (in revision for Structure)

Full-length structure of the host targeted bacterial effector Bep1 reveals a novel structural domain conserved in FIC effector proteins from *Bartonella*

Markus Huber, Alexander Wagner, Jens Reiners, Carsten Eric Maximilian Seyfert, Timothy Sharpe, Sander Smits, Tilman Schirmer, and Christoph Dehio

In revision for Structure

Statement of the own participation

I contributed to this publication by Crystallizing the full length protein Bep1 from *B. clarridgeiae*, processing and analysing the data. Alexander Wagner did biophysical assays with Bep1 and VirD4, with support from Timothy Sharpe. Carsten Seyfert did AMPylation assays with Bep1 and its targets. Jens Reiners and Sander Smits performed the SAX experiments. The manuscript was written by me with contributions from Alexander Wagner.

1 **Full-length structure of the host targeted bacterial effector Bep1 reveals a novel**
2 **structural domain conserved in FIC effector proteins from *Bartonella***

3

4

5 Markus Huber^{1,5}, Alexander Wagner^{1,5}, Jens Reiners³, Carsten Eric Maximilian Sey-
6 fert^{1,4}, Timothy Sharpe¹, Sander H.J. Smits^{2,3}, Tilman Schirmer¹, and Christoph
7 Dehio^{1,6*}

8

9 ¹Biozentrum, University of Basel, 4056 Basel, Switzerland

10 ²Biochemie I, Heinrich Heine University Düsseldorf, 40225 Düsseldorf, Germany

11 ³Center for Structural Studies, Heinrich Heine University Düsseldorf, 40225 Düssel-
12 dorf, Germany

13 ⁴current address: Department Microbial Natural Products (MINS), Helmholtz-Institute
14 for Pharmaceutical Research Saarland (HIPS), 66123 Saarbrücken, Germany

15 ⁵Authors contributed equally

16 ⁶Lead Contact

17

18 *Correspondence: christoph.dehio@unibas.ch

19

1 **SUMMARY**

2 Bacterial effector proteins translocated via a type-IV secretion system (T4SS) typically
3 harbor a C-terminal segment required for recognition by the type-IV secretion coupling
4 protein ¹. In the α -proteobacterial pathogen *Bartonella*, the signal is bipartite being
5 composed of a BID (Bep intracellular delivery) domain and a positively charged C-
6 terminal tail ². Here, we show the crystal structure of full length *Bartonella* effector pro-
7 tein 1 (Bep1), which shows a FIC - OB - BAS(BID) domain arrangement conserved in
8 the majority of Beps with the BID domain inserted into the newly discovered BAS par-
9 ent domain. We propose that the BAS domain is necessary for the overall “boomer-
10 ang”-like shape of Bep1 and that it plays a role during translocation through the T4SS.
11

1 INTRODUCTION

2 The α -proteobacterial genus *Bartonella* comprises arthropod-borne facultative, intra-
3 cellular pathogens that are adapted to mammals and frequently cause disease (e.g.
4 cat scratch disease, bacillary angiomatosis or peliosis) in humans ³. A vast majority
5 of *Bartonella* spp. utilize a VirB/VirD4 Type-IV secretion system (T4SS) to translocate
6 an arsenal of Bartonella effector proteins (Beps) into mammalian host cells. Multiple
7 Beps have been characterized and known functions include the inhibition of host cell
8 apoptosis by BepA ⁴, triggering of F-actin driven cytoskeletal processes by BepC ⁵ and
9 the selective targeting of Rac GTPases by Bep1 ⁶.

10 Beps are multi-domain proteins which share a common architecture at their C-termi-
11 nus, consisting of a ~120 amino acid long four-helix bundle, termed Bep intracellular
12 delivery (BID) domain, and a positively charged tail of variable length ^{2, 7}. The two ele-
13 ments constitute a bipartite C-terminal secretion signal that mediates translocation via
14 the VirB/VirD4 T4SS and is evolutionary conserved not only in the Beps of *Bartonella*,
15 but also in the conjugal DNA-transfer-related relaxases and in toxins encoded by many
16 α -proteobacterial species ^{2, 8, 9}.

17 The N-terminal part of Beps is more divergent and can be composed of additional BID
18 domains with secondarily evolved effector functions ^{10, 11}, or tyrosine phosphorylation
19 motifs that act as scaffolds to recruit host cell signaling proteins ¹². However, more than
20 70% of all Beps possess an N-terminal FIC (Filamentation induced by cAMP) domain
21 and an OB (oligonucleotide binding) fold (FIC-OB Beps) preceding the BID domain ¹³.
22 ¹⁴. Most FIC domains mediate posttranslational modifications such as AMPylation and
23 are folded to a core composed of six α -helices ¹⁵⁻¹⁷.

24 *Bartonella* utilize the VirB/VirD4 T4SS ¹⁸ for the translocation of Beps into eukaryotic
25 host cells ^{2, 19, 20}. The T4SS between different organisms are structurally related and
26 are minimally composed of 12 subunits termed VirB2-11 and VirD4 (referring to the

1 nomenclature of the paradigmatic *Agrobacterium tumefaciens* VirB/VirD4 T4SS) ²¹.
2 While VirB2-11 are crucial for the assembly of the VirB/VirD4 T4SS, the type-IV secre-
3 tion coupling protein (T4CP) VirD4 binds substrates prior to their translocation ²². It has
4 also been shown, that binding of substrates to the T4CP can require additional acces-
5 sory proteins, e.g., in *L. pneumophila*. Recent structural advances have yielded new
6 insights into T4SS assembly and architecture by visualizing isolated and intact secre-
7 tion machineries in the bacterial cell envelope ²³⁻²⁸. In Gram-negative bacteria, T4SS
8 consist of a large outer membrane core complex (OMCC) that is connected via a stalk
9 to an inner membrane complex (IMC) ^{23, 28-30}. T4SS can further possess a pilus struc-
10 ture that extends from the cell surface. Diameters of the OMCC are known from the
11 prototypical pKM101-encoded T4SS, which forms an inner cylinder of about 5.5 nm
12 that is open on the cytoplasmic side (Figure 1A). The extracellular opening of the
13 OMCC has a diameter of ~ 2 nm and narrows further inwards to about 1 nm ³⁰. Dimen-
14 sions of other T4SS have been reported for the *Escherichia coli* F-plasmid encoded
15 T4SS, that forms a pilus with an inner diameter of around 2.5 nm, a stalk of 1.9 - 3.5
16 nm and an IMC chamber of around 6 nm ²⁶. The translocation route through the T4SS
17 is narrow to an extent that proteinaceous substrates require at least partial unfolding
18 for efficient translocation, as has been shown for the 107-kDa relaxase TrwC, which is
19 covalently attached to plasmid DNA during conjugation of plasmid R388 ³¹. How sub-
20 strates are unfolded is yet unknown.

21 Recently, we identified the T4SS effector Bep1 from *Bartonella rochalimae* to selec-
22 tively target and AMPylate Rac GTPases via its FIC domain ⁶. Bep1 and its many
23 homologues present in pathogenic *Bartonella* spp. were believed to have a canonical
24 FIC-OB-BID architecture. In this study, we describe the full-length structure of Bep1
25 from *Bartonella clarridgeiae* as the first complete structure of a Bep-T4SS-effector. In
26 the C-terminal part, that had previously been described as unstructured region, the

1 Bep1 structure revealed a domain with a novel fold into which the BID domain is in-
2 serted. Sequence analyses showed that the domain is confined to FIC domain-con-
3 taining Beps and to α -proteobacterial toxins associated with T4SSs. Due to its appar-
4 ent function as a scaffold, we termed the new domain BAS (BID Associated Scaffold
5 domain). In addition, we show that Bep1 undergoes temperature-dependent confor-
6 mational changes, and partially unfolds under physiological temperatures, which might
7 be a prerequisite for effective translocation.

8

9 RESULTS

10 Bep1 is monomeric, active and adopts a boomerang-like shape

11 To gain mechanistic and structural insights into Bep1, we purified full-length Bep1 (558
12 amino acids, tMw: 63 kDa) from *Bartonella clarridgeiae* to homogeneity (inlet Figure
13 1B). In size-exclusion chromatography coupled with multi-angle light-scattering (SEC-
14 MALS) experiments, Bep1 eluted as a monomer (Figure 1B, Table S2). In addition, we
15 observed a small shoulder in the elution profile corresponding to a species with the
16 approximate molecular mass of monomeric Bep1_{FIC-OB} (Bep1₁₋₃₀₉), suggesting proteo-
17 lytic processing as had been observed for BepA before ¹⁵ (Figure S1A). *In vitro*, full-
18 length Bep1 AMPylates small GTPase Rac1 (Figure S1B), with an efficiency compa-
19 rable to that of the Bep1_{FIC-OB} fragment ⁶.

20 Bep1 crystallized in space-group P3₂21 and the structure was solved to a resolution of
21 3 Å by molecular replacement followed by alternating cycles of model building and
22 refinement to a final R_{work} = 27% and R_{free} = 30% (see STAR Methods and Table S1 for
23 details). Continuous electron density defines the main-chain from residues 16 to 558,
24 with the exception of residues 470 to 481. The structure adopts an L- or boomerang-
25 shape formed by two wings of roughly 10 nm in length that form an angle of approxi-
26 mately 100° (Figure 1A). The multi-domain structure is composed of FIC, OB and BID

4

1 folds, with the latter domain found inserted into the BAS domain, which exhibits a novel
2 fold.

3 The FIC domain and the OB-fold are virtually identical to the respective domains of
4 Bep1_{FIC-OB} (PDB 4NPS), with a root-mean-square deviation (RMSD) of 0.56 Å for 241
5 Cα atoms (Figure S1C). Thus, the fold of the FIC domain and the OB-fold are not
6 altered by the presence of the BAS and BID domains and the remaining part of the
7 peptide chain. The BID domain of Bep1 is highly similar to three previously solved
8 isolated BID domain structures⁷. Superposition of Bep1_{BID} (Bep1₃₂₈₋₄₄₇) with the cor-
9 responding residues of *BroBep6*_{BID1} (PDB 4YK1), for instance, yielded an RMSD of
10 1.40 Å for 87 Cα atoms, although the sequence identity is very low with 21% (Figure
11 S1D).

12

13 **The BAS domain: compact and highly conserved**

14 The BAS domain of Bep1 consists of five anti-parallel α-helices and a two-stranded
15 antiparallel β-sheet. The domain extends from residues 320 to 543, but with residues
16 324 to 449 belonging to the BID domain, which is found inserted between the two β-
17 strands (Figure 2A). A compact hydrophobic core (Figure 2B) is formed by helices α2
18 to α5 and the β-sheet. There are no homologous full-length structures of Bep1 known
19 to date and we found no significant structural homologs of the BAS domain in the Pro-
20 tein Data Bank as screened by DALI (Holm 2020) and no significant sequence homo-
21 logs as scanned by ScanProsite (de Castro, Sigrist et al. 2006).

22 Based on sequence comparison, the BAS domain appears to be well conserved
23 among FIC-OB Beps and α-proteobacterial toxins that are associated with the
24 VirB/VirD4 T4SS (Figure 2C). The secondary structure of BAS agrees well with a re-
25 spective prediction using PSIPRED (<http://bioinf.cs.ucl.ac.uk/psipred/>) (Jones 1999,

1 Buchan and Jones 2019) and the unresolved stretch between $\alpha 1$ and $\alpha 2$ (residues 470
2 to 481) is predicted to form an additional helix.

3

4 **BID as a BAS insertion domain**

5 While the core of BID domain structures is highly conserved ⁷ (Figure 3), their termini
6 show significant variations, that can be attributed to the presence of the BAS domains
7 β -sheet. This β -sheet is necessary for the tethering of the N-terminal linker (324-330)
8 to the C-terminal helix ($\alpha 6$) of the BID domain.

9 Moreover, Bep1 homologs that either lack the BAS domain or have lost extensive C-
10 terminal parts also show a lack or degradation of the usually highly conserved
11 L₃₂₀(I/V)P₃₂₂-motif, that is part of the crucial β -sheet, respectively (Figure S3).

12 In addition to our full-length Bep1 structure, that shows the insertion of the structural
13 child domain, BID (324 to 449), into a loop of the BAS domain connecting $\beta 1$ and $\beta 2$,
14 the sequence alignment suggests the insertion as seen in Bep1 also for other Beps
15 and α -proteobacterial toxins.

16

17 **Shape determining interactions of Bep1**

18 To understand the boomerang-like shape conformation of Bep1, we performed a de-
19 tailed analysis of contact areas between the different domains (Figures 4 and S4) and
20 combined this analysis with multiple sequence alignments of Beps and α -proteobacte-
21 rial toxins that are associated with the VirB/VirD4 T4SS (Figures 2C and S2).

22 We calculated buried surface areas between contacting domains by subtracting the
23 solvent accessible surface area of the domain pair from the sum of the respective ar-
24 eas of the isolated domains. We estimated buried surface areas of 1299 Å² for
25 OB:BAS, 648 Å² for BAS:BID, and 271 Å² for OB:BID interfaces.

1 Relevant polar interactions are shown in Figures 4A-D and include capping of helices
2 $\alpha 4$ and $\alpha 5$ of the BAS domain by the OB residues Lys298^{OB} (Figure 4A) and Asp274^{OB}
3 (Figure 4B), respectively. Glu324^{BID} plays a central role by forming interactions with the
4 two neighboring domains: Lys298^{OB} (Figure 4C) and Arg498^{BAS} (Figure 4D). Another
5 interaction between Arg447^{BID} and Glu503^{BAS} contributes to the BAS:BID interface
6 (Figures 4D). Taken together, the multiple inter-domain interactions suggest that the
7 BAS domain is responsible for the relative arrangement of the OB and BID domains
8 and, thus, for the overall “boomerang” shape of Bep1.

9

10 **Bep1 shows increased flexibility and undergoes conformational changes at**
11 **physiological temperatures**

12 To gain further mechanistic and structural insights into T4SS-effectors, like Bep1, we
13 performed small angle X-ray scattering (SAXS), to identify conformational changes
14 and/or partially unfolding under increasing but still physiological temperatures. SAXS
15 is becoming a common technique to analyze conformational changes upon substrate
16 binding or due to changes in the environment, as well as concentration dependent
17 oligomerization ³²⁻³⁴.

18 We initially performed the SAXS experiment at 15°C, on the Xenocs Xeuss 2.0 with Q-
19 Xoom system. The corresponding SAXS data revealing an R_g and D_{max} value of 3.95
20 nm and 13.43 nm, respectively (Figure S5A, Figure S5C and Table S2). The calculated
21 GASBOR fit showed a χ^2 value of 1.14, indicating a good agreement with the experi-
22 mental data (Figure S5A and Table S2). Superimposition of the Bep1 structure and the
23 calculated GASBOR model was done with SUPCOMB and showed a well-fitting over-
24 lay of the Bep1 domains FIC (orange), OB (red), BID (blue) and BAS (green) with the
25 SAXS model (Figure 5A). Comparing the theoretical scattering curve of the Bep1 struc-
26 ture via CRY SOL offers a χ^2 value of 1.38 for the 15°C sample, indicating a very good

7

3 Results

1 agreement of the structure with the measured scattering data (Figure S5E and Table
2 S2).

3 To determine conformational changes under elevated temperatures, we heated the
4 sample up elevating the temperature to 35°C to analyze the effects on the Bep1 sam-
5 ple. To avoid prolonged exposure times at high temperature we performed these tem-
6 perature experiments for Bep1 on the P12 beamline (PETRA III, DESY Hamburg ³⁵).

7 The collected SAXS data were analyzed for changes in the particle size (Figure S5B,
8 Figure S5C, Figure S5D and Table S2). By comparison of the analyzed data, we could
9 clearly see that the R_g (3.95 to 4.43 nm) as well as the D_{max} value (13.43 to 14.42 nm)
10 changes with the temperature rising from 15°C to 35°C. Furthermore, the dimension-
11 less Kratky plot revealed a slightly higher flexibility indicated by the higher sR_g values
12 for the 35°C sample (Figure S5D), but not a complete unfolding of the Bep1 protein.

13 This is in-line with the changes in the particle size, indicating an elongation of the pro-
14 tein (Table S2). We calculated GASBOR models from the different temperatures and
15 compared them to the 15°C model and the crystal structure. The overlay of the 15°C
16 and 35°C GASBOR model, shown in Figure 5B in grey and red mesh representation,
17 visualizes the elongation of the Bep1 protein at higher temperature. Going even higher
18 than 35°C, leads to a rapid aggregation of the protein. Comparing the theoretical scat-
19 tering curve of the Bep1 structure via CRY SOL offers a χ^2 value of 2.20 for the 35°C
20 sample. (Figure S5E and Table S2). The corresponding residual plot shows that the
21 higher χ^2 value mainly comes from the mismatch of the low s region. This indicates a
22 rearrangement of the domains, in-line, with the higher D_{max} values (Figure S5E and
23 Table S2). Taken together this corresponds with the theory that Bep1 stretches und
24 elevated temperatures. With SREFLEX we tried an initial normal mode analysis to re-
25 fine the Bep1 structure for a better agreement with the scattering data at 35°C and fine
26 tune it manually later on (Figure 5D, Figure S5G and Table S2). The refinement offers

3.2 *Research article II (in revision for Structure)*

1 a small twist of the cAMP domain (FIC, orange), the oligonucleotide binding fold (OB,
2 red), the discontinuous BID associated domain (BAS, lime green) and a more stretched
3 Bep intracellular delivery fold BID domain (blue). We measured the angle and the di-
4 mensions of the Bep1 structure and the SAXS models (Figure 5C, TableS3), revealing
5 that the angle changes with higher temperature, suggesting that some of the interac-
6 tions between OB-fold, BID domain and BAS domain (Figure 4) get lost.

1 **DISCUSSION**

2 Bacteria have evolved a plethora of secretion systems that are critical during patho-
3 genesis or interbacterial killing. These systems secrete different substrates including
4 DNA, peptidoglycan and proteins. Proteins are translocated in a folded conformation
5 by T2SSs ³⁶ or at least partially unfolded by e.g. T1SSs ³⁷, T3SSs ³⁸ and T4SSs ³¹. In
6 this study we report the first structure of a full-length Bep-T4SS-effector, Bep1, show-
7 ing a boomerang-like shape, with each wing being around 10 nm in length (Figure 1C).
8 Although the *Bartonella* VirB/VirD4 T4SS machinery has not been microscopically vis-
9 ualized, its translocation channel is probably in the range of around 2 nm to 6 nm in
10 diameter analog to the T4SS machinery encoded by plasmid pKM101 that is structur-
11 ally well characterized (Figure 1A; ²⁶). Considering these shapes and diameters, we
12 hypothesize that secretion of Bep1 and homologs by the T4SS requires partial unfold-
13 ing or at least conformational changes prior or during translocation.

14 The factor(s) that contribute to T4SS-substrate unfolding are not known. In T3SS, a
15 dedicated hexameric ATPase recognizes and unfolds substrates in an ATP-dependent
16 manner ³⁹. T4-secretion is energized by three ATPases: VirB4, VirB11 and the T4CP
17 VirD4. These three ATPases fulfill diverse functions during translocation, including
18 T4SS-pilus assembly, substrate-secretion (VirB4, VirB11) and -recognition (T4CP) ¹⁸.
19 Either of these ATPases could function as an unfoldase for T4SS-substrates and in-
20 duce the required conformational changes in Bep1. The boomerang shape of Bep1 is
21 held together by hydrophobic interactions and a complex network of conserved ionic
22 bonds. However, interdomain interactions are most numerous between BAS and its
23 inserted BID domain, and between BAS and the OB-fold (Figures 2B and 4), suggest-
24 ing a scaffolding role for the BAS domain. Binding of Bep1 to either of the aforemen-
25 tioned ATPases and/or other T4SS components might introduce slight rearrangements

1 that could ultimately promote extensive conformational changes or partial unfolding
2 along the scaffold between the BID domain and the OB-fold.
3 This is supported by the intrinsic flexibility of the effector, that translates through the
4 “knee” shaped by the BAS domain. In our SAXS-experiments we observed that with
5 increasing temperature the angle between the wings of the Bep1 boomerang became
6 wider (Figure 5C, TableS3), indicating that interactions of the OB-fold and BID domain
7 with the BAS domain are less stable at physiological temperatures of *Bartonella* host
8 organisms. Overall, Bep1 adopts a more stretched conformation at 35°C compared to
9 20°C (Figure 5 B/C). As 35°C is closer to the mammalian body temperature, the
10 stretched Bep1 conformation could biologically be more relevant with respect to T4-
11 secretion through the bacterial membrane. Our SAXS data furthermore show that Bep1
12 is partially unfolded at 35°C without the action of an external factor, which might pro-
13 vide evidence of the involvement of intrinsic characteristics of T4SS-effectors in T4-
14 secretion (Figure S5C). External factors, for example the binding of parts of the T4SS
15 to exposed parts of the BAS domain might contribute further to the elongation of Bep1.
16 *In vitro* translocation experiments comparing Bep1 secretion with more stable Bep1
17 derivatives in combination with SAXS measurements could proof the role of the BAS
18 domain in T4-secretion.
19 The C-terminal part of Bep1 following the BID domain had previously been described
20 as unstructured region with a positively charged tail required for efficient translocation
21 ^{2, 8}. Here we have shown that the major part of this tail together with the short segment
22 housing the L₃₂₀(I/V)P₃₂₂-motif, which precedes the BID domain, forms the well-struc-
23 tured BAS domain. Thereby, the short segment forms one of the β -strands of the β -
24 sheet complementing the hydrophobic core of the BAS domain.

3 Results

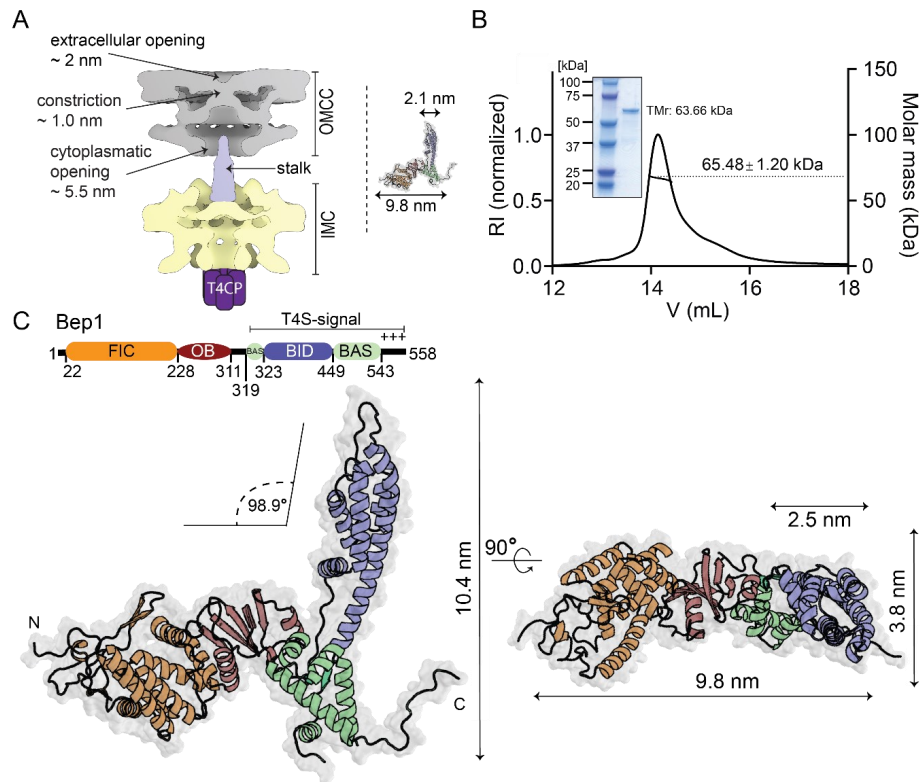
1 Insertions of a child domain into a parent domain have first been identified in the early
2 90s ⁴⁰ and have since been found in 9% of multi-domain proteins of the non-redundant
3 Protein Data Bank ⁴¹.

4 We speculate that during evolution the BID child domain has been inserted into a loop
5 between $\beta 1$ and $\beta 2$ of the BAS parent domain. The conservation of the L₃₂₀(I/V)P₃₂₂-
6 motif in sequences containing the BAS domain, but not in BID domains without a BAS
7 domain (e.g Bep9 and BepE, Figures 3 and S3) is a strong indication for this insertion
8 event.

9 While the BAS domain might play a role for secretion or as part of the bipartite secretion
10 signal ², the occurrence of non-terminal BID:BAS domain combinations (eg. Bep197
11 BID1) suggests a function besides that. It is conceivable, that phenotypes attributed to
12 the BID domain could be triggered in association with the BAS domain, as most BID
13 domain constructs used in previous studies also contained a BAS domain ^{10, 42, 43}.
14 Moreover, the role of the BAS domain might be linked to an enzymatic function that
15 has yet to be explored. Future structure-function studies might unravel the role of the
16 BAS domain after translocation into host cells through the T4SS.

17

1 **Figures**



2

3

4 **Figure 1: Crystal structure of full-length Bep1 and ultrastructure of the T4SS**

5 (A) Scheme of the pKM101-encoded T4SS-machinery with a cutaway view show-
6 ing inner dimensions of the OMCC translocation route. Scheme based on EMD-
7 24098 and EMD-24100 ²⁸, dimensions from Rivera-Calzada et. al. ³⁰. OMCC: outer
8 membrane core complex; IMC: inner membrane complex; T4CP: T4S –coupling pro-
9 tein. Bep1 scaled to the T4SS is depicted on the right.

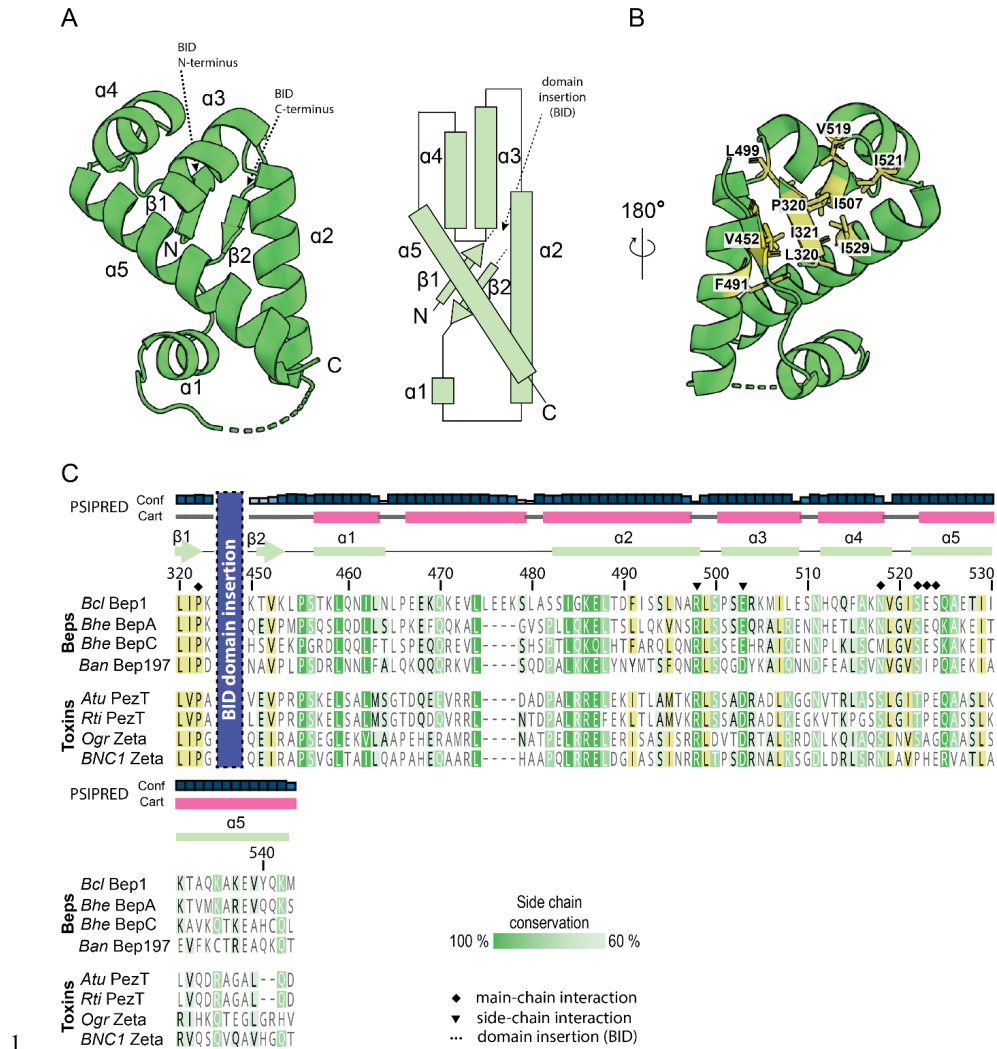
10 (B) Size-exclusion chromatography coupled multi-angle light scattering (SEC-
11 MALS) profile of Bep1 using a GE Healthcare10/300 Superdex 200 increase column.

3 Results

1 Bep1 elutes with an apparent molecular mass of 65 kDa. The inlet depicts the Coo-
2 massie stained SDS-gel of purified Bep1. RI- refractive index. TMr = theoretical Mo-
3 lecular mass. Dots indicate corresponding molar mass (kDa).

4 (C) Overall structure of Bep1 (7ZBR) composed of a filamentation induced by
5 cAMP domain (FIC, orange), an oligonucleotide binding fold (OB, red) which pre-
6 cedes the Bep intracellular delivery fold (BID, blue) and the discontinuous BID asso-
7 ciated domain (BAS, lime green).

8



1 **Figure 2: Structure and sequence conservation of the BAS domain**

2 (A) Structure (left) and topology (right) of the BID associated (BAS) domain

3 formed by 5 α -helices and a 2-stranded antiparallel β -sheet. In the full-length protein,

4 the BID domain is found inserted between β 1 and β 2 as indicated. Note, that the

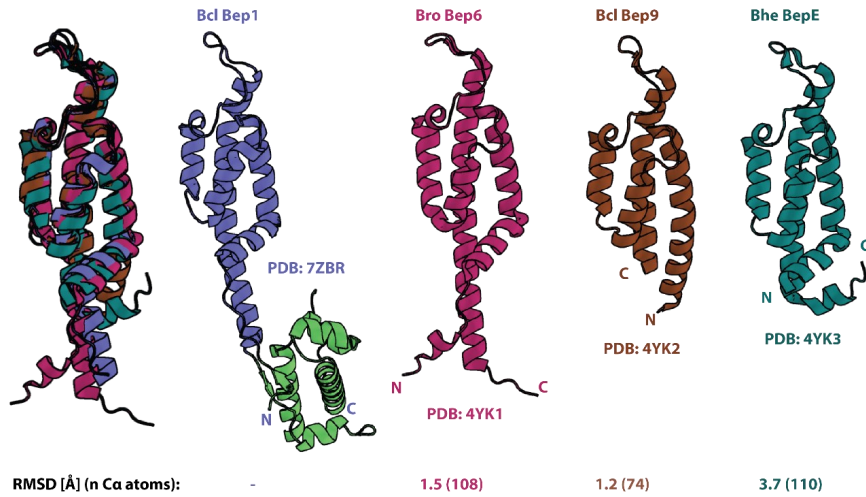
5 stretch between α 1 and α 2 (470-481) is not resolved in our structure.

6 (B) The BAS domain turned by 180° about a vertical axis with respect to the view

7 in panel A, with conserved hydrophobic residues shown as yellow sticks.

3 Results

1 (C) Sequence alignment of the Bep1 BAS domain with other FIC-OB Beps and α -
2 proteobacterial toxins possessing a BID domain. Secondary structure elements of
3 Bep1 BAS are shown on the top (observed in the structure, green; predicted by PSI-
4 PRED ^{44, 45}, pink). Highly conserved residues (100% identity) are shown in white with
5 lime-green background. Conserved residues (>80% identity) are white with a lighter
6 green background. Partially conserved residues (>60% identity) are black with a light
7 green background. Residues involved in intra- and inter-domain interactions (see Fig-
8 ure 4) are highlighted with a black triangle (side-chain) or diamond (main-chain) on
9 top of the alignment. Conserved hydrophobic residues are shown with yellow back-
10 ground.
11



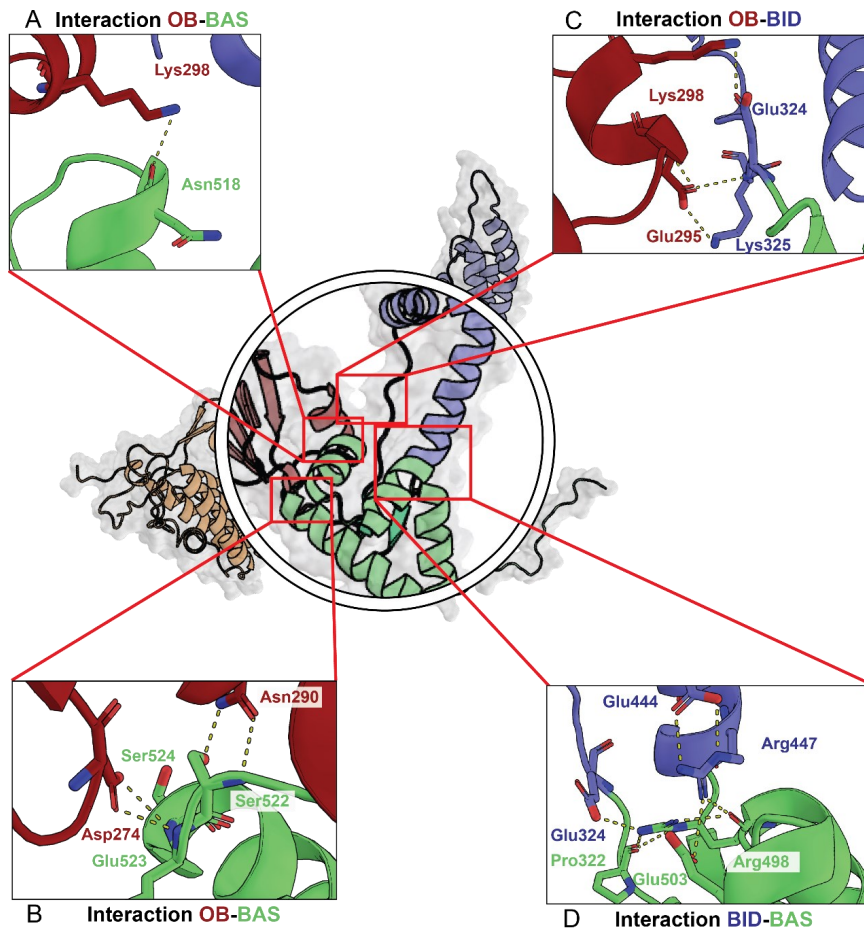
1

2 **Figure 3: Termini of isolated BID domain structures show various arrangement**
 3 **and are tethered together by the BAS domain in full-length Bep1**

4 Superposition (left) and side-by-side view of BID domain structures. For Bep1, also the
 5 BAS domain (green) is shown. The crystal structure of Bep9 from *B. clarridgeiae*
 6 (brown) is of isoform 3 (Bep9/3, see Figure S3). RMSD values refer to the comparison
 7 with Bep1.

8

9



1

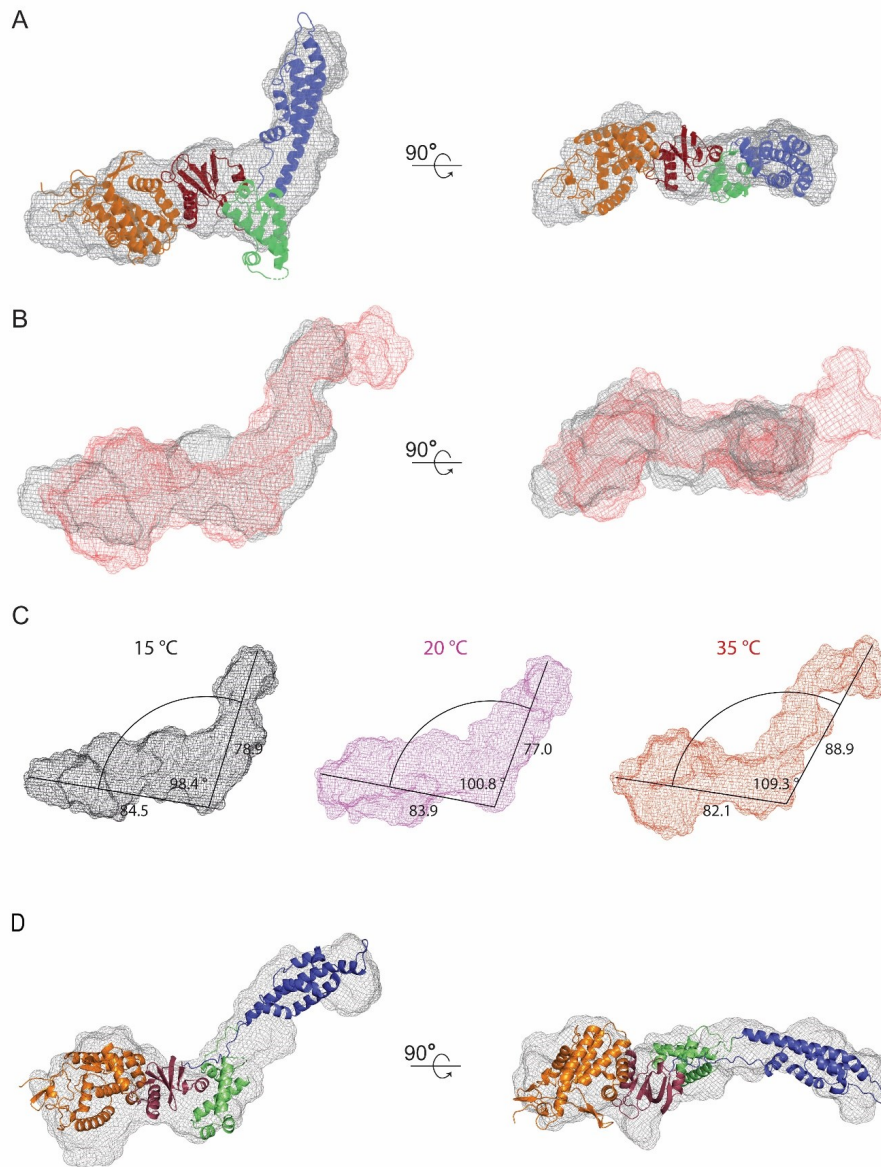
2 **Figure 4: The BAS domain acts as a scaffold for the BID domain and OB-fold**

3 (A-D) Inter-domain interactions of Bep1. Hydrogen bonds and salt-bridges are drawn

4 as yellow dashed lines.

5

1



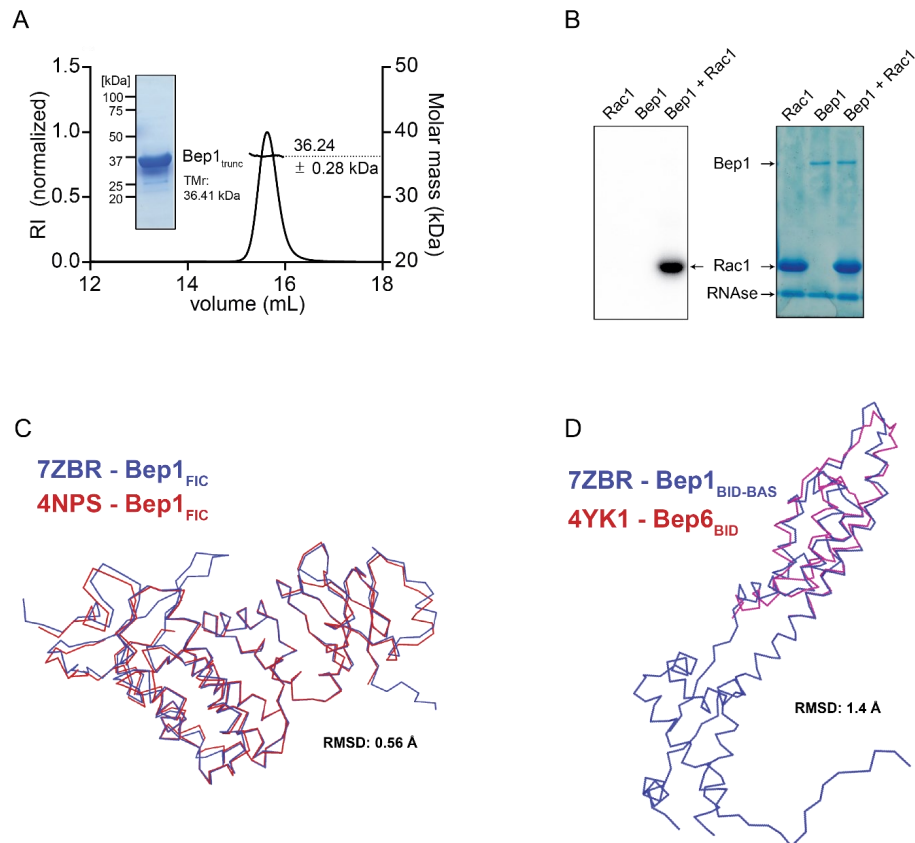
2

3 **Figure 5: Bep1 GASBOR model.** A: The volumetric model from GASBOR is shown
 4 as grey mesh, calculated from the Bep1 at 15 °C scattering data. Superimposing of

3 Results

1 the Bep1 crystal structure was done using SUPCOMB. The Bep1 components FIC
2 domain (orange), OB-fold (red), BID domain (blue) and BAS domain (green) are shown
3 in cartoon representation. **B:** Overlay of the GASBOR model at 15 °C in grey mesh
4 and from 35 °C in red mesh. **C:** GASBOR models of the different temperatures (15 °C
5 in grey, 20 °C in magenta, 35 °C in red) with measured distances and angles. **D:** GAS-
6 BOR models of 35 °C in red and overlaid with the refined Bep1 model.

1 **Supplementary**



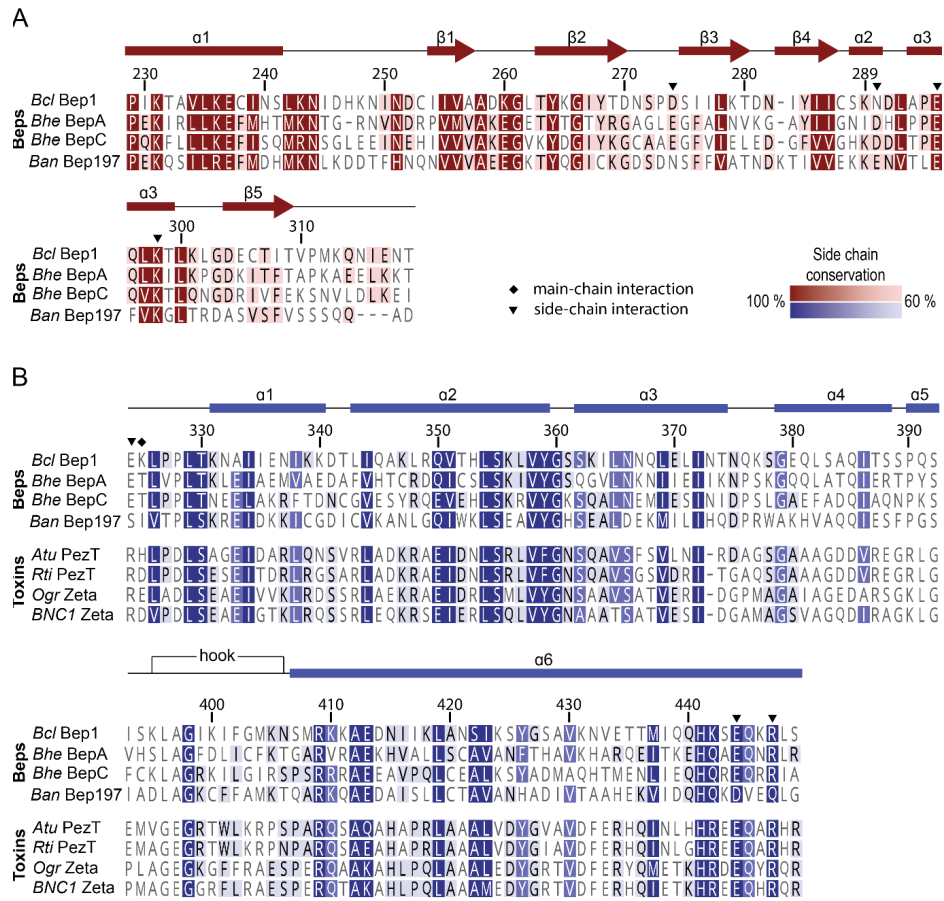
2

3 **Supplementary Figure 1: Characteristics of full-length Bep1**

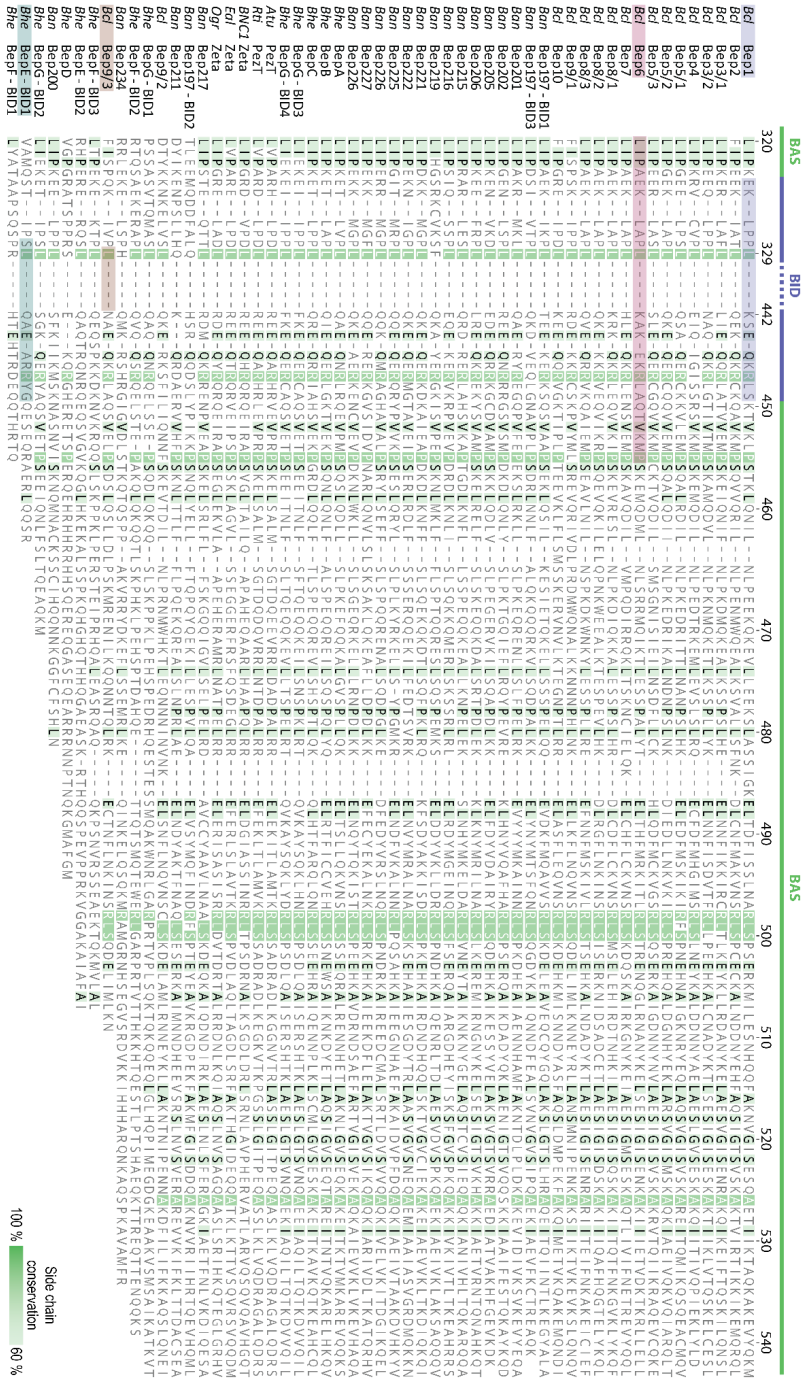
4 (A) Size-exclusion chromatography coupled multi-angle light scattering (SEC-MALS)
 5 profile of Bep1_{trunc} using a GE Healthcare10/300 Superdex 200 increase column.
 6 Bep1_{trunc} elutes with an apparent molecular mass of 36 kDa. The inset depicts the Coo-
 7 massie stained SDS-gel of purified Bep1_{trunc}. RI = refractive index. TMr = theoretical
 8 Molecular mass. Dots indicate corresponding molar mass (kDa).
 9 (B) Autoradiogram and SDS-gel of Bep1 and Rac1 after incubation with ³²P-α-ATP.(C)
 10 Ca-trace of Bep1_{FIC} from full-length *B. clarridgeiae* (blue) overlayed onto Bep1_{FIC}
 11 from *B. rochalimae* (red).

3 Results

- 1 (D) α -trace of Bep1BID-BAS from full-length *B. clarridgeiae* (blue) overlaid onto
- 2 Bep6BID from *B. rochalimae* (red)



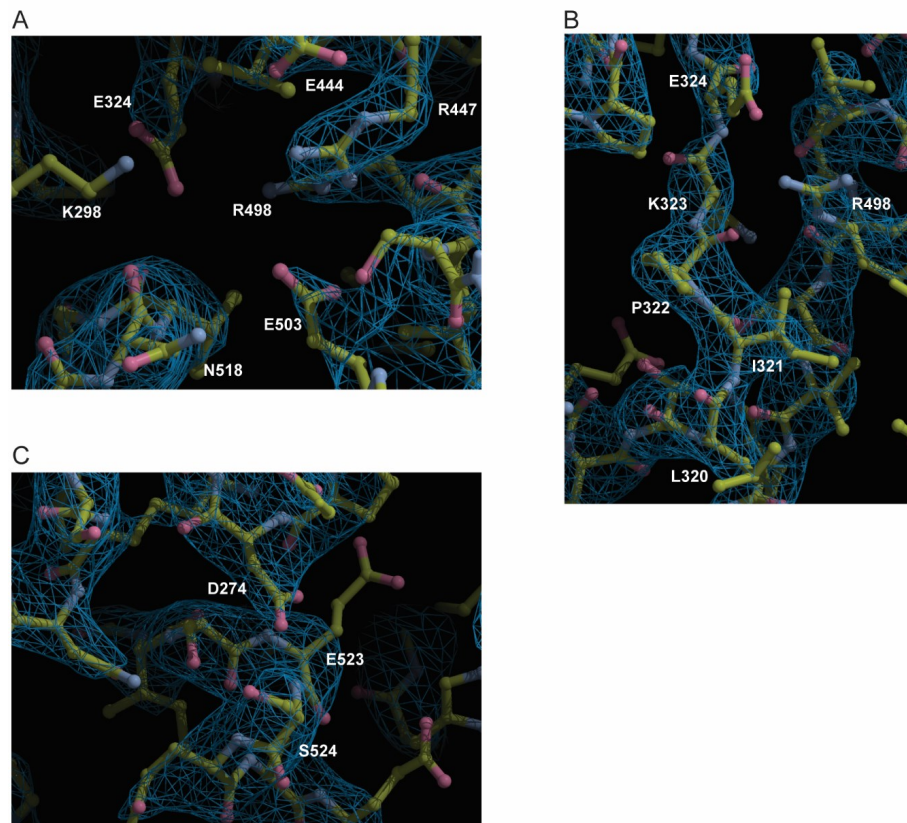
3 Results



1 **Supplementary Figure 3: BAS domain sequence alignment of BID domain pro-**
2 **teins**

3 Multiple-sequence alignment of BID domain containing Beps and α -proteobacterial
4 toxins zoomed in on the BAS domain and the flanking ends of the respective BID do-
5 mains. Sequence coverage of structures seen in Figure 3 is indicated with semi-trans-
6 parent bars of the respective colour. The conservation level (100% - 60%) is shown by
7 the strength of the green background colour.

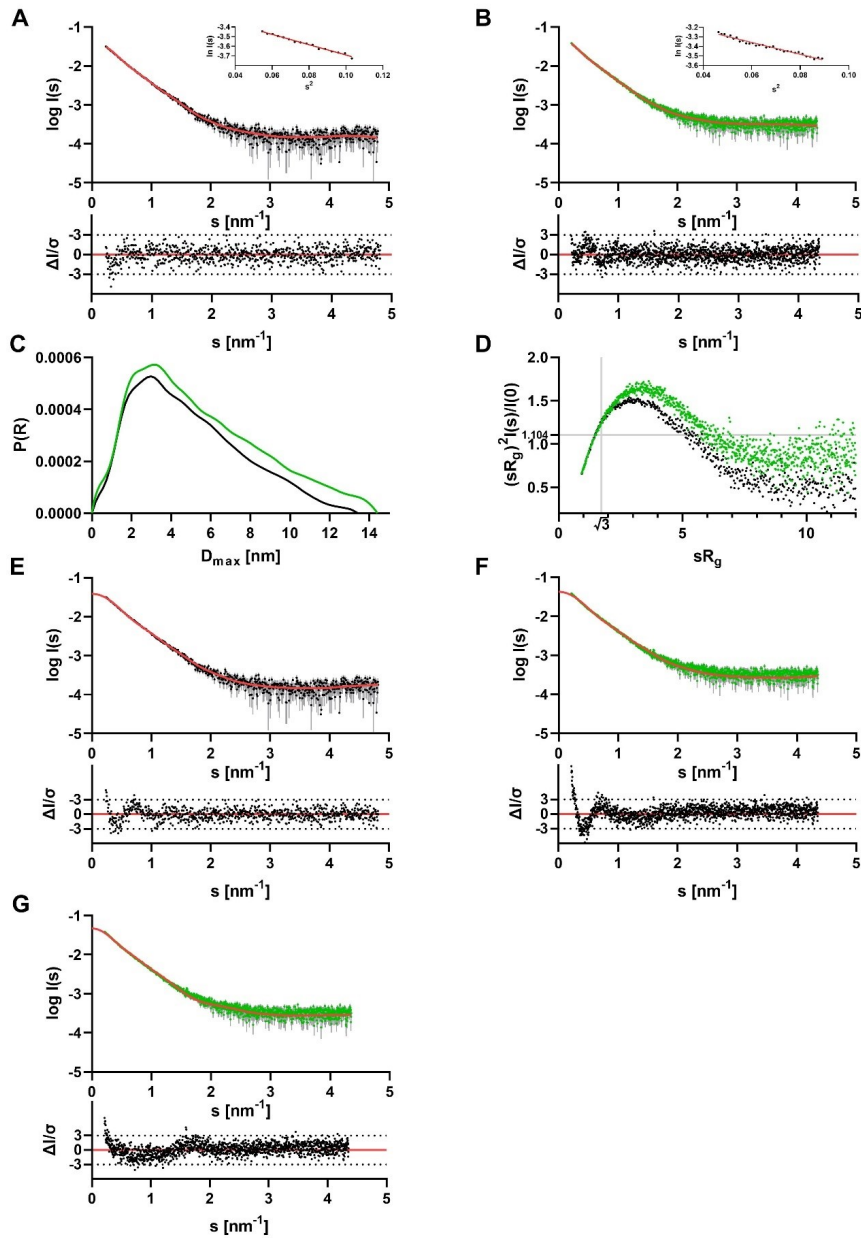
8



1

2 **Supplementary Figure 4: Electron density maps of intra- and interdomain inter-**
3 **actions**

4 A-C show electron density with corresponding model of areas from the OB-fold, BAS
5 domain and BID domain involved in interactions (see Figure 4). Maps are shown as
6 meshes with a contour level of $1.9 \text{ e}/\text{\AA}^3$ in coot ⁴⁶



1

2 **Figure S5: SAXS results for Bep1 at different temperatures. A:** Scattering data of
 3 Bep1 at 15°C. Experimental data are shown in black dots, with grey error bars. The
 4 ab-initio GASBOR model fit is shown as red line and below is the residual plot of the

27

3 Results

1 data. The Guinier plot is added in the right corner. **B**: Scattering data of Bep1 at 35°C.
2 Experimental data are shown in green dots, with grey error bars. The ab-initio GAS-
3 BOR model fit is shown as red line and below is the residual plot of the data. The
4 Guinier plot is added in the right corner. **C**: $\rho(r)$ function of Bep1 at 15°C (black dots)
5 and 35°C (green dots). **D**: Dimensionless Kratky plots of Bep1 at 15°C (black dots)
6 and 35°C (green dots). **E**: CRYSQL fit of the Bep1 crystal structure against the scat-
7 tering data of Bep1 at 15°C. Experimental data are shown in black dots, with grey error
8 bars. The CRYSQL fit is shown as red line and below is the residual plot of the data.
9 **F**: CRYSQL fit of the Bep1 crystal structure against the scattering data of Bep1 at
10 35°C. Experimental data are shown in green dots, with grey error bars. The CRYSQL
11 fit is shown as red line and below is the residual plot of the data. **G**: CRYSQL fit of the
12 refinement of the Bep1 crystal structure against the scattering data of Bep1 at 35°C.
13 Experimental data are shown in green dots, with grey error bars. The CRYSQL fit is
14 shown as red line and below is the residual plot of the data.
15
16

1 **Table S1: Data collection and refinement statistics**

	Bcl. Bep1 (7ZBR)
Resolution range	46.38 - 3.0 (3.107 - 3.0)
Space group	P 32 2 1
Unit cell	70.492 70.492 213.961 90 90 120
Total reflections	166906 (16534)
Unique reflections	13003 (1271)
Multiplicity	12.8 (13.0)
Completeness (%)	99.63 (98.74)
Mean I/sigma(I)	8.10 (0.66)
Wilson B-factor	110.18
R-merge	0.1851 (3.604)
R-meas	0.1933 (3.748)
R-pim	0.05439 (1.014)
CC1/2	0.993 (0.335)
CC*	0.998 (0.709)
Reflections used in refinement	13003 (1255)
Reflections used for R-free	1302 (126)
R-work	0.2699 (0.3957)
R-free	0.3019 (0.4233)
CC(work)	0.924 (0.428)
CC(free)	0.907 (0.238)
Number of non-hydrogen atoms	4196
macromolecules	4196
ligands	0
solvent	0
Protein residues	531
RMS(bonds)	0.003
RMS(angles)	0.62
Ramachandran favored (%)	98.29
Ramachandran allowed (%)	1.71
Ramachandran outliers (%)	0
Rotamer outliers (%)	0
Clashscore	2.35
Average B-factor	102.64
macromolecules	102.64

2

3 Results

1 **Table S2: Overall SAXS Data**

SAXS Device	Xenocs Xeuss 2.0 with Q-Xoom	P12, PETRA III, DESY Hamburg ³⁵	
Data collection parameters			
Detector	PILATUS 3 R 300K windowless	PILATUS 6 M (423.6 x 434.6 mm ²)	
Detector distance (m)	0.550	3.0	
Beam size	0.8 mm x 0.8 mm	120 μm x 200 μm	
Wavelength (nm)	0.154	0.124	
Sample environment	Low Noise Flow Cell, 1 mm ø	Quartz glass capillary, 1 mm ø	
s range (nm ⁻¹) [‡]	0.10 – 6.0	0.02 – 6.0	
Exposure time per frame (s)	600 (30 frames)	0.095 (40 frames)	
Sample			
Organism	<i>Bartonella clarridgeiae</i> CIP		
UniProt ID	E6YFW2 (full length)		
Mode of measurement	batch	batch	
Protein concentration (mg/ml)	12.00	7.80	
Temperature (°C)	15	20	35
Protein buffer	25 mM Hepes pH 7.5, 300 mM NaCl, 1 mM TCEP, 5% glycerol		
Structural parameters			
I(0) from P(r)	0.041	0.046	0.050
R _g (real-space from P(r)) (nm)	3.95	4.00	4.43
s-range for GNOM fit (nm ⁻¹)	0.233 – 4.819	0.232 – 4.355	0.215 – 4.355
I(0) from Guinier fit	0.043	0.046	0.051
s-range for Guinier fit (nm ⁻¹)	0.233 – 0.321	0.232 – 0.337	0.215 – 0.298
R _g (from Guinier fit) (nm)	4.00	3.83	4.32
points from Guinier fit	1 - 16	1 - 39	1 - 31
D _{max} (nm)	13.43	13.42	14.42
POROD volume estimate (nm ³)	82.80	87.43	108.36
Molecular mass (kDa)			
From I(0)	59.55	63.70	70.62
From Qp ⁴⁷	63.71	61.19	67.67
From MoW2 ⁴⁸	56.80	59.44	47.41
From Vc ⁴⁹	56.70	55.71	53.97
Bayesian Inference ⁵⁰	58.15	58.15	63.88
From POROD	51.75	54.64	67.73
From sequence		63.66	
Structure Evaluation			
GASBOR fit χ ²	1.14	1.32	1.09
Ambimeter score	2.484	2.486	2.281
Crysol fit χ ² (s range)	1.377 (0.233 – 4.819)	1.734 (0.232 – 4.355)	2.200 (0.215 – 0.298) 1.60 (after refinement)
Software			
ATSAS Software Version ⁵¹	3.0.2		
Primary data reduction	PRIMUS ⁵²		
Data processing	GNOM ⁵³		
Ab initio modelling	GASBOR ⁵⁴		
Flexible refinement	SREFLEX ⁵⁵		
Superimposing	SUPCOMB ⁵⁵		
Structure evaluation	AMBIMETER ⁵⁶ / CRY SOL ⁵⁷		
Model visualization	PyMOL ⁵⁸		

2 ‡s = 4πsin(θ)/λ, 2θ – scattering angle, λ – X-ray-wavelength, n.d. not determined
3

1 **Table S3: Temperature affected changes on the structure of Bep1**

Temperature (°C)	length (Å)	width (Å)	angle (°)
15	78.9	84.5	98.4
20	77.0	83.9	100.8
35	88.9	82.1	109.3

2

1 **STAR METHODS**

2

3 **RESOURCE AVAILABILITY**

4 **Lead Contact**

5 Further information and requests for resources and reagents should be directed to and
6 will be fulfilled by the Lead Contact, Dr. Christoph Dehio (christoph.dehio@unibas.ch).

7

8 **Material Availability**

9 Plasmids generated in this study are available upon request to the Lead Contact.

10

11 **Data and Code Availability**

12 Structural data are deposited on <https://www.rcsb.org/> and <https://www.sasbdb.org/>.

13

14 **EXPERIMENTAL MODEL AND SUBJECT DETAILS**

15 **Microbes**

16 *E. coli* cells were cultured at 20°C - 37°C in LB medium supplemented with appropriate
17 antibiotics (Key resource table).

18

19 **METHOD DETAILS**

20 **Cloning**

21 A Construct encoding soluble *Bartonella clarridgeiae* (Bcl)-Bep1 (Bep1-Fic-OB)_{aa1-309}
22 was cloned via restriction cloning into pRSFDuet™-1, resulting in pAW041. Note that
23 (Bcl)-Bep1 full length_{aa1-558} was received from the Seattle Structural Genomics Center
24 for Infectious Disease (see Key resource table).

25

1 **Protein Expression and Purification**

2 Expression plasmids (pCES001, pAW041) were transformed into *E. coli* BL21(DE3).
3 Single colonies were picked to inoculate precultures, respectively, which were incu-
4 bated overnight at 37°C in 50 ml LB + 1% glucose + 100 µg/ml ampicillin (BG1861-
5 *His6-bep1_{bcl}*) or 50 µg/ml kanamycin. Next day, 15 ml of precultures were used to in-
6 oculate 1.5 l LB + 1% glucose + the appropriate antibiotic and cultures were grown at
7 37°C to OD=1.0. Protein expression was induced with 0.2-0.5 mM IPTG and expres-
8 sion cultures were incubated at 21°C for 16 hours. Expression cultures were pelleted,
9 frozen in liquid nitrogen and stored at -80°C. Cell pellets were resuspended in low
10 imidazole buffer (25 mM Hepes pH 7.5, 20 mM imidazole, 300 mM NaCl, 1 mM TCEP,
11 5% glycerol) supplemented with Benzonase® (Merck) and cOmplete™ Mini EDTA-free
12 protease inhibitor (Roche). Following incubation for 30 min on ice, cells were broken
13 using a French Press (16 000 psi) and supernatant was obtained by centrifugation at
14 100.000 x g (45 min, 4°C). Subsequently, the supernatant was loaded onto a pre-
15 equilibrated (with low imidazole buffer) HisTrap™excel column (GE Healthcare). Fol-
16 lowing a wash step of the column with 5 column volumes low imidazole buffer, proteins
17 were eluted with an imidazole gradient from 20 to 500 mM imidazole. Elution fractions
18 were concentrated in Amicon® Ultra-15 centrifugal filters (30 kDa cut-off for Bep1 and
19 sVirD4, 10 kDa cut-off for Bep1-Fic-OB). Concentrated proteins were further purified
20 by Size-exclusion chromatography (SEC) either using a HiLoad 16/60 Superdex 200
21 pg column (GE Healthcare) or a HiLoad 16/60 Superdex 75 pg column (GE
22 Healthcare) pre-equilibrated in SEC-buffer (25 mM Hepes pH 7.5, 300 mM NaCl, 1
23 mM TCEP, 5% glycerol). Eluted proteins were frozen in liquid nitrogen and stored at -
24 80°C. Protein concentrations were determined using the Pierce™ BCA Protein Assay
25 kit (Thermo Fisher Scientific) and via direct A280-measurments using a NanoDrop
26 One^C UV-Vis spectrophotometer (Thermo Fisher Scientific).

1

2 **Structure determination**

3 For crystallization 12 mg/ml of the purified Bep1 (0.2 mM, supplemented with 5 mM
4 ATP and 5 mM MgCl₂) were mixed with reservoir solution in a ratio of 1:2 yielding an
5 end concentration of 4 mg/ml. Crystallization was done using the sitting-drop vapour
6 diffusion method by dispensing 0.6 µl in MRC 96-well plates (SWISSCI). The reservoir
7 solution was composed of 100 mM Hepes pH 7.8, 0.175 mM LiCl and 20% v/v PEG
8 8000. Crystals were obtained at 20°C and frozen in liquid nitrogen with glycerol as an
9 additional cryoprotectant. Data collection was done at the Swiss Light Source of the
10 PSI (<https://www.psi.ch/en/sls>) on beam-line X06SA (PXI) at $\lambda = 1.0 \text{ \AA}$ with an EIGER
11 16M X detector (133 Hz). Images were processed with XDS⁵⁹. The structure was
12 solved by molecular replacement with Phaser⁶⁰. As search models the crystal struc-
13 tures of Bep1 (FIC and OB domain, PDB: 4NPS) from *Bartonella clarridgeiae* and Bep6
14 (BID domain, PDB: 4YK1) from *Bartonella rochalimae* were used. Model building was
15 done in COOT⁴⁶ with alternating cycles of refinement in Phenix⁶¹. Data collection and
16 refinement statistics are summarized in Table S1.

17

18 **Small-Angle X-ray Scattering (SAXS)**

19 We collected the initial SAXS data from Bep1 on our Xeuss 2.0 Q-Xoom system from
20 Xenocs, equipped with a PILATUS 3 R 300K detector (Dectris) and a GENIX 3D CU
21 Ultra Low Divergence x-ray beam delivery system. The chosen sample to detector
22 distance for the experiment was 0.55 m, results in an achievable q-range of 0.10 - 6
23 nm⁻¹. The measurement was performed at 15 °C with a protein concentration range of
24 3 - 12 mg/ml. The Bep1 sample was injected in the Low Noise Flow Cell (Xenocs) via
25 autosampler. We collect 30 frames with an exposur time of ten minutes/frame and

1 scaled the data to absolute intensity against water. We checked each frame for radia-
2 tion damage using CorMap/ χ^2 test, implemented in in PRIMUS ⁵². After checking the
3 frames of the different concentrations we saw no concentration effect and continue the
4 evaluation with the 12 mg/ml data set.

5 To avoid longer exposer times on high temperature we performed the temperature
6 experiments for Bep1 on the P12 beamline (PETRA III, DESY Hamburg ³⁵). The au-
7 to-sampler at P12 was set to the chosen temperature and the Bep1 sample (7.8 mg/ml)
8 was incubated 20 min before measuring. We collected 40 frames for each temperature
9 with an exposer time of 0.095 sec/frame, radiation damage was checked via the
10 SASFLOW pipeline⁶³ and identical frames were merged. Data were scaled to absolute
11 intensity against water.

12 All used programs for data processing were part of the ATSAS Software package (Ver-
13 sion 3.0.2) ⁵¹. Primary data reduction was performed with the program PRIMUS ⁵².
14 With the Guinier approximation ⁶², we determine the forward scattering $I(0)$ and the
15 radius of gyration (R_g). The program GNOM ⁵³ was used to estimate the maximum
16 particle dimension (D_{max}) with the pair-distribution function $p(r)$. Cross evaluations of
17 the D_{max} values was also done using SHANUM ⁶⁵. Low resolution *ab initio* models
18 were calculated with GASBOR ⁵⁴. The theoretical scattering of the Bep1 structure was
19 computed with CRY SOL (ns 501, lm 70, fb 18), using the same s-range like GNOM
20 and compared against the solution scattering data of the different used temperature ⁵⁸.
21 We refine the Bep1 crystal structure with SREFLEX ⁵⁵ using the 35 °C scattering data
22 and fine tune the structure manually later on. Superimposing of the Bep1 structure was
23 done with the program SUPCOMB ⁵⁵.

24

25 **Multiangle Light Scattering**

3 Results

1 Size-exclusion chromatography coupled multiangle light scattering (SEC-MALS) of
2 Bep1-derivatives was performed on a GE Healthcare10/300 Superdex 200 increase
3 column, equilibrated overnight with SEC buffer (25 mM Hepes pH 7.5, 300 mM NaCl,
4 1 mM TCEP, 5% glycerol) at 25°C, using an Agilent 1260 HPLC. 100 ul sample at a
5 concentration of 0.3 mg/ml (Bep1) or 0.2 mg/ml (Bep1-Fic-OB) were applied and elu-
6 tion was monitored an Agilent multi-wavelength absorbance detector (280 nm), a Wy-
7 att Heleos II 8+ multiangle light scattering detector and a Wyatt Optilab rEX differential
8 refractive index detector. 2 mg/ml BSA solution (Thermo Pierce) was injected to cali-
9 brate interdetector delay volumes, band broadening corrections, and light scattering
10 detector normalization using the Wyatt ASTRA 6 software (Wyatt Technology). Weight-
11 averaged molar mass was calculated from the light scattering and the differential re-
12 fractive index (RI) signals using Wyatt ASTRA 6 software (Wyatt Technology).

13

14 **QUANTIFICATION AND STATISTICAL ANALYSIS**

15 Statistical parameters are indicated in figures and respective legends. Error bars in the
16 SAXS scattering plots (Figure S5) show the standard deviation. Statistical data of the
17 Bep1 structure data collection and refinement are summarized in Table S1. Statistics
18 of the SAXS Data collection are shown in Table S2.

19

20 **DATA AND SOFTWARE AVAILABILITY**

21 We upload the SAXS data to the Small Angle Scattering Biological Data Bank
22 (SASBDB) (Valentini et al. 2015; Kikhney et al. 2020), with the accession codes
23 SASDLK7 (15°C), SASDLL7 (20°C) and SASDLM7 (35°C).

24 Protein structure data have been deposited in the Protein Data Bank under accession
25 number 7ZBR.

3.2 *Research article II (in revision for Structure)*

1 Molecular replacement was done with Phaser ⁶⁰. Several rounds of iterative model
2 building and refinement were performed using Coot ⁴⁶ and Phenix.refine ⁶¹, respec-
3 tively. MSA were done with the GENEIOUS software package Version 7.1.7 and later
4 ⁶³. Visualization of structures and models were done with pymol ⁶⁴.
5

1 REFERENCES

- 2 [1] Christie, P. J., Whitaker, N., and Gonzalez-Rivera, C. (2014) Mechanism and structure of the
3 bacterial type IV secretion systems, *Biochim Biophys Acta* 1843, 1578-1591.
- 4 [2] Schulein, R., Guye, P., Rhomberg, T. A., Schmid, M. C., Schröder, G., Vergunst, A. C., Carena, I., and
5 Dehio, C. (2005) A bipartite signal mediates the transfer of type IV secretion substrates of
6 *Bartonella henselae* into human cells, *Proceedings of the National Academy of Sciences of the*
7 *United States of America* 102, 856-861.
- 8 [3] Wagner, A., and Dehio, C. (2019) Role of distinct type-IV-secretion systems and secreted effector
9 sets in host adaptation by pathogenic *Bartonella* species, *Cellular microbiology* 21, e13004.
- 10 [4] Pulliainen, A. T., Pielles, K., Brand, C. S., Hauert, B., Böhm, A., Quebatte, M., Wepf, A., Gstaiger, M.,
11 Aebersold, R., Dessauer, C. W., and Dehio, C. (2012) Bacterial effector binds host cell adenyllyl
12 cyclase to potentiate Gas-dependent cAMP production, *Proceedings of the National*
13 *Academy of Sciences of the United States of America* 109, 9581-9586.
- 14 [5] Marlaire, S., and Dehio, C. (2020) *Bartonella* effector protein C mediates actin stress fiber
15 formation via recruitment of GEF-H1 to the plasma membrane, 2020.2004.2017.046482.
- 16 [6] Dietz, N., Huber, M., Sorg, I., Goepfert, A., Harms, A., Schirmer, T., and Dehio, C. (2021) Structural
17 basis for selective AMPylation of Rac-subfamily GTPases by *Bartonella* effector protein 1
18 (Bep1), *Proceedings of the National Academy of Sciences of the United States of America* 118.
- 19 [7] Stanger, F. V., de Beer, T. A. P., Dranow, D. M., Schirmer, T., Phan, I., and Dehio, C. (2017) The BID
20 Domain of Type IV Secretion Substrates Forms a Conserved Four-Helix Bundle Topped with a
21 Hook, *Structure (London, England : 1993)* 25, 203-211.
- 22 [8] Harms, A., Liesch, M., Körner, J., Québatte, M., Engel, P., and Dehio, C. (2017) A bacterial toxin-
23 antitoxin module is the origin of inter-bacterial and inter-kingdom effectors of *Bartonella*,
24 *PLoS genetics* 13, e1007077.
- 25 [9] Wagner, A., Tittes, C., and Dehio, C. (2019) Versatility of the BID Domain: Conserved Function as
26 Type-IV-Secretion-Signal and Secondarily Evolved Effector Functions Within *Bartonella*-
27 Infected Host Cells, *Frontiers in microbiology* 10, 921.
- 28 [10] Truttmann, M. C., Guye, P., and Dehio, C. (2011) BID-F1 and BID-F2 domains of *Bartonella*
29 *henselae* effector protein BepF trigger together with BepC the formation of invasome
30 structures, *PLoS one* 6, e25106.
- 31 [11] Okujava, R., Guye, P., Lu, Y. Y., Mistl, C., Polus, F., Vayssier-Taussat, M., Halin, C., Rolink, A. G.,
32 and Dehio, C. (2014) A translocated effector required for *Bartonella* dissemination from
33 derma to blood safeguards migratory host cells from damage by co-translocated effectors,
34 *PLoS pathogens* 10, e1004187.

3.2 Research article II (in revision for Structure)

- 1 [12] Sorg, I., Schmutz, C., Lu, Y. Y., Fromm, K., Siewert, L. K., Bögli, A., Strack, K., Harms, A., and Dehio,
2 C. (2020) A Bartonella Effector Acts as Signaling Hub for Intrinsic STAT3 Activation to Trigger
3 Anti-inflammatory Responses, *Cell host & microbe* 27, 476-485.e477.
- 4 [13] Engel, P., Salzburger, W., Liesch, M., Chang, C. C., Maruyama, S., Lanz, C., Calteau, A., Lajus, A.,
5 Médigue, C., Schuster, S. C., and Dehio, C. (2011) Parallel evolution of a type IV secretion
6 system in radiating lineages of the host-restricted bacterial pathogen *Bartonella*, *PLoS*
7 *genetics* 7, e1001296.
- 8 [14] Harms, A., Segers, F. H., Quebatte, M., Mistl, C., Manfredi, P., Körner, J., Chomel, B. B., Kosoy,
9 M., Maruyama, S., Engel, P., and Dehio, C. (2017) Evolutionary Dynamics of Pathoadaptation
10 Revealed by Three Independent Acquisitions of the VirB/D4 Type IV Secretion System in
11 *Bartonella*, *Genome biology and evolution* 9, 761-776.
- 12 [15] Palanivelu, D. V., Goepfert, A., Meury, M., Guye, P., Dehio, C., and Schirmer, T. (2011) Fic
13 domain-catalyzed adenylation: insight provided by the structural analysis of the type IV
14 secretion system effector BepA, *Protein Sci* 20, 492-499.
- 15 [16] Roy, C. R., and Cherfils, J. (2015) Structure and function of Fic proteins, *Nature reviews*.
16 *Microbiology* 13, 631-640.
- 17 [17] Harms, A., Stanger, F. V., and Dehio, C. (2016) Biological Diversity and Molecular Plasticity of FIC
18 Domain Proteins, *Annual review of microbiology* 70, 341-360.
- 19 [18] Waksman, G. (2019) From conjugation to T4S systems in Gram-negative bacteria: a mechanistic
20 biology perspective, *EMBO reports* 20.
- 21 [19] Beijersbergen, A., Dulk-Ras, A. D., Schilperoort, R. A., and Hooykaas, P. J. (1992) Conjugative
22 Transfer by the Virulence System of *Agrobacterium tumefaciens*, *Science (New York, N.Y.)*
23 256, 1324-1327.
- 24 [20] Souza, D. P., Oka, G. U., Alvarez-Martinez, C. E., Bisson-Filho, A. W., Dunger, G., Hobeika, L.,
25 Cavalcante, N. S., Alegria, M. C., Barbosa, L. R., Salinas, R. K., Guzzo, C. R., and Farah, C. S.
26 (2015) Bacterial killing via a type IV secretion system, *Nature communications* 6, 6453.
- 27 [21] Li, Y. G., and Christie, P. J. (2018) The *Agrobacterium* VirB/VirD4 T4SS: Mechanism and
28 Architecture Defined Through In Vivo Mutagenesis and Chimeric Systems, *Current topics in*
29 *microbiology and immunology* 418, 233-260.
- 30 [22] Costa, T. R. D., Harb, L., Khara, P., Zeng, L., Hu, B., and Christie, P. J. (2020) Type IV Secretion
31 Systems: Advances in Structure, Function, and Activation, *Molecular microbiology*.
- 32 [23] Low, H. H., Gubellini, F., Rivera-Calzada, A., Braun, N., Connery, S., Dujeancourt, A., Lu, F.,
33 Redzej, A., Fronzes, R., Orlova, E. V., and Waksman, G. (2014) Structure of a type IV secretion
34 system, *Nature* 508, 550-553.

3 Results

- 1 [24] Ghosal, D., Chang, Y. W., Jeong, K. C., Vogel, J. P., and Jensen, G. J. (2017) In situ structure of the
2 *Legionella* Dot/Icm type IV secretion system by electron cryotomography, *EMBO reports* 18,
3 726-732.
- 4 [25] Chetrit, D., Hu, B., Christie, P. J., Roy, C. R., and Liu, J. (2018) A unique cytoplasmic ATPase
5 complex defines the *Legionella pneumophila* type IV secretion channel, *Nature microbiology*
6 3, 678-686.
- 7 [26] Hu, B., Khara, P., and Christie, P. J. (2019) Structural bases for F plasmid conjugation and F pilus
8 biogenesis in *Escherichia coli*, *Proceedings of the National Academy of Sciences of the United*
9 *States of America* 116, 14222-14227.
- 10 [27] Hu, B., Khara, P., Song, L., Lin, A. S., Frick-Cheng, A. E., Harvey, M. L., Cover, T. L., and Christie, P.
11 J. (2019) In Situ Molecular Architecture of the *Helicobacter pylori* Cag Type IV Secretion
12 System, *mBio* 10.
- 13 [28] Khara, P., Song, L., Christie, P. J., and Hu, B. (2021) In Situ Visualization of the pKM101-Encoded
14 Type IV Secretion System Reveals a Highly Symmetric ATPase Energy Center, *mBio* 12,
15 e0246521.
- 16 [29] Fronzes, R., Schäfer, E., Wang, L., Saibil, H. R., Orlova, E. V., and Waksman, G. (2009) Structure of
17 a type IV secretion system core complex, *Science (New York, N.Y.)* 323, 266-268.
- 18 [30] Rivera-Calzada, A., Fronzes, R., Savva, C. G., Chandran, V., Lian, P. W., Laeremans, T., Pardon, E.,
19 Steyaert, J., Remaut, H., Waksman, G., and Orlova, E. V. (2013) Structure of a bacterial type
20 IV secretion core complex at subnanometre resolution, *The EMBO journal* 32, 1195-1204.
- 21 [31] Trokter, M., and Waksman, G. (2018) Translocation through the Conjugative Type IV Secretion
22 System Requires Unfolding of Its Protein Substrate, *Journal of bacteriology* 200.
- 23 [32] Molodenskiy, D., Shirshin, E., Tikhonova, T., Gruzinov, A., Peters, G., and Spinozzi, F. (2017)
24 Thermally induced conformational changes and protein-protein interactions of bovine serum
25 albumin in aqueous solution under different pH and ionic strengths as revealed by SAXS
26 measurements, *Phys Chem Chem Phys* 19, 17143-17155.
- 27 [33] Josts, I., Nitsche, J., Maric, S., Mertens, H. D., Moulin, M., Haertlein, M., Prevost, S., Svergun, D.
28 I., Busch, S., Forsyth, V. T., and Tidow, H. (2018) Conformational States of ABC Transporter
29 MsbA in a Lipid Environment Investigated by Small-Angle Scattering Using Stealth Carrier
30 Nanodiscs, *Structure (London, England : 1993)* 26, 1072-1079 e1074.
- 31 [34] Manalastas-Cantos, K., Kschonsak, M., Haering, C. H., and Svergun, D. I. (2019) Solution structure
32 and flexibility of the condensin HEAT-repeat subunit Ycg1, *J Biol Chem* 294, 13822-13829.
- 33 [35] Blanchet, C. E., Spilotros, A., Schwemmer, F., Graewert, M. A., Kikhney, A., Jeffries, C. M., Franke,
34 D., Mark, D., Zengerle, R., Cipriani, F., Fiedler, S., Roessle, M., and Svergun, D. I. (2015)

3.2 Research article II (in revision for Structure)

- 1 Versatile sample environments and automation for biological solution X-ray scattering
2 experiments at the P12 beamline (PETRA III, DESY), *J Appl Crystallogr* 48, 431-443.
- 3 [36] Nivaskumar, M., and Francetic, O. (2014) Type II secretion system: a magic beanstalk or a
4 protein escalator, *Biochim Biophys Acta* 1843, 1568-1577.
- 5 [37] Bakkes, P. J., Jenewein, S., Smits, S. H., Holland, I. B., and Schmitt, L. (2010) The rate of folding
6 dictates substrate secretion by the Escherichia coli hemolysin type 1 secretion system, *J Biol*
7 *Chem* 285, 40573-40580.
- 8 [38] Stebbins, C. E., and Galan, J. E. (2003) Priming virulence factors for delivery into the host, *Nat*
9 *Rev Mol Cell Biol* 4, 738-743.
- 10 [39] Akeda, Y., and Galan, J. E. (2005) Chaperone release and unfolding of substrates in type III
11 secretion, *Nature* 437, 911-915.
- 12 [40] Russell, R. B. (1994) Domain insertion, *Protein Eng* 7, 1407-1410.
- 13 [41] Aroul-Selvam, R., Hubbard, T., and Sasidharan, R. (2004) Domain insertions in protein structures,
14 *J Mol Biol* 338, 633-641.
- 15 [42] Schmid, M. C., Scheidegger, F., Dehio, M., Balmelle-Devaux, N., Schulein, R., Guye, P.,
16 Chennakesava, C. S., Biedermann, B., and Dehio, C. (2006) A translocated bacterial protein
17 protects vascular endothelial cells from apoptosis, *PLoS pathogens* 2, e115.
- 18 [43] Rhomberg, T. A., Truttmann, M. C., Guye, P., Ellner, Y., and Dehio, C. (2009) A translocated
19 protein of Bartonella henselae interferes with endocytic uptake of individual bacteria and
20 triggers uptake of large bacterial aggregates via the invasome, *Cellular microbiology* 11, 927-
21 945.
- 22 [44] Jones, D. T. (1999) Protein secondary structure prediction based on position-specific scoring
23 matrices, *J Mol Biol* 292, 195-202.
- 24 [45] Buchan, D. W. A., and Jones, D. T. (2019) The PSIPRED Protein Analysis Workbench: 20 years on,
25 *Nucleic Acids Res* 47, W402-W407.
- 26 [46] Emsley, P., Lohkamp, B., Scott, W. G., and Cowtan, K. (2010) Features and development of Coot,
27 *Acta Crystallogr D Biol Crystallogr* 66, 486-501.
- 28 [47] Porod, G. (1951) Die Röntgenkleinwinkelstreuung Von Dichtgepackten Kolloiden Systemen - 1
29 Teil., *Kolloid Z Z Polym* 124, 83-114.
- 30 [48] Fischer, H., Neto, M. D., Napolitano, H. B., Polikarpov, I., and Craievich, A. F. (2010)
31 Determination of the molecular weight of proteins in solution from a single small-angle X-ray
32 scattering measurement on a relative scale, *Journal of Applied Crystallography* 43, 101-109.
- 33 [49] Rambo, R. P., and Tainer, J. A. (2013) Accurate assessment of mass, models and resolution by
34 small-angle scattering, *Nature* 496, 477-481.

3 Results

- 1 [50] Hajizadeh, N. R., Franke, D., Jeffries, C. M., and Svergun, D. I. (2018) Consensus Bayesian
2 assessment of protein molecular mass from solution X-ray scattering data, *Sci Rep* 8, 7204.
- 3 [51] Manalastas-Cantos, K., Konarev, P. V., Hajizadeh, N. R., Kikhney, A. G., Petoukhov, M. V.,
4 Molodenskiy, D. S., Panjkovich, A., Mertens, H. D. T., Gruzinov, A., Borges, C., Jeffries, C. M.,
5 Svergun, D. I., and Franke, D. (2021) ATSAS 3.0: expanded functionality and new tools for
6 small-angle scattering data analysis, *Journal of Applied Crystallography* 54.
- 7 [52] Konarev, P. V., Volkov, V. V., Sokolova, A. V., Koch, M. H. J., and Svergun, D. I. (2003) PRIMUS: a
8 Windows PC-based system for small-angle scattering data analysis, *Journal of Applied*
9 *Crystallography* 36, 1277-1282.
- 10 [53] Svergun, D. I. (1992) Determination of the Regularization Parameter in Indirect-Transform
11 Methods Using Perceptual Criteria, *Journal of Applied Crystallography* 25, 495-503.
- 12 [54] Svergun, D. I., Petoukhov, M. V., and Koch, M. H. (2001) Determination of domain structure of
13 proteins from X-ray solution scattering, *Biophysical journal* 80, 2946-2953.
- 14 [55] Panjkovich, A., and Svergun, D. I. (2016) Deciphering conformational transitions of proteins by
15 small angle X-ray scattering and normal mode analysis, *Phys Chem Chem Phys* 18, 5707-5719.
- 16 [56] Kozin, M. B., and Svergun, D. I. (2001) Automated matching of high- and low-resolution
17 structural models, *Journal of Applied Crystallography* 34, 33-41.
- 18 [57] Petoukhov, M. V., and Svergun, D. I. (2015) Ambiguity assessment of small-angle scattering
19 curves from monodisperse systems, *Acta Crystallogr D Biol Crystallogr* 71, 1051-1058.
- 20 [58] Svergun, D., Barberato, C., and Koch, M. H. J. (1995) CRY SOL - A program to evaluate x-ray
21 solution scattering of biological macromolecules from atomic coordinates, *Journal of Applied*
22 *Crystallography* 28, 768-773.
- 23 [59] PyMOL. (2015) The PyMOL Molecular Graphics System, Version 2.0 Schrödinger, LLC.
- 24 [60] Kabsch, W. (2010) XDS, *Acta Crystallogr D Biol Crystallogr* 66, 125-132.
- 25 [61] McCoy, A. J., Grosse-Kunstleve, R. W., Adams, P. D., Winn, M. D., Storoni, L. C., and Read, R. J.
26 (2007) Phaser crystallographic software, *J Appl Crystallogr* 40, 658-674.
- 27 [62] Adams, P. D., Afonine, P. V., Bunkóczi, G., Chen, V. B., Davis, I. W., Echols, N., Headd, J. J., Hung,
28 L. W., Kapral, G. J., Grosse-Kunstleve, R. W., McCoy, A. J., Moriarty, N. W., Oeffner, R., Read,
29 R. J., Richardson, D. C., Richardson, J. S., Terwilliger, T. C., and Zwart, P. H. (2010) PHENIX: a
30 comprehensive Python-based system for macromolecular structure solution, *Acta Crystallogr*
31 *D Biol Crystallogr* 66, 213-221.
- 32 [63] Franke, D., Kikhney, A. G., and Svergun, D. I. (2012) Automated acquisition and analysis of small
33 angle X-ray scattering data, *Nuclear Instruments and Methods in Physics Research Section A:*
34 *Accelerators, Spectrometers, Detectors and Associated Equipment* 689, 52-59.

- 1 [64] Guinier, A. (1939) Diffraction of x-rays of very small angles-application to the study of
2 ultramicroscopic phenomenon, *Annales de Physique* 12, 161-237.
- 3 [65] Konarev, P. V., and Svergun, D. I. (2015) A posteriori determination of the useful data range for
4 small-angle scattering experiments on dilute monodisperse systems, *IUCrJ* 2, 352-360.
- 5 [66] Kearse, M., Moir, R., Wilson, A., Stones-Havas, S., Cheung, M., Sturrock, S., Buxton, S., Cooper,
6 A., Markowitz, S., Duran, C., Thierer, T., Ashton, B., Meintjes, P., and Drummond, A. (2012)
7 Geneious Basic: an integrated and extendable desktop software platform for the
8 organization and analysis of sequence data, *Bioinformatics* 28, 1647-1649.
- 9 [67] Lilkova, E. (2015) The PyMOL Molecular Graphics System, Version 2.0 Schrodinger, LLC. .

10
11
12

13 **Acknowledgements**

14 The synchrotron SAXS data was collected at beamline P12 operated by EMBL Ham-
15 burg at the PETRA III storage ring (DESY, Hamburg, Germany). We would like to thank
16 Tobias Gräwert for the assistance in using the beamline.

17

18 **Funding**

19 The work was funded by project grant 310030B_201273 from the Swiss National Sci-
20 ence Foundation (to C.D.). The Center for Structural studies is funded by the DFG
21 (Grant number 417919780 and INST 208/761-1 FUGG to S.S.).

3.3 Unpublished Results

3.3.1 Implementation of a quantitative online AMPylation assay

3.3.1.1 Introduction and Aim

Since the re-emergence of AMPylation reactions with the Fic proteins VopS and IbpA, the standard methods for qualitative and quantitative AMPylation assays have been autoradiography [172] and scintillation counting [173]. Both methods make use of radioactive ATP-analogs, in most cases ^{32}P - α -ATP or ^{33}P - α -ATP, that are supplemented in enzymatic reactions. Detection of the radioactive signal is either done by image analysis of an exposed film or screen (autoradiography), or more directly the quantification of radioactivity in samples with a scintillation counter. While both methods have proven their worth through high sensitivity and usually low signal/noise ratios, the handling of radioactive material requires increased attention during experiments and specialized facilities. Furthermore, depending on the experimental design, both assays require extended periods of hands-on time, when used as quantitative assays, as time-points have to be handled manually for each monitored reaction.

AMP-antibodies, raised against specific hydroxyl sidechains can be used in western blot analysis and may substitute qualitative autoradiography assays in many cases. However, reliable quantification of western blots is often debatable and relies on many manual steps, including image analysis, that weaken reproducibility if not handled with care [174]. Even if image analysis is becoming more and more automated, the handling of each sample manually is time consuming and makes the assay prone for errors. This becomes immanent, when an increasing number of blots has to be combined into a single data set.

While we were working on the FIC domain of Bep1 from *B. clarridgeia* (Research article I), we wanted to determine kinetic parameters for Bep1 and subsequently study its homologs in other *Bartonella* spp. (e.g. BepA and Bep197). Obviously there are more advantageous assays for the characterization of enzymatic reactions, e.g. the malachite green assay for measurement of phosphatase activity [175]. One of my aims was to test and implement online assays for the qualitative

measurement of AMPylation and to build an automated pipeline for the analysis of kinetic experiments. My focus was mainly on two methods that indirectly measure AMPylation by nucleotide turnover, the phosphate sensor assay and the online Ion exchange chromatography (oIEC) assay.

3.3.1.2 Results

3.3.1.2.1 Phosphate sensor assay

The phosphate sensor (PS) assay uses a fluorophore (PV4406, Thermo Fisher) that increases its emission upon binding inorganic phosphate (P_i). In combination with pyrophosphatase (PPase), this allows the detection of the PP_i byproduct of an AMPylation reaction in real-time. A platerader was used for fully-automated discontinuous measurements at certain time points and the monitored relative fluorescence units (RFU) were converted with the help of a calibration curve (see Methods).

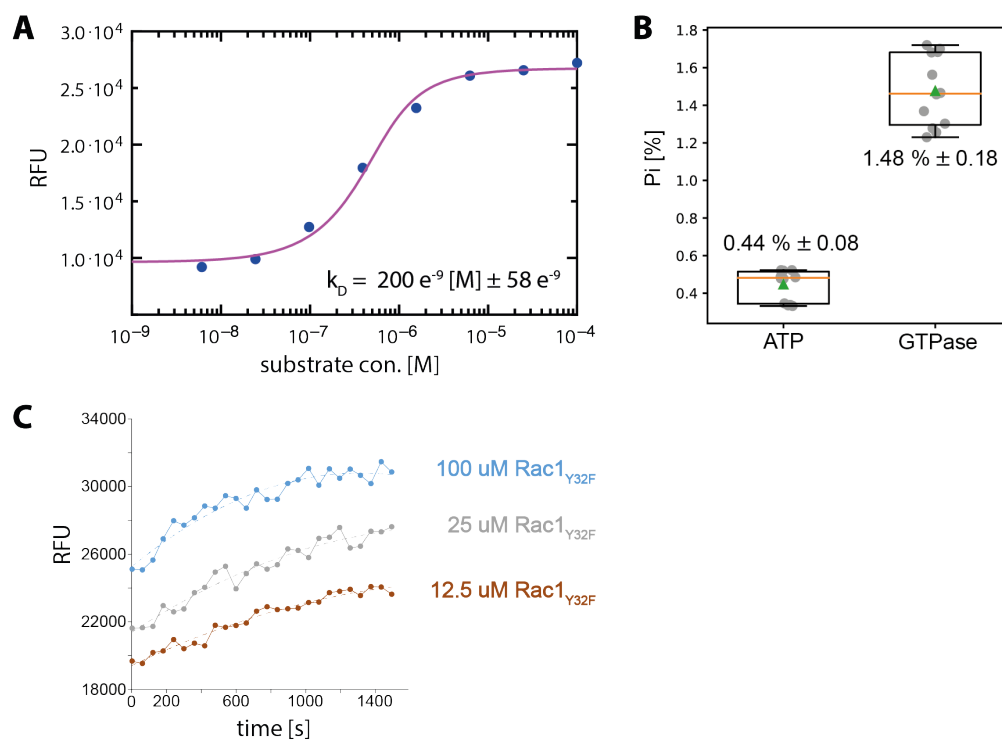


Figure 15: Phosphate Sensor assay controls - (A) Calibration curve for the phosphate sensor assay done with with a dilution series of P_i . (B) P_i contamination of ATP stocks and purified GTPase aliquots. (C) Side reactions leading to an increase of PS signal while monitoring Rac1Y32F with 500 μM ATP.)

3 Results

Calibration showed a tight binding of P_i to the PS with a K_D of 200 nM (Figure 15A), translating into a dynamic range of approximately 25 nM to 2 μ M (PS saturation of 10 % to 90 % respectively).

Control experiments with ultra pure ATP (R1441, Thermo Fisher) and purified GTPase constructs showed contamination with P_i of approximately 0.4 % and 1.5 %, respectively (Figure 15B). At average physiological ATP concentrations of 5 mM one could expect 20 μ M of P_i , thus saturating the PS.

Likewise, GTPase constructs at concentrations of 100 μ M showed enough contaminants to reach the upper limit of the assays dynamic range (\approx 88 % saturation of PS).

Experiments with the AMPylation deficient Rac1 mutant Rac1_{Y32F}, lacking the modifiable Y32, were expected to show no change over time. However, I found that besides the P_i contamination, scaling with the concentration of Rac1_{Y32F}, the measurements showed a continuous increase of fluorescence signal. These results did not change when setting up experiments without PPase or without enzyme (Figure 15C) and could be reproduced with other assays (see below).

Because of the obvious drawbacks of the PS assay, I started to focus on the oIEC assay.

3.3.1.2.2 Online Ion Exchange Chromatography (oIEC) assay

The online Ion Exchange Chromatography (oIEC) assay is an optimized version of conventional ion exchange chromatography. It enables loading of a sample directly during an ongoing reaction without the usually required quenching step [176]. The method allows quantitative analysis of an enzymatic reaction through the detection of chromophoric species (such as nucleotides, proteins and other light absorbing compounds). Combined with automated loops of loading and elution of reaction aliquots it allows to monitor reaction progress in an automated way (see Methods).

Implementation of the assay, namely separation of substrate and product, was a semi-success, as the assay allowed separation of ATP, ADP, AMP and target GTPases (Figure 16). However, modified GTPases (target-AMP) did only shift slightly and were thus visible merely as a shoulder of native GTPase. Fortunately,

it is not necessary to separate the overlapping peaks of native and modified targets, since in such a combined peak, an increase of signal over time can be directly linked to AMP-transfer from ATP to the target.

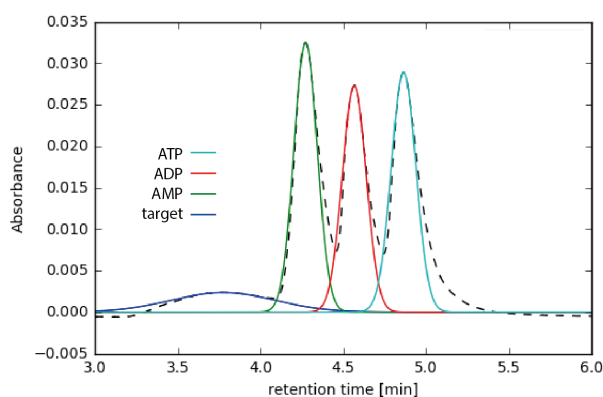


Figure 16: Separation of products and substrates during oIEC - AMP, ADP, ATP and Rac1 as they were eluted from the ion exchange column after optimization.

Figure 17 shows the procedure of acquiring and processing a kinetic data set consisting of a standard AMPylation reaction over a time of 1 hour. 8 measurements are made and sampling time is increased at the end. As peaks are identified and integrated for one chromatogram, the procedure is repeated for the whole dataset. This allows the generation of progress curves for all observed species and subsequent fitting of these curves yields the initial velocity (v_{init}) for each species.

Intriguingly, the emergence of ADP, clearly visible in Figure 17, is not an artefact and happens in nearly every AMPylation reaction. This explains the signal gain with Rac1_{Y32F} and ATP during PS measurements (Figure 15) and could mean that GTPases are hydrolysing small amounts of ATP as a side-reaction. However, the rate of ATP hydrolysis seems to depend greatly on the purity of the protein samples in use. A reaction with a Rac1 batch that was not thoroughly purified is depicted in Figure 18.

It becomes obvious that the hydrolysis rate does not scale with the concentration of GTPase used in a reaction when observing data sets produced with proteins of various purity grades. Most likely, the abundance of ATPases in living cells results in some amounts, in most cases just traces, being carried over during protein purification. This should be taken into consideration when assaying adenylylation,

3 Results

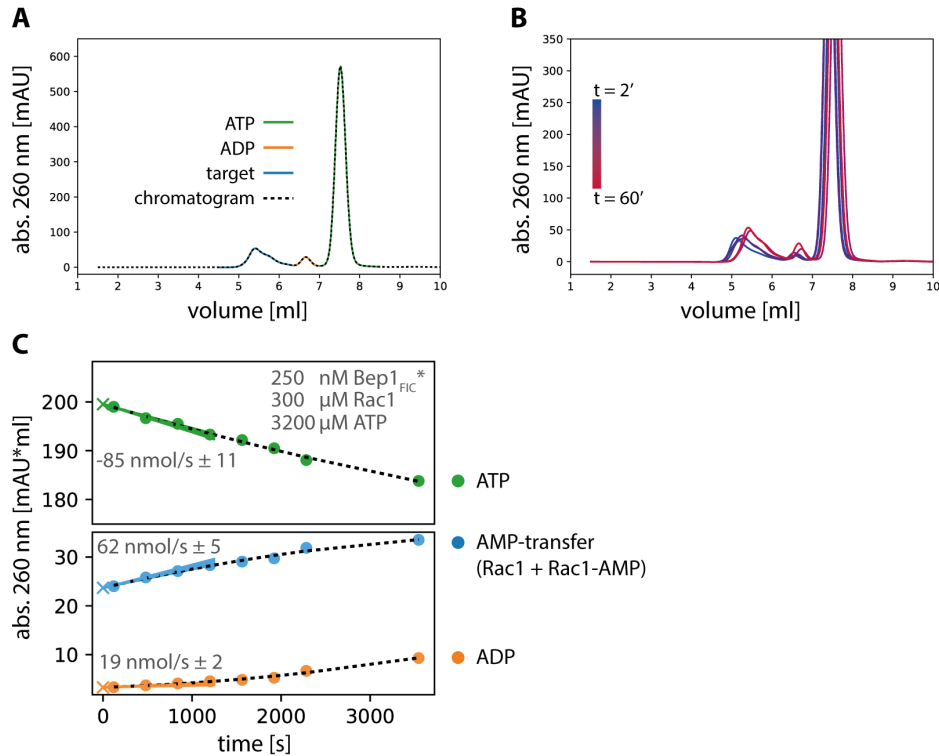


Figure 17: oIEC data collection and processing - (A) Shows a single chromatogram after processing with the peak detection algorithm. (B) shows an overlay of chromatograms at time-points from 2 to 60 minutes with the clearly visible appearance of the target-AMP shoulder and a peak-shift at later time-points. (C) Progress curves as derived from integration of the peaks from each time point of (B). Initial velocities are derived from a heuristic fit and indicated as lines in respective colors.

since methods like autoradiography or scintillation counting are prone to miss this detail. If so, the ATPase pool could be rapidly diminished, especially when using cell lysates in an assay, and results might be considerably biased.

The oIEC was applied in 3.1 and for kinetics of Bep1_{fl}.

3.3.2 Quantitative analysis of Bep1 mediated AMPylation

3.3.2.1 Introduction and Aim

Although most of the experiments were done with the minimal Bep1_{FIC}* construct, I was also working on the full length Bep1 from *B. clarridgeiae* during my PhD. Besides containing the OB-fold, BID-domain and C-terminus, the *B. clarridgeiae*

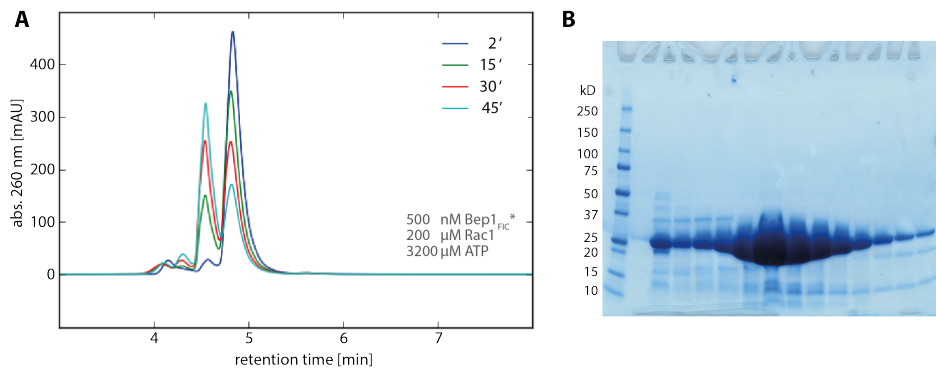


Figure 18: Side-reaction during AMPylation assays - (A) Chromatograms of 4 time-points are superposed, showing the rapid hydrolysis of ATP. (B) shows the Rac1 fractions, later pooled and used in the experiment, with sub-optimal purity-grade

construct, from now on referred to as Bep1_{fl}, was expressed and purified without its anti-toxin BiaA. In contrast, the minimal Fic construct Bep1_{FIC}* (Research article I) was purified together with its tightly bound inhibition relieved anti-toxin, BiaA_{E33G}.

The two homologous Beps show a strong conservation with a pairwise identity of 69.1 %. The catalytic Fic motif is identical. However, the two crucial residues, K117 and D119 in Bep1_{FIC}*, are changed to R117 and E119 in Bep1_{fl}.



Figure 19: Partial alignment of Bep1 homologs - Alignment of the Fic cores of Bep1_{FIC}* from *B. rochalimae* and Bep1_{fl} from *B. clarridgeiae*. Identical sites are shown with gray squares. Crucial sites for target recognition are marked in green.

To find out, if the varying Fic flap sequence had an effect on AMPylation efficiency, I carried out kinetic studies with Bep1_{fl}.

3.3.2.2 Results

3.3.2.2.1 Kinetic parameters for Bep1_{fl}-mediated target AMPylation

To gain kinetic parameters for Bep1_{fl}, $v_{init}(S)$ type Michaelis-Menten plots were derived from ATP and Rac1 dilution series. Measurements were done identical to those in Research article I (see also Methods below) and data was processed with the

3 Results

published python pipeline (https://github.com/FicTeam/HuberDietz_PNAS21).

Dilution series yielded K_M values of 50 μM for ATP and 1.2 mM for Rac1 (Figure 20). For k_{cat} a value of 15 s^{-1} was determined.

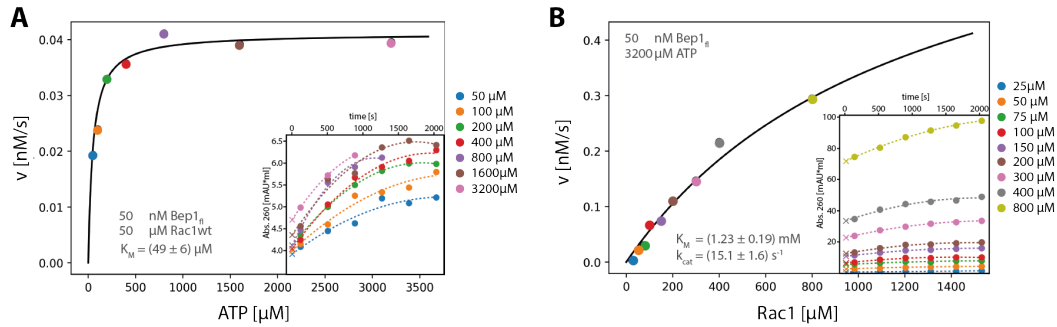


Figure 20: Michaelis-Menten plots for the Bep1_{fl} catalyzed AMPylation of Rac1. - Initial reaction rates as a function of ATP (A) and Rac1 (B) concentrations are plotted and have been derived from respective progress curves shown as insets.

Comparison of values of Bep1_{fl} and Bep1_{FIC}* shows an approximately 8-fold increase of k_{cat} for Bep1_{fl} and an increase of similar magnitude for K_M, ATP (Table 2).

Table 2: Kinetic values for known AMPylators of GTPases

Enzyme	Target	$k_{\text{cat}}/K_M, \text{target}$ [$\text{s}^{-1}\text{mM}^{-1}$]	K_M, ATP [mM]	K_M, target [mM]	k_{cat} [s^{-1}]
VopS _{FIC}	Cdc42 _{Q61L}	100 ± 25 ¹	0.160 ± 0.02 ²	0.180 ± 0.04 ²	18 ± 1.5 ²
IbpA _{FIC2}	Cdc42 _{Q61L}	162 ± 19 ¹	0.73 ± 0.04 ³	1.57 ± 0.15 ³	255 ± 15 ³
Bep1 _{FIC} *	Rac1 _{wt}	1.31 ± 0.46 ¹	0.52 ± 0.02 ⁴	1.44 ± 0.42 ⁴	1.89 ± 0.36 ⁴
Bep1 _{fl}	Rac1 _{wt}	12.2 ± 2.04 ¹	0.05 ± 0.01	1.23 ± 0.19	15.06 ± 1.62

¹ derived from k_{cat} and K_M, target values

² taken from [61]

³ taken from [148]

⁴ taken from Research article I

3.3.2.2 Target AMPylation mediated by Bep1_{fl} for loss- and gain-of-function mutants

To assess the impact of the higher AMPylation efficiency of Bep1_f in relation to $\text{Bep1}_{\text{FIC}^*}$, I analysed the performance of Rac1, Cdc42 and respective loss- and gain-of-function mutants (Figure 21).

As has already been stated in Research article I, under physiological ATP concentrations far above K_M , Bep1 will be saturated with ATP and only partially loaded with target ($[\text{ATP}] \gg K_{M, \text{ATP}}$ and $[\text{target}] \ll K_{M, \text{target}}$). During such conditions, the efficiency constant ($k_{\text{cat}}/K_{M, \text{target}}$) is the only rate defining parameter. Thus the use of the efficiency constant is sufficient when comparing reactions of the same enzyme with different targets.

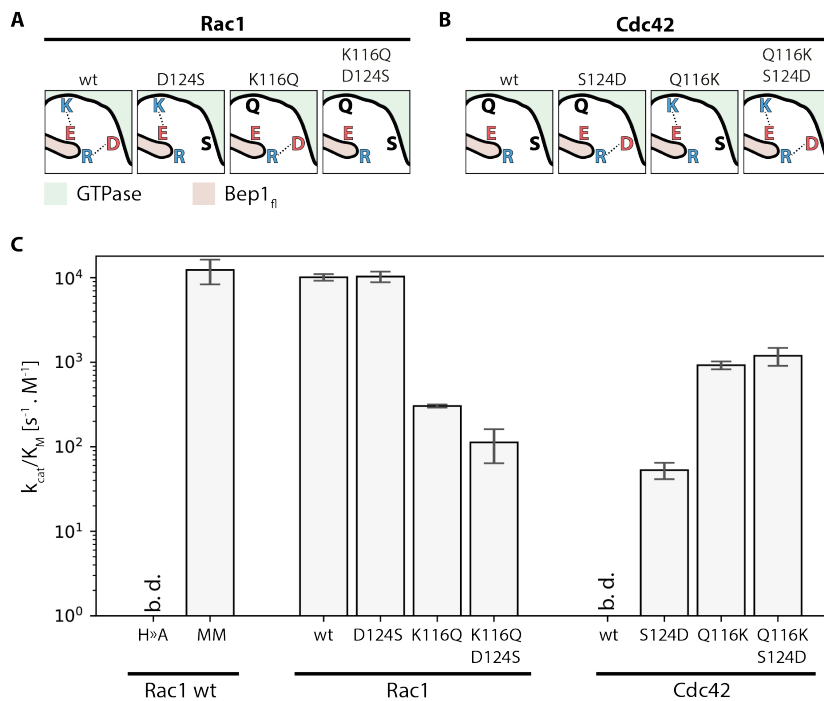


Figure 21: Bep1_f catalyzed AMPylation efficiencies of target variants - Schematic representation of (A) Rac1 loss-of function and (B) Cdc42 gain-of-function mutants. (C) Performance (k_{cat}/K_M) for Bep1_f catalyzed AMPylation of target variants. H \gg A is the catalytically compromised $\text{Bep1}_f\text{H170A}$ mutant. MM shows the efficiency from Michaelis-Menten fits. Other values are derived directly from measurements of initial reaction velocities (v_{init}). b.d., below detection limit. Standard deviation of efficiencies is shown as whiskers.

While the AMPylation performance of Bep1_f with wild-type (wt) Rac1 was in the same range as the performance determined by Michaelis-Menten plots (Figure

3 Results

20, the Rac1_{D124S} mutation seemed to have no effect at all. Rac1_{K116Q} showed a considerably diminished performance (30-fold), and the double loss-of-function mutant Rac1_{K116Q, D124S} even more so (100-fold). Cdc42_{wt} showed no detectable AMPylation, but single mutants Cdc42_{S124D} and Cdc42_{Q116K} revealed a significant signal gain, with Cdc42_{Q116K} performance even exceeding Rac1_{K116Q}. AMPylation of the double-mutant Cdc42_{Q116K, S124D} displayed no observable increase over Cdc42_{Q116K}. Enzymatic efficiency values are listed in Table 3.

To summarize, the data shows a strong dependence for efficient Bep1_{fl}-mediated AMPylation on the E119^{Bep1_{fl}}-K116^{target} interaction. The second salt-bridge R117^{Bep1_{fl}}-D124^{target} is able to compensate for the loss of the more prominent interaction, but doesn't seem to be necessary, if the E119^{Bep1_{fl}}-K116^{target} interaction is unhindered.

Table 3: Bep1 catalyzed AMPylation efficiencies of target variants

Targets	Bep1 _{FIC} *	Bep1 _{fl}
	k _{cat} /K _{M, target} [s ⁻¹ mM ⁻¹]	
Rac1_{wt}	1.18 ± 0.20	10'116 ± 910
Rac1_{D124S}	0.481 ± 0.067	10'317 ± 1'336
Rac1_{K116Q}	0.202 ± 0.009	303 ± 9
Rac1_{K116Q, D124S}	0.043 ± 0.002	113 ± 35
Cdc42_{Q116K, S124D}	0.046 ± 0.003	1'192 ± 333
Cdc42_{Q116K}	0.028 ± 0.002	922 ± 118
Cdc42_{S124D}	0.001 ± 0.002	53 ± 11
Cdc42_{wt}	below detection	below detection

efficiencies (k_{cat}/K_M) derived from vinit values measured by oIEC

3.3.3 Bep1 interactions with GTPases in complex with their regulators

3.3.3.1 Introduction and Aims

The low efficiency of AMPylations catalyzed by Bep1, compared to other Fic toxins like IbpA and VopS, has been puzzling. There are various possible reasons for this. However, kinetic studies of Bep1 showed a conspicuously low target affinity (Research article I and Figure 20). In case of IbpA, that shows a similar low affinity for its target the GTP-locked Cdc42_{Q61L}, a high k_{cat} can compensate for this and yields a 100-fold higher efficiency compared to Bep1_{FIC}*.

This brought up the idea of another factor, that could help in facilitating interactions between Bep1 and its targets by providing an additional interface, that would

augment the flap-target interaction found in Research article I. Obvious candidates are GTPase regulating proteins like GEFs, GAPs and GDIs.

If such an interaction were true, this could push Bep1s efficiency into the range of VopS and IbpA.

One of my aims was thus the analysis of Bep1's capability to modify GTPases in complex with their regulators, GEFs, GAPs and GDIs. For this I started structural and kinetic analysis.

Intriguingly, GDI-bound Cdc42 had been found to be AMPylated by IbpA [148]. Also, since a majority of Rho GTPases is GDI bound, the ability to modify GDI-GTPase complexes would increase the potential targets drastically. Thus, my primary focus was on GDI-complexed target Rho-GTPases.

3.3.3.2 Results

3.3.3.2.1 Model of a potential GTPase-GDI-Bep1 complex

To see if a complex of Rac-GDI would in theory be possible, a model was built from the published Bep1-target model (Research article I) and RhoGDI-1 (ARHGDI1) in complex with Cdc42 (PDB 1DOA). The two complexes were overlaid by superposition of the respective Rho GTPases (Figure 22).

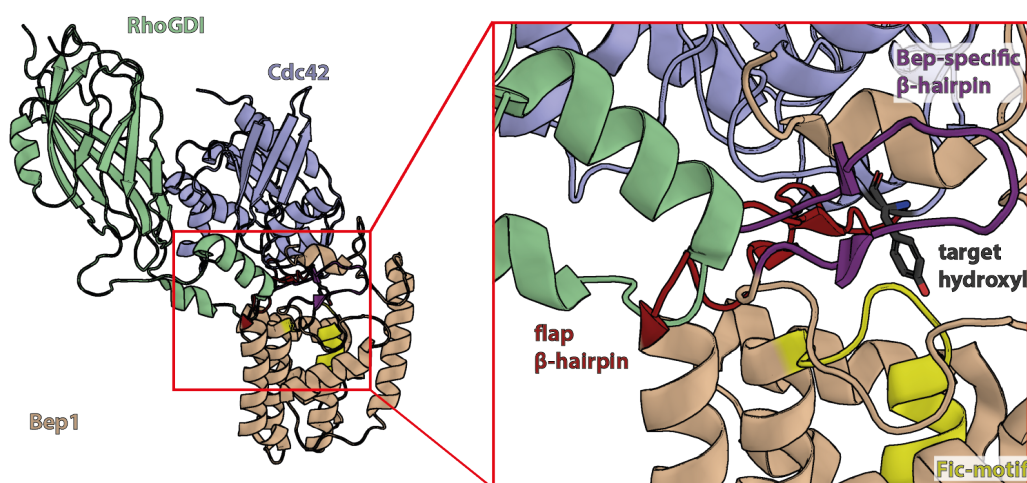


Figure 22: Structure model of a potential GTPase-GDI-Bep1 complex - The model shows the arrangement of RhoGDI-1, Cdc42 and Bep1 after superimposing the Bep1-target model (Research article I) with a GTPase-RhoGDI complex structure (1DOA). Superposition was done on based on the GTPase.

3 Results

Helix $\alpha 2$ from RhoGDI-1 and a short loop following the helix show slight clashes with the base of the flap β -hairpin of Bep1. However, these clashes might be resolved by small rearrangements of helix $\alpha 2$ or by movement of the Bep-flap and hairpin. Provided the clashes could be resolved, the Bep-specific β -hairpin [110] could facilitate an interaction with RhoGDIs helix $\alpha 2$. Both regions are highly conserved in GDIs throughout mammals (see Figure 23) and Bep BID domains [110], respectively. However, there are no obvious interactions, e.g. charged residues in position for salt-bridges, observable.

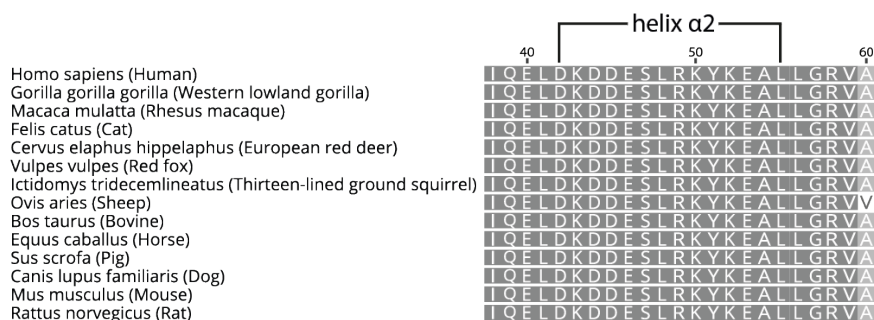


Figure 23: Partial alignment of RhoGDI-1 from mammalian species - Helix $\alpha 2$, potentially targeted by Beps is indicated. Conservation is shown by grey, filled rectangles.

3.3.3.2.2 Rac1-RhoGDI complex from insect cells

Rho-GTPases have to be isoprenylated in order to form a complex with their respective RhoGDI. While modification of GTPases after their production in bacteria can be done, expression of GTPases in insect cells is sufficient to modify them post translationally. Thus, expression in insect-cells was chosen for protein production. Co-expression of Rac1-RhoGDI complex in Sf21 cells worked best with N-terminally His-tagged Rac1 (pMH041) and N-terminally His-tagged RhoGDI (pMH045). Unfortunately, expression of single Rac1 without its GDI failed to extract from cell membranes in all purification attempts.

Whole protein mass spectrometry showed 2 peaks corresponding to masses of 25.225 kD and 27.251 kD for the Rac1- and RhoGDI-construct, respectively. These masses fit the theoretical values of 25.237 kD (Rac1, pMH041) and 27.209 kD (RhoGDI, pMH045), although rather poorly, with deviations higher than expected from other experiments (usually, accuracy is within a few Dalton).

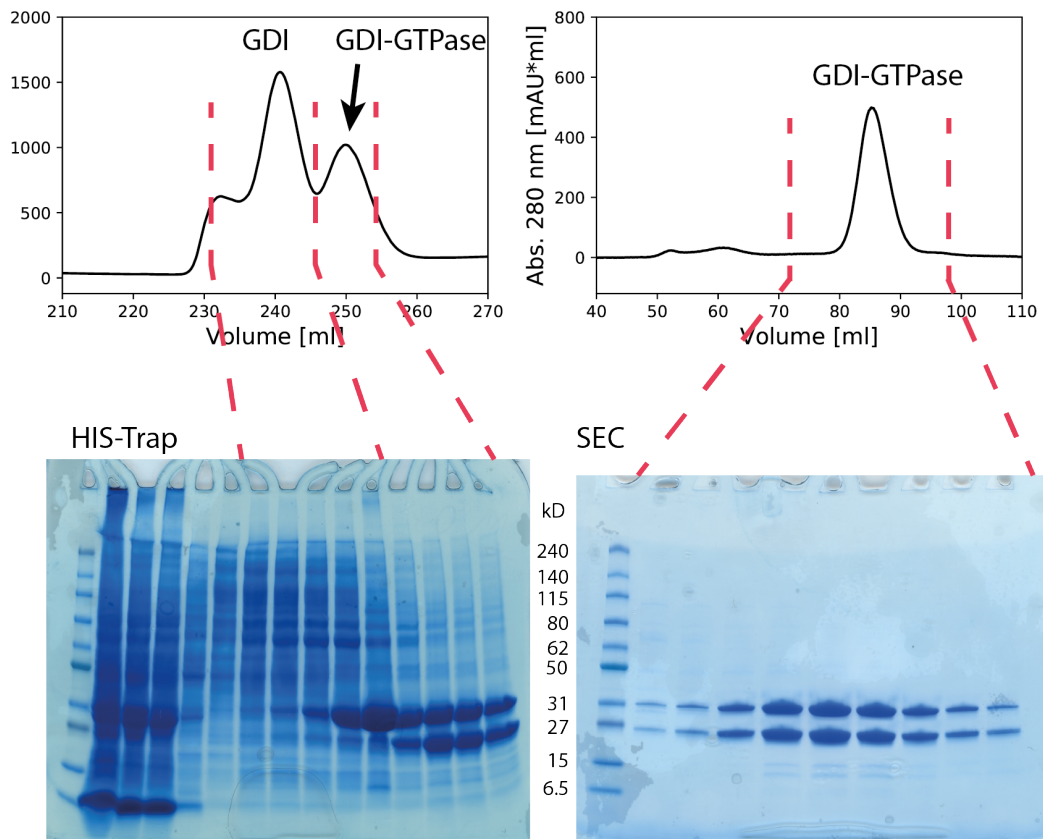


Figure 24: Purification of Rac1-RhoGDI complex - Purification was done by HIS-Trap and consecutive size exclusion chromatography (SEC). While elution from the HIS-trap resulted in mostly overlapping fractions of monomeric GDIs and GTPase-GDI complex, the sole complex could be isolated with SEC.

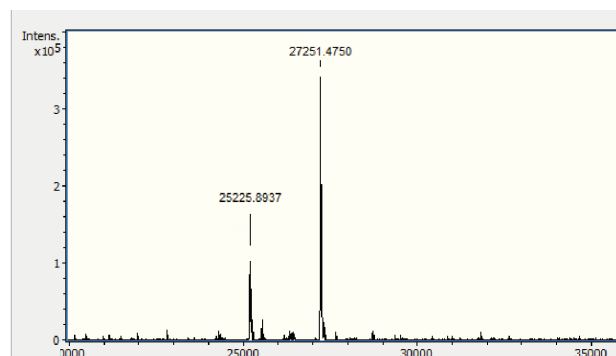


Figure 25: Whole protein mass spectrometry of Rac1-RhoGDI complex - Two peaks corresponding to masses of 25.225 kD and 27.209 kD could be resolved.

3.3.3.2.3 Reaction kinetics of Rac1-RhoGDI complex mediated AMPylation by Bep1_{fl}

Kinetics were done with the Rac1-RhoGDI complex from SF21 and uncomplexed Rac1 from *E. coli*. Although expression of Rac1 in SF21 cells seemed to work, purification of the control-construct could not be achieved.

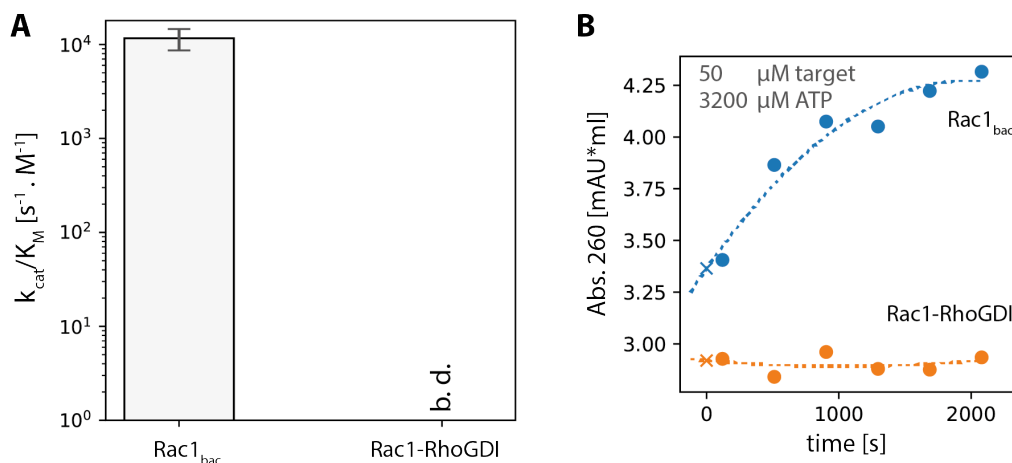


Figure 26: Efficiency of Rac1-GDI complex AMPylation catalyzed by Bep1 - (A) shows AMPylation efficiencies of Bep1_{fl} for Rac1 from *e.coli* and for Rac1-RhoGDI complex. b.d., below detection limit. Efficiency values in (A) are derived from v_{init} values of progress curves as shown in (B).

Regrettably, further experiments have not been in the scope of this thesis and would be necessary to disprove an impact of GDI on Bep1 target AMPylation with complete certainty. However, the results shown above significantly weaken the hypothesis that Bep1 might interact with RhoGDI complexed targets.

3.3.3.2.4 Model of a potential GTPase-GAP-Bep1 complex

Analysis of a theoretical complex of Rac-GDI was based on our Bep1-target model (Research article I) and RhoGAP (ARHGAP1) in complex with RhoA (PDB 5M6X). The two models were overlaid by superposition of respective Rho GTPases (Figure 27).

The model shows massive overlaps between major parts of the GAP and helices α -3, α -4 and α -7 of Bep1. These extensive steric clashes with the Fic core, including the catalytic site, make the possibility of a trimeric complex very unlikely.

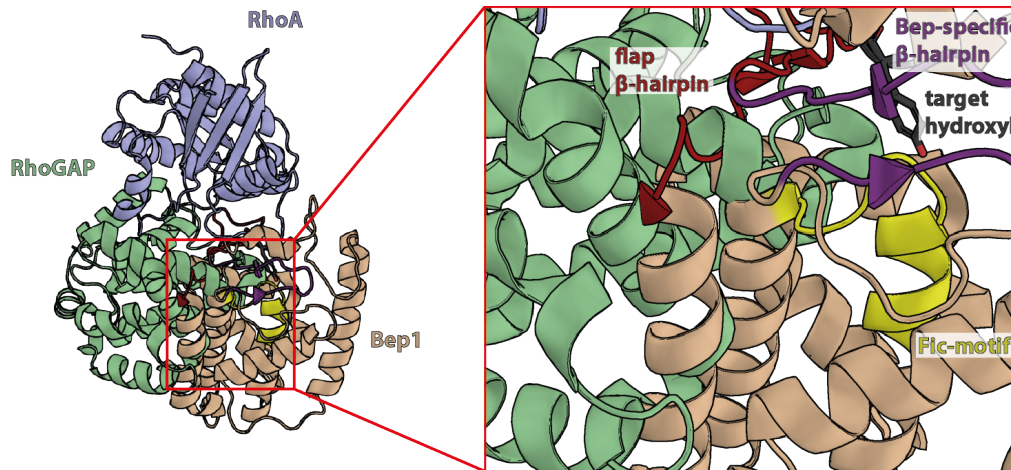


Figure 27: Structure model of a potential GTPase-GAP-Bep1 complex - The model shows the arrangement of RhoGAP, RhoA and Bep1 after superimposing the Bep1-target model (Research article I) with a GTPase-RhoGAP complex structure (5M6X). Superposition was done on based on the GTPase.

3.3.3.2.5 Model of a potential GTPase-GEF-Bep1 complex

Recent work by Simon Marlair showed recruitment of RhoGEF by BepC to interfere with RhoA signaling [44]. Although there was no estimation of the binding affinity published, interactions between BepC and RhoGEF were strong enough for pull down assays with BepC. While the Fic motif of BepC is deteriorated (catalytic H170R) and shows no apparent AMPylation activity, the Fic fold is strongly conserved in Beps, including BepC (Figure 10). On top of the structural conservation, certain Bep-specific elements, like the Bep-specific β -hairpin, show also strong conservation at sequence level [110]. This could indicate, that Bep Fic domains interact with GEFs in a more general way. In addition to merely recruiting GEFs to the membrane for the manipulation of the GTPase cycle, Fic proteins capable of catalyzing AMPylations, could modify target Rho GTPases during their activation through GEFs.

To assess the possibility of a trimeric complex, an overlay of our Bep1-target model and PDZ-RhoGEF (ARHGEF11) in complex with RhoA (PDB 3KZ1) was done (28). Note that the plextrin homology domain (PH) of PDZ-RhoGEF is structurally identical to GEF-H1 (ARHGEF2, PDB 5EFX) at areas facing the Bep1-GTPase complex. The overall RMSD of the PH domains is 0.84 Å (for 541 atoms).

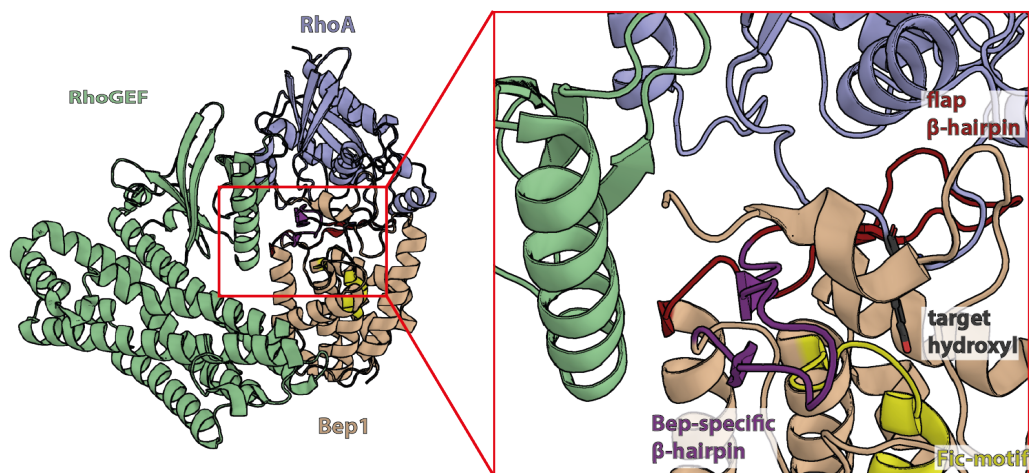


Figure 28: Structure model of a potential GTPase-GEF-Bep1 complex - The model shows the arrangement of RhoGEF, RhoA and Bep1 after superimposing the Bep1-target model (Research article I) with a GTPase-RhoGEF complex structure (3KZ1). Superposition was done on based on the GTPase.

The modeled Bep1-GTPase-GEF complex shows no clashes and puts the Bep-specific β -hairpin exactly at the interface region between GEF and effector (Figure 28). There are no apparent side chain - side chain interactions, but the strongly conserved C-terminal α -helix of the GEF-H1 (ARHGEF2) PH-domain in mammals (Figure 29) would be an ideal target for an interaction.

	helix $\alpha 1$																			
	559								569											
Homo sapiens (Human)	T	A	S	R	D	D	R	S	T	W	I	R	V	I	Q	Q	S	V	R	T
Gorilla gorilla gorilla (Western lowland gorilla)	T	A	S	R	D	D	R	S	T	W	I	R	V	I	Q	Q	S	V	R	T
Macaca mulatta (Rhesus macaque)	T	A	S	R	D	D	R	S	T	W	I	R	V	I	Q	Q	S	V	R	I
Felis catus (Cat)	T	A	S	R	D	D	R	S	T	W	I	R	V	I	Q	Q	S	V	R	V
Cervus elaphus hippelaphus (European red deer)	T	A	S	R	D	D	R	S	T	W	I	R	V	I	Q	Q	S	V	R	W
Vulpes vulpes (Red fox)	T	A	S	R	D	D	R	S	T	W	I	R	V	I	Q	Q	S	V	R	V
Ictidomys tridecemlineatus (Thirteen-lined ground squirrel)	T	A	S	R	D	D	R	S	T	W	I	R	V	I	Q	Q	S	V	R	V
Ovis aries (Sheep)	T	A	S	R	D	D	R	S	T	W	I	R	V	I	Q	Q	S	V	R	V
Bos taurus (Bovine)	T	A	S	R	D	D	R	S	T	W	I	R	V	I	Q	Q	S	V	R	V
Equus caballus (Horse)	T	A	S	R	D	D	R	S	T	W	I	R	V	I	Q	Q	S	V	R	V
Sus scrofa (Pig)	T	A	S	R	D	D	R	S	T	W	I	R	V	I	Q	Q	S	V	R	V
Canis lupus familiaris (Dog)	T	A	S	R	D	D	R	S	T	W	V	R	V	I	Q	Q	S	V	R	V
Mus musculus (Mouse)	A	A	S	R	D	D	R	T	T	W	I	R	V	I	Q	Q	S	V	R	L
Rattus norvegicus (Rat)	A	A	S	R	D	D	R	T	T	W	I	R	V	I	Q	Q	S	V	R	L

Figure 29: Partial alignment of GEF-H1 from mammalian species - The C-terminal helix $\alpha 1$ of GEF-H1 PH domains is indicated. Conservation is indicated by grey, filled rectangles.

Unfortunately, the assessment of Bep1-catalyzed AMPylation of targets in complex with GEF-H1 was outside the scope of this thesis.

3.3.4 Methods

3.3.4.0.1 Cloning of GTPase constructs

Original GTPase constructs were provided by the labs of Jack Dixon and Kim Orth as N-terminal GST-fusion proteins in a pGEX-6.1 vector. The wild-type Rac1 and Cdc42 constructs were cloned into the pET26b derived p7XNH3 vector (FX cloning [177]) to yield pNS056 and pNS038, respectively (N-terminal 10x-HIS-tag). Rac1_{D124S} (pNS033), Rac1_{K116Q} (pNS034), Rac1_{K116Q,D124S} (pNS037), Cdc42_{S124D} (pNS040), Cdc42_{Q116K} (pNS041) and Cdc42_{Q116K,S124D} (pNS042) were derived from pNS056 and pNS038, respectively, via site directed mutagenesis.

3.3.4.0.2 Cloning of insect cell constructs

For the expression of wild-type GTPases in insect cells, the full-length gene was cloned into pAB2G-N-HIS10 and pAB2G-N-GST-HIS10 via Gateway cloning [178] single step BP-LR reactions. For each clone, a PCR with 500 nM attB-Primers (each, forward and reverse), 50 ng pGEX-6.1 vector containing the full-length GTPase sequence, 200 μ M dNTPs, 0.02 U/ μ l iProofTM polymerase and 5 % DMSO was set up (2' 98 °C, 25x [10' 98 °C, 20' 50-70 °C, 20' 72 °C], 5' 72 °C). The PCR was followed by DpnI treatment for 15' at 37 °C and DpnI inactivation for 15' at 80 °C. 100 ng of the treated attB-PCR fragments were mixed with 150 ng Donor vector (pDONORTM221), 150 ng Destination vector (pAB2G-N-HIS10 or pAB2G-N-GST-HIS10), BP ClonaseTM Enzyme Mix and LR ClonaseTM Enzyme Mix in TE buffer (10 mM Tris, 1 mM EDTA, pH 8.0). Reactions were incubated overnight at 16 °C followed by 10' incubation at 37 °C with Proteinase K. Reactions were dialysed and transformed in electrocompetent cells. The transformed bacteria were plated on LB agar plates containing antibiotics (50 μ g/ml Kanamycin, 10 μ g/ml Gentamycin, 7 μ g/ml Tetracyclin) and incubated for 32 to 48 hours for blue-white selection. Colonies were picked for overnight cultures (37 °C) for sequencing and positive clones stored as glycerol stocks.

3.3.4.0.3 Preparation of viruses for insect cell infection

E. coli overnight cultures were grown for each construct from glycerol stocks and 2 ml of culture were spun down for 2' at 16'000g. Each pellet was resuspended in 200 μ l of solution S1 (50 mM Tris/HCL, 10 mM EDTA, pH 8.0, 100 μ g/ml RNase) and incubated for 5'. 200 μ l of solution S2 (0.2 M NaOH, 1 % SDS) were added and the tube inverted 2 times. After about 3' to 5' on ice 200 μ l of solution S3 (3 M

3 Results

KAc, 2 M HAc, pH 5.5) were added and the tube inverted 20 times. Another 5' on ice were followed by 5 min of centrifugation at 16'000g. 1 ml of 70 % isopropanol were mixed with the supernatant, followed by another 5' centrifugation at 16'000g. The DNA pellet was washed once with 500 μ l 70 % ethanol and stored in pure ethanol. The samples were brought into a Laminar flow cabinet, the ethanol was decanted and the pellet left to dry for 30' to 60'. The DNA was resuspended at a in ddH₂O. For each construct 2 wells of a 6-well plate was seeded with 2ml Sf21 cells at $0.5 \cdot 10^6$ cell/ml. The cells were incubated 15' at 27 °C. 10 μ l of DNA, 5 μ l of CellFECTION infection agent and 200 μ l of medium were added and the cells incubated at 27 °C for another 15'. The supernatant was removed and 1 ml of medium was added. The plates were sealed against evaporation with parafilm and incubated at 27 °C for 4-5 days. For each well a T-Flask (500 ml) was prepared with 25 ml of Sf21 cells at $0.6 \cdot 10^6$ cells/ml and supplemented with the supernatant of the corresponding well. Viability, cell size and fluorescence were monitored for 3-4 days. The viruses (V1) were harvested when the cells reached viabilities of around 70-80 %, showed enlarged cell diameters and conspicuous fluorescence. The cultures were spun down at 1'500g for 10' at room temperature and the supernatants - containing the viruses - were stored at 4 °C. Cell pellets were used to check protein expressions. For the production of V2 viruses (later used for the infection of expression cultures), V1 viruses showing good protein expression were chosen. 200 ml of Sf21 cells at $0.6 \cdot 10^6$ cells/ml were prepared and infected with 50 ml of V1 supernatants. After incubation at 27 °C for a few days, the V2 supernatants were harvested around 80% cell viability and stored at 4 °C or as glycerol stocks.

3.3.4.0.4 Protein production in bacteria

Bcl. Bep1 and Bcl. Bep1 H170A and GTPase (pNS033, pNS034, pNS037, pNS038, pNS040, pNS041, pNS042 and pNS056) plasmids were transformed into TSS competent Bl21 (DE3) *E. coli* and the bacteria were plated on LB agar plates (containing 100 μ g/ml Kanamycin). After incubation at 37 °C overnight a colony was picked and used to start an expression culture in auto-induction media. After 6-8 hours of incubation at 37 °C, the temperature was reduced to 20 °C for overnight protein expression. The protein expressing *E. coli* were harvested at an OD₆₀₀ of 12 to 15 by centrifugation at 6'000g for 10' at 12 °C. The pellets were stored at -80 °C or used directly for protein purification.

For purification , pellets were resuspended in IMAC binding buffer (50 mM Hepes

pH 7.5, 500 mM NaCl₂, 5 mM MgCl₂, 1 mM TCEP, 20 mM Imidazol) with a ratio of 1:5 (w/v). The solution was supplemented with 1 spatula tip of RNase A and 1 tablet of cOmplete™ (Roche) per 50 ml of buffer. The samples were stirred for 30' to 60' until they were homogeneous solutions. The *E. coli* were lysed with a FrenchPress or a Microfluidizer at roughly 14'000 PSI (two pass-throughs). This was followed by ultracentrifugation (135'000 g, 35', 12 °C) and filtration (0.22 µm pore size) of the supernatant. Initial purification was done by immobilized metal affinity chromatography (IMAC) with HisTrap™s (5ml High Performance, Cytiva) at 4 °C. The supernatant was loaded with 5 ml/min followed by 8 column volumes of wash with IMAC binding buffer. Elution was done with a linear gradient of IMAC elution buffer (50 mM Hepes pH 7.5, 500 mM NaCl₂, 5 mM MgCl₂, 1 mM TCEP, 500 mM Imidazol) over 10 column volumes. Further purification was done by Size exclusion chromatography (SEC) with HiLoad® 16/600 Superdex® 75 pg columns in SEC buffer (50 mM Hepes pH 7.5, 500 mM NaCl₂, 5 mM MgCl₂, 1 mM TCEP). Samples were applied in 5 ml fractions and run with 1 ml/min. The purest fractions were pooled, concentrated to 10-20 mg/ml and aliquots were frozen (10% glycerol added).

For GTPase purification, salt concentration was reduced to 150 mM NaCl₂ in all buffers.

3.3.4.0.5 Protein production of GTPases in insect cells

Production of GTPases in insect cells was either done by expressing GTPases alone or co-expressing them with RhoGST. 4 l of SF9 insect cells were infected with either 40 ml of a single V2 supernatant (1:100) or 20 ml of each of two different V2 supernatants (for co-expressions) and incubated for a few days at 27 °C until the majority of cells showed the typical characteristics of infection and protein expression (big diameter, viability at 80-85 % and conspicuous fluorescence). The cells were harvested by centrifugation at 1'000 g for 10' at 4 °C and the cell pellets frozen at -80 °C or used directly for protein purification.

For purification of monomeric GTPases the pellets were resuspended in IMAC binding buffer (50 mM Hepes at pH 8, 500 mM NaCl, 1mM TCEP) supplemented with protease inhibitors (PMSF, Bestatin, E-64, Pepstatin A, Phenthrolin, PA), DNase and 0.1 % NP-40. The insect cells were disrupted with 20 strokes in a douncer on ice. Initial purification was done by immobilized metal affinity chromatography (IMAC) with HisTrap™s (Cytiva, High Performance) at 4 °C. The supernatant was

3 Results

loaded with 5 ml/min followed by 8 column volumes of wash with IMAC binding buffer. Elution was done with a linear gradient of IMAC elution buffer (50 mM Hepes pH 7.5, 150 mM NaCl₂, 5 mM MgCl₂, 1 mM TCEP, 500 mM Imidazol) over 10 column volumes. A second purification step was done by Size exclusion chromatography (SEC) with HiLoad[®] 16/600 Superdex[®] 75 pg columns in SEC buffer (50 mM Hepes pH 7.5, 150 mM NaCl₂, 5 mM MgCl₂, 1 mM TCEP). Samples were applied in 5 ml fractions and run with 1 ml/min. The purest fractions were pooled. A last purification was done by glutathione resin batch purification. 2 ml of resin (GenScript) were washed 3 times with ddH₂O once with GST binding buffer. The pooled SEC fractions were mixed with the glutathione resin and gently rocked overnight at 4 °C. The resin was washed 2 times with GST binding buffer. The protein was eluted with GST elution buffer by 3 consecutive incubations of 10' on ice. The pure fractions were pooled, concentrated and aliquots were frozen (10 % glycerol added).

GTPase-RhoGST dimers were purified similar to monomeric GTPases, but the glutathione resin batch purification was skipped. Instead the pooled fractions were directly concentrated and aliquots frozen in liquid nitrogen (10 % glycerol added).

3.3.4.0.6 Mass spectrometry

Whole protein mass analysis was done with a Bruker Daltonics microTOF. Sample preparations were done by diluting proteins down to 0.2 mg/ml in a total volume of 50 µl of 90 % H₂O, 10 % Acetonitril and 0.1 % Formic acid. The pH of each sample was checked and adjusted to be less than 3 when necessary. Microspin Columns from The Nest Group were activated with 100 µl pure Acetonitril and spun at 2000 rpm for 1'. The Spin columns were then washed 2 times with 100 µl H₂O (1' at 1500 rpm). 50 µl of samples per column were applied and the columns spun for 1' at 1500 rpm. Columns were washed 2 times with 50 µl of 90 % H₂O, 10 % Acetonitril and 0.1 % Formic acid (1' at 1500 rpm). Samples were eluted with 50 µl 20 % H₂O, 80 % Acetonitril and 0.1 % Formic acid (2' at 1500 rpm). Samples were then frozen in liquid nitrogen or applied directly to the microTOF.

20 µl of the samples were directly injected into the microTOF by Electron spray ionization (ESI) and analyzed with the time-of-flight (TOF) method. Data acquisition and analysis was done with Hystar (3.2.49.9).

3.3.4.1 Phosphate sensor assay

The phosphate sensor (PV4406, Thermo Fisher) allows the detection of inorganic Phosphate (P_i) via a fluorophore, whose emission at 450 nm (after excitation at 430 nm) is increased about 6- to 8-fold upon binding of P_i . Since an AMPylation reaction produces pyrophosphate ($\text{ATP} + \text{target} \xrightarrow{\text{FIC}} \text{target-AMP} + \text{PPi}$), a coupled reaction with pyrophosphatase (PPase, EF0221, Thermo Fisher) had to be set up, to liberate P_i . In this set-up, the measured amount of P_i is equal to the amount of modified target (target-AMP) adjusted by a factor of 2.

GTPases used in the phosphate sensor assay were either used in their APO-form or underwent GDP loading. For this, the GTPase was incubated with 25x excess of GDP and 50x excess of EDTA for 20' at room temperature. The exchange was stopped with 100x excess of MgCl_2 and the buffer exchanged (50 mM Hepes pH 7.5, 150 mM NaCl_2 , 5 mM MgCl_2 , 1 mM TCEP) with a HiTrap™ Desalting column (Cytiva, 17-1408-01).

Reactions were set up with 500 nM phosphate sensor, 2 U PPase, and varying concentrations of effector and target. The reactions were started by addition of ATP and the progress followed in 96-well plates (total reaction volume of 120 μl per well) with a plate reader (BioTek Synergy models) by measuring the fluorescence $\frac{430}{450}$ nM every 20" for 20'.

3.3.4.2 Online ion exchange chromatography (oIEC) assay

The online ion exchange chromatography (oIEC) assay allows quantitative analysis of enzymatic reaction through the detection of chromophoric species (such as nucleotides, proteins and other light absorbing compounds). The method is based on an interplay of standard chromatography equipment, in which an auto-sampler periodically injects an aliquote of a reaction mix into the chromatography system. An Aekta controls the flow and the ratio of running and elution buffers that run through an ion exchange column (Resource™Q 1ml, Cytiva, GE17-1177-01).

After a sample is injected, charged components bind to the columns matrix with different strength. This immobilizes them and stops the reaction. After a short washing step, an eluent (eg. high salt concentrations) is gradually or stepwise increased to elute the components. Together with the varying relative binding strength to the columns matrix of the differently charged compounds, this results

3 Results

in different elution volumes for the components. The Aktas UV detector allows to resolve these components in chromatograms as separate peaks. Putting together chromatograms from each timed injection allows to follow a reaction, by following the change of absorbance for each peak.

For each reaction, a mix of effector and target was prepared. The reaction was started by adding ATP to a total reaction volume of 200 μ l. An aliquote (20 μ l) was injected by the autosampler every 4' to 6' (depending on the set-up) while maintaining a flow of 4 ml/min with running buffer (20 mM Tris/HCL pH 8.5). Elution was done with a gradual increase of elution buffer (20 mM Tris/HCL pH 8.5, 1 M $(\text{NH}_4)_2\text{SO}_4$) to 20%. After a short step to 100% of elution buffer the column was equilibrated with running buffer before the next injection. A total of 6 to 8 injections (20 μ l each) were done for each reaction and the chromatograms processed.

3.3.4.2.1 oIEC processing

Chromatogram data was extracted from Unicorn data files using the pycorn script from Yasar L. Ahmed (<https://pypi.org/project/pycorn/>) and a baseline (average of 5 chromatograms after injection of a blank) was subtracted to get corrected chromatograms. Peaks were detected based on a script from Eli Billauer (<http://billauer.co.il/peakdet.html>) that returns maxima and minima. These maxima and minima were used to set peak characteristics like centre, amplitude and width. Peaks were then integrated numerically (or for test cases as Gaussian's) to yield the relative amount of the underlying component of a reaction at each specific time point. For the processing of chromatograms, a python script was written and published on github (https://github.com/FicTeam/HuberDietz_PNAS21).

3.3.4.2.2 Kinetic fitting

To follow the progress of each reaction, the relative quantities of the GTPase peak of each time-point, extracted from chromatograms collected at 260 nm, were analysed. Note that the GTPase peak comprised target (native) and product (AMPylated) GTPase. However, the increase of absorbance at 260 nm can be attributed directly to the emergence of nucleotide and thus AMPylation of the target. The progress curves were fitted best by a heuristic quadratic function to yield initial velocities. Absolute velocities were derived through calibration with an ATP dilution series. Enzymatic parameters (K_M and k_{cat}) for both substrates, ATP and target, were

obtained by fitting the Michaelis-Menten equation to the initial velocities of the respective substrate dilution series (see also [179]).

In single-substrate kinetics, the concentration of target variants were corrected by the back-extrapolated peak absorbance at $t = 0$. ATP concentrations were kept at 3.2 mM (supplemented with 6.4 mM MgCl_2) and Bep1 concentrations were varied to adjust for the reaction speed with different GTPase variants.

3.3.4.2.3 Software

Structure models were done with Pymol [180] and all alignments exported from Geneious Prime (2020.2.4).

4 Discussion

4.1 The oIEC as new gold standard for AMPylation assays

Implementation of the oIEC as an assay to study AMPylation in a quantitative setting has shown great potential in this study, with the apparent advantage, that the transferred AMP moiety can be directly detected by conventional UV sensors. However, this criteria is also met by many more substrates and products, as has been shown by others [176], thus the oIEC is a unique tool with applications even outside the intended scope.

While the separation of substrate and product is a prerequisite for applying the assay, thorough optimization of chromatography parameters (e.g. adjusting pH, salt concentration, or a change of column) allows a wide range of adjustments for this requirement.

In a first step of the oIEC, reagents are trapped on the column, leading to an "enrichment" of bound components. The volume applied to the column can be adjusted to increase (higher injection volume) or decrease (lower injection volume) the signal intensity during the elution and detection step. Thus, oIEC is applicable for a wide range of reactions that might require unusually low or high concentrations of reaction components.

Moreover, different components of a reaction can be analysed in parallel. This allows fitting of kinetic models in a global fashion, considering all monitored progressions at once, and yielding more robust results. Furthermore, compared to other automated assays, like the Malachite green or Phosphate sensor assays, side-reactions can be monitored and factored in during data processing.

Considering the abundance of FPLC equipment in modern laboratories, the ease of use of oIEC and its many advantages, oIEC has the potential to greatly improve data quality and reduce time investment of many kinetic studies.

4.2 Two intermolecular Salt bridges are crucial for Bep1-mediated target AMPylation

Structural and kinetic analysis of Bep1 homologs from two different *Bartonella spp.* have shown, that charged residues on the elongated Fic-flap of Bep1 are crucial for target specificity. While the residues at the tip are not fully conserved, they carry residues of the same charge, that is (R/K)₁₁₇ and (E/D)₁₁₉. The importance of salt-bridges of these Bep1 residues with partners of the Rho-insert (D₁₂₄) and the G4-motif (K₁₁₆), respectively, has been illuminated by Research article I and unpublished Results with Bep1_{fl}. Since gain-of-function double mutants could not reach full Rac1wt AMPylation efficiencies, there are probably other contributing factors that have yet to be found.

In experiments with both Bep1 constructs a more dominant interaction with residues of the G4-motif was observable, although interactions with residues of the Rho-insert were sufficient for effective target AMPylation.

The narrow target selectivity towards the Rac subfamily, excluding both Cdc42 and RhoA with their branches, probably plays a role in the "stealth" infection strategy of *Bartonella*. Since inactivation of RhoA has been shown to trigger a response of the innate immune system through activation of the pyrin inflammasome [27], avoiding this pathway might be beneficial for *Bartonella*.

While a few toxins evolved to interfere with Rho GTPase in a more specific manner, by modulating their regulators (GAPs, GEFs and GDIs) instead of interacting with GTPases directly, there had not been any indication of a toxin, that would target exclusively proteins of the Rac branch before [2]. This makes the new found exquisite selectivity also interesting as a molecular tool, eg. in research targeting impaired signaling of Rac-subfamily GTPases, that can be linked to a diminished ability for ROS production in immune cells, leading to constricted clearing of bacterial infections [181, 182].

4.3 Secretion of Bep1 full-length requires partial unfolding

The novel structure of a full-length Bartonella effector shows a boomerang-like shape with "wings" of roughly 10 nm in length. This curious shape puts a vast space between FIC and BID domain and yields a bulky multi-domain protein, that has to undergo rearrangements and probably partial unfolding for secretion through the narrow T4SS channel.

The "wings" were found to be flexible, as the angle between them becomes wider when the temperature increases. When reaching temperatures close to the mammalian body temperature, partial unfolding of the protein has been detected by SAX measurement.

Although the increase in temperature shows already the onsets of unfolding of Bep1, the T4SS probably contains an unfolding machinery, that guides these changes in a more controlled way.

4.4 A novel fold (CB) structurally links FIC-OB and BID domains

The C-terminus of Bep1, that has previously been described as unstructured tail [124, 125], shows a distinct fold. Interestingly, this CB-fold (C-terminal α -helical bundle) appears to be evolutionary linked to the BID domain, as the stalk of the elongated BID seems crucial to bury the otherwise exposed hydrophobic core.

The CB-fold is spatially positioned between the OB-fold and the BID-domain of Bep1 and acts as a scaffolding between those two.

Most striking is the conservation of certain hot-spots throughout Beps containing a FIC domain. A few conserved charged residues, including a central complex salt bridge (K₃₉₈-E₃₂₄-R₄₉₈) and respective hydrogen bonds, in the OB-fold, the BID domain and the CB-fold are key to link the different domains together.

Speculations about the exceptionally conserved L₃₂₀(I/V)PxE₃₂₄ motif have already been made by Stanger et. al. [126]. It is evident that this hydrophobic motif covers the hydrophobic core of the CB-fold in Beps, while the motifs E₃₂₄ plays a central part for interactions with OB- and CB-folds.

4.5 Inhibition relieved anti-toxin could interfere with ATP exchange

Kinetic characterization of Bep1_{fl} compared to Bep1_{FIC}* showed a significant difference of the reaction rates with k_{cat} values approximately one order of magnitude higher for the full length protein. Both proteins show an identical FIC fold and a fully conserved catalytic loop. This could imply an influence of domains not present in Bep1_{FIC}*. However, after analysis of the full-length Bep1 structure in Research article II (in revision for Structure) this seems improbable, since elements following the FIC domain don't come close to the catalytic site.

A more fitting hypothesis comes to mind, considering that Bep1_{FIC}* is tightly bound to its inhibition relieved antitoxin (BiaA_{E33G}), that usually blocks proper positioning of ATP. Intriguingly, ATP affinity seems also higher for the full length protein, hinting that this might be entirely the effect of the missing anti-toxin.

Although lacking the crucial glutamate, that competes with the ATP γ -phosphate, the inhibitory helix could still influence ATP exchange rates. This might explain the higher affinity for ATP and a higher target AMPylation rate, altogether.

4.6 Recruitment of GEFs by Beps could be a more general mechanism

Low AMPylation rates for Bep1_{FIC}* initially brought up the idea, that Beps might recruit another factor in host cells for the AMPylation of targets. Preliminary analysis of GDI-, GAP- and GEF-complexed Rho GTPases ruled out GAPs, as steric clashes are too severe to allow binding of Beps to such a complex. Analysis of a potential GDI-target-BEP complex looked promising at first, but preliminary experiments showed no AMPylation activity.

A structure model of an interaction between Bep1 and PDZ-RhoGEF in complex with RhoA showed no steric hindrance and positions the Bep-specific β -hairpin [110] directly opposite a conserved region of the GEF.

A recently published study shows that BepC interacts with GEF-H1 and directs

4 Discussion

it to the plasma membrane for the modulation of RhoA signaling [44]. BepC has a deteriorated FIC motif and apparently doesn't AMPylate its targets. However, taking into account these new findings, recruitment of GEFs by Beps could be a more general mechanism, also applied by AMPylating Beps that would modify their targets during their activation through GEFs.

5 References

Bibliography

- [1] Jorge E. Galán. Common Themes in the Design and Function of Bacterial Effectors. *Cell Host and Microbe*, 5(6):571–579, 6 2009.
- [2] Klaus Aktories. Bacterial protein toxins that modify host regulatory GTPases. *Nature Reviews Microbiology*, 9(7):487–498, 5 2011.
- [3] Klaus Aktories. Rho-modifying bacterial protein toxins. *Pathogens and Disease*, 73(9), 12 2015.
- [4] Jacqueline Cherfils and Mahel Zeghouf. Regulation of small GTPases by GEFs, GAPs, and GDIs. *Physiological Reviews*, 93(1):269–309, 1 2013.
- [5] Alan Hall. The cellular functions of small GTP-binding proteins. *Science*, 249(4969):635–640, 1990.
- [6] Henry R. Bourne, David A. Sanders, and Frank McCormick. The GTPase superfamily: A conserved switch for diverse cell functions. *Nature*, 348(6297):125–132, 1990.
- [7] I. R. Vetter and A. Wittinghofer. The guanine nucleotide-binding switch in three dimensions. *Science*, 294(5545):1299–1304, 11 2001.
- [8] Johannes L. Bos, Holger Rehmann, and Alfred Wittinghofer. GEFs and GAPs: Critical Elements in the Control of Small G Proteins. *Cell*, 129(5):865–877, 6 2007.
- [9] Hui Zong, Kozo Kaibuchi, and Lawrence A. Quilliam. The Insert Region of RhoA Is Essential for Rho Kinase Activation and Cellular Transformation. *Molecular and Cellular Biology*, 21(16):5287–5298, 8 2001.
- [10] Patrick J. Roberts, Natalia Mitin, Patricia J. Keller, Emily J. Chenette, James P. Madigan, Rachel O. Currin, Adrienne D. Cox, Oswald Wilson, Paul Kirschmeier, and Channing J. Der. Rho family GTPase modification and dependence on CAAX motif-signaled posttranslational modification. *Journal of Biological Chemistry*, 283(37):25150–25163, 9 2008.
- [11] Paul M. Müller, Juliane Rademacher, Richard D. Bagshaw, Celina Wortmann, Carolin Barth, Jakobus van Unen, Keziban M. Alp, Girolamo Giudice, Rebecca L. Eccles, Louise E. Heinrich, Patricia Pascual-Vargas, Marta Sanchez-Castro, Lennart Brandenburg, Geraldine Mbamalu, Monika Tucholska, Lisa

- Spatt, Maciej T. Czajkowski, Robert William Welke, Sunqu Zhang, Vivian Nguyen, Trendelina Rrustemi, Philipp Trnka, Kiara Freitag, Brett Larsen, Oliver Popp, Philipp Mertins, Anne Claude Gingras, Frederick P. Roth, Karen Colwill, Chris Bakal, Olivier Pertz, Tony Pawson, Evangelia Petsalaki, and Oliver Rocks. Systems analysis of RhoGEF and RhoGAP regulatory proteins reveals spatially organized RAC1 signalling from integrin adhesions. *Nature Cell Biology*, 22(4):498–511, 4 2020.
- [12] Miguel C. Seabra. Membrane association and targeting of prenylated Ras-like GTPases. *Cellular Signalling*, 10(3):167–172, 1998.
- [13] Alfred Wittinghofer and Ingrid R Vetter. Structure-function relationships of the G domain, a canonical switch motif. *Annual Review of Biochemistry*, 80:943–971, 2011.
- [14] Antje Schaefer, Nathalie R. Reinhard, and Peter L. Hordijk. Toward understanding RhoGTPase specificity: Structure, function and local activation. *Small GTPases*, 5(2), 12 2014.
- [15] Joseph Tcherkezian and Nathalie Lamarche-Vane. Current knowledge of the large RhoGAP family of proteins. *Biology of the Cell*, 99(2):67–86, 2 2007.
- [16] Etienne Boulter, Rafael Garcia-Mata, Christophe Guilluy, Adi Dubash, Guendalina Rossi, Patrick J. Brennwald, and Keith Burridge. Regulation of Rho GTPase crosstalk, degradation and activity by RhoGDI1. *Nature Cell Biology*, 12(5):477–483, 5 2010.
- [17] David Michaelson, Joseph Silletti, Gretchen Murphy, Peter D’Eustachio, Mark Rush, and Mark R. Philips. Differential localization of Rho GTPases in live cells: Regulation by hypervariable regions and RhoGDI binding. *Journal of Cell Biology*, 152(1):111–126, 1 2001.
- [18] Kent L. Rossman, Channing J. Der, and John Sondek. GEF means go: Turning on Rho GTPases with guanine nucleotide-exchange factors. *Nature Reviews Molecular Cell Biology*, 6(2):167–180, 2 2005.
- [19] Céline DerMardirossian and Gary M. Bokoch. GDIs: Central regulatory molecules in Rho GTPase activation. *Trends in Cell Biology*, 15(7):356–363, 7 2005.

Bibliography

- [20] Aron B. Jaffe and Alan Hall. Rho GTPases: Biochemistry and biology. *Annual Review of Cell and Developmental Biology*, 21:247–269, 2005.
- [21] Keith Burridge and Krister Wennerberg. Rho and Rac Take Center Stage. *Cell*, 116(2):167–179, 1 2004.
- [22] Anne J. Ridley and Alan Hall. The small GTP-binding protein rho regulates the assembly of focal adhesions and actin stress fibers in response to growth factors. *Cell*, 70(3):389–399, 8 1992.
- [23] Anne J. Ridley, Hugh F. Paterson, Caroline L. Johnston, Dagmar Diekmann, and Alan Hall. The small GTP-binding protein rac regulates growth factor-induced membrane ruffling. *Cell*, 70(3):401–410, 8 1992.
- [24] Gary M. Bokoch. Regulation of innate immunity by Rho GTPases. *Trends in Cell Biology*, 15(3):163–171, 3 2005.
- [25] Michel R. Popoff. Bacterial factors exploit eukaryotic Rho GTPase signaling cascades to promote invasion and proliferation within their host. *Small GTPases*, 5(MAY), 2014.
- [26] Monica Ruse and Ulla G. Knaus. New players in TLR-mediated innate immunity: PI3K and small Rho GTPases. *Immunologic Research*, 34(1):33–48, 2006.
- [27] Hao Xu, Jieling Yang, Wenqing Gao, Lin Li, Peng Li, Li Zhang, Yi Nan Gong, Xiaolan Peng, Jianzhong Jeff Xi, She Chen, Fengchao Wang, and Feng Shao. Innate immune sensing of bacterial modifications of Rho GTPases by the Pyrin inflammasome. *Nature*, 513(7517):237–241, 9 2014.
- [28] G. Aaron Hobbs, Bingying Zhou, Adrienne D. Cox, and Sharon L. Campbell. Rho GTPases, oxidation, and cell redox control. *Small GTPases*, 5(MAY), 5 2014.
- [29] Erica Werner. GTPases and reactive oxygen species: Switches for killing and signaling. *Journal of Cell Science*, 117(2):143–153, 1 2004.
- [30] Anh T. P. Ngo, Ivan Parra-Izquierdo, Joseph E. Aslan, and Owen J. T. McCarty. Rho GTPase regulation of reactive oxygen species generation and signaling in platelet function and disease. *Small GTPases*, page 21541248.2021.1878001, 1 2021.

- [31] Robert H. Insall and Laura M. Machesky. Actin Dynamics at the Leading Edge: From Simple Machinery to Complex Networks. *Developmental Cell*, 17(3):310–322, 9 2009.
- [32] Naomi E. Harwood and Facundo D. Batista. The cytoskeleton coordinates the early events of B-cell activation. *Cold Spring Harbor Perspectives in Biology*, 3(2):1–15, 2011.
- [33] Peter Beemiller and Matthew F. Krummel. Mediation of T-cell activation by actin meshworks. *Cold Spring Harbor perspectives in biology*, 2(9), 2010.
- [34] Franck Debeurme, Antoine Picciocchi, Marie Claire Dagher, Didier Grunwald, Sylvain Beaumel, Franck Fieschi, and Marie José Stasia. Regulation of NADPH oxidase activity in phagocytes: Relationship between FAD/NADPH binding and oxidase complex assembly. *Journal of Biological Chemistry*, 285(43):33197–33208, 10 2010.
- [35] Alison E.M. Adams, Douglas I. Johnson, Richard M. Longnecker, Barbara F. Sloat, and John R. Pringle. CDC42 and CDC43, two additional genes involved in budding and the establishment of cell polarity in the yeast *Saccharomyces cerevisiae*. *Journal of Cell Biology*, 111(1):131–142, 1990.
- [36] H. F. Paterson, A. J. Self, M. D. Garrett, I. Just, K. Aktories, and A. Hall. Microinjection of recombinant p21(rho) induces rapid changes in cell morphology. *Journal of Cell Biology*, 111(3):1001–1007, 1990.
- [37] Anne J. Ridley and Alan Hall. Snails, Swiss, and serum: the solution for Rac 'n' Rho. *Cell*, 116(2 Suppl), 2004.
- [38] Patrice Boquet and Emmanuel Lemichez. Bacterial virulence factors targeting Rho GTPases: Parasitism or symbiosis? *Trends in Cell Biology*, 13(5):238–246, 5 2003.
- [39] Mark P. Stevens, Andrea Friebel, Lowrie A. Taylor, Michael W. Wood, Philip J. Brown, Wolf Dietrich Hardt, and Edouard E. Galyov. A Burkholderia pseudomallei type III secreted protein, BopE, facilitates bacterial invasion of epithelial cells and exhibits guanine nucleotide exchange factor activity. *Journal of Bacteriology*, 185(16):4992–4996, 8 2003.

Bibliography

- [40] Wolf Dietrich Hardt, Li Mei Chen, Kornel E. Schuebel, Xosé R. Bustelo, and Jorge E. Galán. *S. typhimurium* Encodes an activator of Rho GTPases that induces membrane ruffling and nuclear responses in host cells. *Cell*, 93(5):815–826, 5 1998.
- [41] Gretel Buchwald, Andrea Friebel, Jorge E. Galán, Wolf Dietrich Hardt, Alfred Wittinghofer, and Klaus Scheffzek. Structural basis for the reversible activation of a Rho protein by the bacterial toxin SopE. *EMBO Journal*, 21(13):3286–3295, 7 2002.
- [42] Zhiwei Huang, Sarah E. Sutton, Adam J. Wallenfang, Robert C. Orchard, Xiaojing Wu, Yingcai Feng, Jijie Chai, and Neal M. Alto. Structural insights into host GTPase isoform selection by a family of bacterial GEF mimics. *Nature Structural and Molecular Biology*, 16(8):853–860, 8 2009.
- [43] Neal M. Alto, Feng Shao, Cheri S. Lazar, Renee L. Brost, Gordon Chua, Seema Mattoo, Stephen A. McMahon, Partho Ghosh, Timothy R. Hughes, Charles Boone, and Jack E. Dixon. Identification of a bacterial type III effector family with G protein mimicry functions. *Cell*, 124(1):133–145, 1 2006.
- [44] Simon Marlaire and Christoph Dehio. Bartonella effector protein C mediates actin stress fiber formation via recruitment of GEF-H1 to the plasma membrane. *PLOS Pathogens*, 17(1):e1008548, 1 2021.
- [45] Chunyan Wang, Haoran Zhang, Jiaqi Fu, Meng Wang, Yuhao Cai, Tianyun Ding, Jiezhong Jiang, Jane E Koehler, Xiaoyun Liu, and Congli Yuan. Bartonella type IV secretion effector BepC induces stress fiber formation through activation of GEF-H1. *PLOS Pathogens*, 17(1):e1009065, 1 2021.
- [46] Claudia Hoffmann, Marius Pop, Jost Leemhuis, Jörg Schirmer, Klaus Aktories, and Gudula Schmidt. The *Yersinia pseudotuberculosis* Cytotoxic Necrotizing Factor (CNF γ) Selectively Activates RhoA. *Journal of Biological Chemistry*, 279(16):16026–16032, 4 2004.
- [47] Gilles Flatau, Emmanuel Lemichez, Michel Gauthier, Pierre Chardin, Sonia Paris, Carla Fiorentini, and Patrice Boquet. Toxin-induced activation of the G protein p21 Rho by deamidation of glutamine. *Nature*, 387(6634):729–733, 1 1997.

- [48] Lori Buetow, Gilles Flatau, Katy Chiu, Patrice Boquet, and Partho Ghosh. Structure of the Rho-activating domain of Escherichia coli cytotoxic necrotizing factor 1. *Nature Structural Biology*, 8(7):584–588, 2001.
- [49] Gudula Schmidt, Peter Sehr, Matthias Wilm, Jörg Selzer, Matthias Mann, and Klaus Aktories. Gin 63 of Rho is deamidated by Escherichia coli cytotoxic necrotizing factor-1. *Nature*, 387(6634):725–729, 1997.
- [50] Gudula Schmidt, Jörg Selzer, Maria Lerm, and Klaus Aktories. The Rho-deamidating cytotoxic necrotizing factor 1 from Escherichia coli possesses transglutaminase activity: Cysteine 866 and histidine 881 are essential for enzyme activity. *Journal of Biological Chemistry*, 273(22):13669–13674, 5 1998.
- [51] Andrey S. Selyunin, Sarah E. Sutton, Bethany A. Weigele, L. Evan Reddick, Robert C. Orchard, Stefan M. Bresson, Diana R. Tomchick, and Neal M. Alto. The assembly of a GTPase-kinase signalling complex by a bacterial catalytic scaffold. *Nature*, 469(7328):107–113, 1 2011.
- [52] Klaus Aktories and Alan Hall. Botulinum ADP-ribosyltransferase C3: a new tool to study low molecular weight GTP-binding proteins. *Trends in Pharmacological Sciences*, 10(10):415–418, 1989.
- [53] E J Rubin, D M Gill, P Boquet, and M R Popoff. Functional modification of a 21-kilodalton G protein when ADP-ribosylated by exoenzyme C3 of Clostridium botulinum. *Molecular and Cellular Biology*, 8(1):418–426, 1 1988.
- [54] Yixin Fu and Jorge E. Galán. A Salmonella protein antagonizes Rac-1 and Cdc42 to mediate host-cell recovery after bacterial invasion. *Nature*, 401(6750):293–297, 9 1999.
- [55] Ulrich Von Pawel-Rammingen, Maxim V. Telepnev, Gudula Schmidt, Klaus Aktories, Hans Wolf-Watz, and Roland Rosqvist. GAP activity of the Yersinia YopE cytotoxin specifically targets the Rho pathway: A mechanism for disruption of actin microfilament structure. *Molecular Microbiology*, 36(3):737–748, 2000.
- [56] Sina Mohammadi and Ralph R. Isberg. Yersinia pseudotuberculosis virulence determinants invasin, YopE, and YopT modulate RhoG activity and localization. *Infection and Immunity*, 77(11):4771–4782, 11 2009.

Bibliography

- [57] Karine Brugirard-Ricaud, Eric Duchaud, Alain Givaudan, Pierre Alain Girard, Frank Kunst, Noel Boemare, Michel Brehélin, and Robert Zumbihl. Site-specific antiphagocytic function of the *Photobacterium luminescens* type III secretion system during insect colonization. *Cellular Microbiology*, 7(3):363–371, 3 2005.
- [58] Jörg Selzer, Fred Hofmann, Gundula Rex, Matthias Wilm, Matthias Mann, Ingo Just, and Klaus Aktories. Clostridium novyi α -toxin-catalyzed incorporation of GlcNAc into Rho subfamily proteins. *Journal of Biological Chemistry*, 271(41):25173–25177, 1996.
- [59] I. Just, J. Selzer, M. Wilm, C. Von Eichel-Streiber, M. Mann, and K. Aktories. Glucosylation of Rho proteins by Clostridium difficile toxin B. *Nature*, 375(6531):500–503, 6 1995.
- [60] Carolyn A. Worby, Seema Mattoo, Robert P. Kruger, Lynette B. Corbeil, Antonius Koller, Juan C. Mendez, Bereket Zekarias, Cheri Lazar, and Jack E. Dixon. The Fic Domain: Regulation of Cell Signaling by Adenylylation. *Molecular Cell*, 34(1):93–103, 4 2009.
- [61] Melanie L. Yarbrough, Yan Li, Lisa N. Kinch, Nick V. Grishin, Haydn L. Ball, and Kim Orth. AMPylation of Rho GTPases by Vibrio VopS disrupts effector binding and downstream signaling. *Science*, 323(5911):269–272, 1 2009.
- [62] A. Sekine, M. Fujiwara, and S. Narumiya. Asparagine residue in the rho gene product is the modification site for botulinum ADP-ribosyltransferase. *Journal of Biological Chemistry*, 264(15):8602–8605, 5 1989.
- [63] P. Chardin, P. Boquet, P. Madaule, M. R. Popoff, E. J. Rubin, and D. M. Gill. The mammalian G protein rhoC is ADP-ribosylated by Clostridium botulinum exoenzyme C3 and affects actin microfilaments in Vero cells. *EMBO Journal*, 8(4):1087–1092, 1989.
- [64] Harald Genth, Ralf Gerhard, Akio Maeda, Mutsuki Amano, Kozo Kaibuchi, Klaus Aktories, and Ingo Just. Entrapment of Rho ADP-ribosylated by Clostridium botulinum C3 exoenzyme in the Rho-guanine nucleotide dissociation inhibitor-1 complex. *Journal of Biological Chemistry*, 278(31):28523–28527, 8 2003.

- [65] Holger Barth, Claudia Olenik, Peter Sehr, Gudula Schmidt, Klaus Aktories, and Dieter K. Meyer. Neosynthesis and activation of Rho by *Escherichia coli* cytotoxic necrotizing factor (CNF1) reverse cytopathic effects of ADP-ribosylated Rho. *Journal of Biological Chemistry*, 274(39):27407–27414, 9 1999.
- [66] Peter Sehr, Gili Joseph, Harald Genth, Ingo Just, Edgar Pick, and Klaus Aktories. Glucosylation and ADP ribosylation of Rho proteins: Effects on nucleotide binding, GTPase activity, and effector coupling. *Biochemistry*, 37(15):5296–5304, 4 1998.
- [67] Feng Shao, Peter M. Merritt, Zhaoqin Bao, Roger W. Innes, and Jack E. Dixon. A *Yersinia* effector and a *Pseudomonas* avirulence protein define a family of cysteine proteases functioning in bacterial pathogenesis. *Cell*, 109(5):575–588, 5 2002.
- [68] Katja Barthelmes, Evelyn Ramcke, Hyun Seo Kang, Michael Sattler, and Aymelt Itzen. Conformational control of small GTPases by AMPylation. *Proceedings of the National Academy of Sciences of the United States of America*, 117(11):5772–5781, 3 2020.
- [69] M. H. Stoler, T. A. Bonfiglio, R. T. Steigbigel, and M. Pereira. An atypical subcutaneous infection associated with acquired immune deficiency syndrome. *American Journal of Clinical Pathology*, 80(5):714–718, 1983.
- [70] P. E. LeBoit, T. G. Berger, B. M. Egbert, J. H. Beckstead, T. S.B. Yen, and M. H. Stoler. Bacillary angiomatosis: The histopathology and differential diagnosis of a pseudoneoplastic infection in patients with human immunodeficiency virus disease. *American Journal of Surgical Pathology*, 13(11):909–920, 11 1989.
- [71] Leonard N. Slater, David F. Welch, Diane Hensel, and Danese W. Coody. A Newly Recognized Fastidious Gram-Negative Pathogen as a Cause of Fever and Bacteremia. *New England Journal of Medicine*, 323(23):1587–1593, 12 1990.
- [72] Jane E. Koehler, Frederick D. Quinn, Timothy G. Berger, Philip E. LeBoit, and Jordan W. Tappero. Isolation of *Rochalimaea* Species from Cutaneous

Bibliography

- and Osseous Lesions of Bacillary Angiomatosis. *New England Journal of Medicine*, 327(23):1625–1631, 12 1992.
- [73] R L Regnery, B E Anderson, J E Clarridge, M C Rodriguez-Barradas, D C Jones, and J H Carr. Characterization of a novel Rochalimaea species, *R. henselae* sp. nov., isolated from blood of a febrile, human immunodeficiency virus-positive patient. *Journal of Clinical Microbiology*, 30(2):265–274, 1992.
- [74] D F Welch, D A Pickett, L N Slater, A G Steigerwalt, and D J Brenner. *Rochalimaea henselae* sp. nov., a cause of septicemia, bacillary angiomatosis, and parenchymal bacillary peliosis. *Journal of Clinical Microbiology*, 30(2):275–280, 1992.
- [75] D. J. Brenner, S. P. O'Connor, H. H. Winkler, and A. G. Steigerwalt. Proposals to unify the genera bartonella and Rochalimaea, with descriptions of Bartonella quintana comb. nov., Bartonella vinsonii comb. nov., Bartonella henselae comb. nov., and Bartonella elizabethae comb. nov., and to remove the family Bartonellaceae f. *International Journal of Systematic Bacteriology*, 43(4):777–786, 10 1993.
- [76] Michel Drancourt, Jean Luc Mainardi, Philippe Brouqui, François Vandenesch, Anne Carta, Franck Lehnert, Jerome Etienne, Fred Goldstein, Jacques Acar, and Didier Raoult. Bartonella (Rochalimaea) quintana Endocarditis in Three Homeless Men. *New England Journal of Medicine*, 332(7):419–423, 2 1995.
- [77] David H. Spach, Andrew S. Kanter, Molly J. Dougherty, Ann M. Larson, Marie B. Coyle, Don J. Brenner, Bala Swaminathan, Ghassan M. Matar, David F. Welch, Richard K. Root, and Walter E. Stamm. Bartonella (Rochalimaea) quintana Bacteremia in Inner-City Patients with Chronic Alcoholism. *New England Journal of Medicine*, 332(7):424–428, 2 1995.
- [78] D. H. Spach and J. E. Koehler. Bartonella-associated infections. *Infectious Disease Clinics of North America*, 12(1):137–155, 1998.
- [79] Ralf Schüle, Anja Seubert, Christian Gille, Christa Lanz, Yves Hansmann, Yves Piémont, and Christoph Dehio. Invasion and persistent intracellular colonization of erythrocytes: A unique parasitic strategy of the emerging pathogen Bartonella. *Journal of Experimental Medicine*, 193(9):1077–1086, 5 2001.

- [80] Christoph Dehio. Molecular and cellular basis of Bartonella pathogenesis. *Annual Review of Microbiology*, 58:365–390, 9 2004.
- [81] Alexander Harms and Christoph Dehio. Intruders below the Radar: Molecular pathogenesis of Bartonella spp. *Clinical Microbiology Reviews*, 25(1):42–78, 1 2012.
- [82] Rachel C. Abbott, Bruno B. Chomel, Rickie W. Kasten, Kim A. Floyd-Hawkins, Yoko Kikuchi, Jane E. Koehler, and Niels C. Pedersen. Experimental and natural infection with Bartonella henselae in domestic cats. *Comparative Immunology, Microbiology and Infectious Diseases*, 20(1):41–51, 1997.
- [83] Jan Koesling, Toni Aebischer, Christine Falch, Ralf Schüle, and Christoph Dehio. Cutting Edge: Antibody-Mediated Cessation of Hemotropic Infection by the Intraerythrocytic Mouse Pathogen Bartonella grahamii. *The Journal of Immunology*, 167(1):11–14, 7 2001.
- [84] Brandee L. Pappalardo, Talmage Brown, Jody L. Gookin, Carolyn L. Morrill, and Edward B. Breitschwerdt. Granulomatous disease associated with Bartonella infection in 2 dogs. *Journal of veterinary internal medicine / American College of Veterinary Internal Medicine*, 14(1):37–42, 1 2000.
- [85] A. N. Gurfield, H. J. Boulouis, B. B. Chomel, R. W. Kasten, R. Heller, C. Bouillin, C. Gandoin, D. Thibault, C. C. Chang, F. Barrat, and Y. Piemont. Epidemiology of Bartonella infection in domestic cats in France. *Veterinary Microbiology*, 80(2):185–198, 5 2001.
- [86] B. B. Chomel. Cat-scratch disease and bacillary angiomatosis. *OIE Revue Scientifique et Technique*, 15(3):1061–1073, 1996.
- [87] Burt E Anderson and Mark A Neuman. Bartonella spp. as emerging human pathogens. *Clinical Microbiology Reviews*, 10(2):203–219, 1997.
- [88] C. Dehio and A. Sander. Bartonella as emerging pathogens. In *Trends in Microbiology*, volume 7, pages 226–228. Elsevier Ltd, 6 1999.
- [89] Jun Hang, Kristin E. Mullins, Robert J. Clifford, Fatma Onmus-Leone, Yu Yang, Ju Jiang, Mariana Leguia, Matthew R. Kasper, Ciro Maguiña, Emil P. Lesho, Richard G. Jarman, Allen L. Richards, and David Blazes.

Bibliography

- Complete genome sequence of *Bartonella ancashensis* strain 20.00, isolated from the blood of a patient with verruga peruana. *Genome Announcements*, 3(6), 2015.
- [90] Laura W. Lamps and Margie A. Scott. Cat-scratch disease: historic, clinical, and pathologic perspectives. *American journal of clinical pathology*, 121 Suppl, 2004.
- [91] Erick Chinga-Alayo, E. Huarcaya, C. Nasarre, R. del Aguila, and A. Llanos-Cuentas. The influence of climate on the epidemiology of bartonellosis in Ancash, Peru. *Transactions of the Royal Society of Tropical Medicine and Hygiene*, 98(2):116–124, 2 2004.
- [92] Margaret Kosek, Rosa Lavarello, Robert H. Gilman, Jose Delgado, Ciro Maguiña, Manuela Verástegui, Andres G. Lescano, Vania Mallqui, Jon C. Kosek, Sixto Recavarren, and Lilia Cabrera. Natural history of infection with *Bartonella bacilliformis* in a nonendemic population. *Journal of Infectious Diseases*, 182(3):865–872, 2000.
- [93] Judith Chamberlin, Larry W. Laughlin, Sofia Romero, Nelson Soloórzano, Scott Gordon, Richard G. Andre, Paul Pachas, Heidi Friedman, Carlos Ponce, and Douglas Watts. Epidemiology of endemic *Bartonella bacilliformis*: A prospective cohort study in a Peruvian mountain valley community. *Journal of Infectious Diseases*, 186(7):983–990, 10 2002.
- [94] Henri L. Saenz, Philipp Engel, Michèle C. Stoeckli, Christa Lanz, Günter Raddatz, Muriel Vayssier-Taussat, Richard Birtles, Stephan C. Schuster, and Christoph Dehio. Genomic analysis of *Bartonella* identifies type IV secretion systems as host adaptability factors. *Nature Genetics*, 39(12):1469–1476, 12 2007.
- [95] Philippe Brouqui, Bernard Lascola, Veronique Roux, and Didier Raoult. Chronic *Bartonella quintana* Bacteremia in Homeless Patients. *New England Journal of Medicine*, 340(3):184–189, 1999.
- [96] Peter J. Hotez. Neglected infections of poverty in the United States of America. *PLoS Neglected Tropical Diseases*, 2(6):e256, 6 2008.

- [97] Christoph Dehio and Renée M. Tsois. Type IV effector secretion and subversion of host functions by bartonella and brucella species. In *Current Topics in Microbiology and Immunology*, volume 413, pages 269–295. Springer Verlag, 2017.
- [98] G. Marignac, F. Barrat, B. Chomel, M. Vayssier-Taussat, C. Gandoin, C. Bouillin, and H. J. Boulouis. Murine model for Bartonella birtlesii infection: New aspects. *Comparative Immunology, Microbiology and Infectious Diseases*, 33(2):95–107, 3 2010.
- [99] Peng Zhang, Bruno B. Chomel, Maureen K. Schau, Jeanna S. Goo, Sara Droz, Karen L. Kelminson, Smitha S. George, Nicholas W. Lerche, and Jane E. Koehler. A family of variably expressed outer-membrane proteins (Vomp) mediates adhesion and autoaggregation in Bartonella quintana. *Proceedings of the National Academy of Sciences of the United States of America*, 101(37):13630–13635, 9 2004.
- [100] Christoph Dehio. Bartonella - Host-cell interactions and vascular tumour formation. *Nature Reviews Microbiology*, 3(8):621–631, 8 2005.
- [101] Simone C. Eicher and Christoph Dehio. Bartonella entry mechanisms into mammalian host cells. *Cellular Microbiology*, 14(8):1166–1173, 8 2012.
- [102] Bruno B. Chomel, Henri Jean Boulouis, Edward B. Breitschwerdt, Rickie W. Kasten, Muriel Vayssier-Taussat, Richard J. Birtles, Jane E. Koehler, and Christoph Dehio. Ecological fitness and strategies of adaptation of Bartonella species to their hosts and vectors. *Veterinary Research*, 40(2), 3 2009.
- [103] Sabrina Siamer and Christoph Dehio. New insights into the role of Bartonella effector proteins in pathogenesis. *Current Opinion in Microbiology*, 23:80–85, 2 2015.
- [104] Dorsey L. Kordick, Talmage T. Brown, Kwangok Shin, and Edward B. Breitschwerdt. Clinical and pathologic evaluation of chronic Bartonella henselae or Bartonella clarridgeiae infection in cats. *Journal of Clinical Microbiology*, 37(5):1536–1547, 1999.
- [105] K. L. Karem, K. A. Dubois, S. L. McGill, and R. L. Regnery. Characterization of Bartonella henselae-specific immunity in BALB/c mice. *Immunology*, 97(2):352–358, 1999.

Bibliography

- [106] Arto T. Pulliainen and Christoph Dehio. Persistence of Bartonella spp. stealth pathogens: From subclinical infections to vasoproliferative tumor formation. *FEMS Microbiology Reviews*, 36(3):563–599, 5 2012.
- [107] Filomena Iannino, Stefania Salucci, Andrea Di Provvido, Alessandra Paolini, and Enzo Ruggieri. Bartonella infections in humans dogs and cats. *Veterinaria Italiana*, 54(1):63–72, 1 2018.
- [108] Philipp Engel, Walter Salzburger, Marius Liesch, Chao Chin Chang, Soichi Maruyama, Christa Lanz, Alexandra Calteau, Aurélie Lajus, Claudine Médigue, Stephan C. Schuster, and Christoph Dehio. Parallel evolution of a type IV secretion system in radiating lineages of the host-restricted bacterial pathogen bartonella. *PLoS Genetics*, 7(2):e1001296, 2 2011.
- [109] Houchaima Ben-Tekaya, Jean Pierre Gorvel, and Christoph Dehio. Bartonella and Brucella-weapons and strategies for stealth attack. *Cold Spring Harbor Perspectives in Medicine*, 3(8):a010231, 8 2013.
- [110] Alexander Harms, Francisca H.I.D. Segers, Maxime Quebatte, Claudia Mistl, Pablo Manfredi, Jonas Körner, Bruno B. Chomel, Michael Kosoy, Soichi Maruyama, Philipp Engel, and Christoph Dehio. Evolutionary dynamics of pathoadaptation revealed by three independent acquisitions of the VirB/D4 type IV secretion system in Bartonella. *Genome Biology and Evolution*, 9(3):761–776, 3 2017.
- [111] Eric Cascales and Peter J. Christie. The versatile bacterial type IV secretion systems. *Nature Reviews Microbiology*, 1(2):137–149, 2003.
- [112] P. J. Christie. Type IV secretion: Intercellular transfer of macromolecules by systems ancestrally related to conjugation machines. *Molecular Microbiology*, 40(2):294–305, 2001.
- [113] Gunnar Schröder, Ralf Schuelein, Maxime Quebatte, and Christoph Dehio. Conjugative DNA transfer into human cells by the VirB/VirD4 type IV secretion system of the bacterial pathogen Bartonella henselae. *Proceedings of the National Academy of Sciences of the United States of America*, 108(35):14643–14648, 8 2011.

- [114] Matxalen Llosa, Craig Roy, and Christoph Dehio. Bacterial type IV secretion systems in human disease. In *Molecular Microbiology*, volume 73, pages 141–151. John Wiley & Sons, Ltd, 7 2009.
- [115] Alexander Wagner and Christoph Dehio. Role of distinct type-IV-secretion systems and secreted effector sets in host adaptation by pathogenic Bartonella species. *Cellular Microbiology*, 21(3), 3 2019.
- [116] Ralf Schulein and Christoph Dehio. The VirB/VirD4 type IV secretion system of Bartonella is essential for establishing intraerythrocytic infection. *Molecular Microbiology*, 46(4):1053–1067, 11 2002.
- [117] Muriel Vayssier-Taussat, Danielle Le Rhun, Hong Kuan Deng, Francis Biville, Sandra Cescau, Antoine Danchin, Geneviève Marignac, Evelyne Lenaour, Henri Jean Boulouis, Maria Mavris, Lionel Arnaud, Huanming Yang, Jing Wang, Maxime Quebatte, Philipp Engel, Henri Saenz, and Christoph Dehio. The Trw type IV secretion system of Bartonella mediates host-specific adhesion to erythrocytes. *PLoS Pathogens*, 6(6):e1000946, 6 2010.
- [118] M. Y. Kosoy, E. K. Saito, D. Green, E. L. Marston, D. C. Jones, and J. E. Childs. Experimental evidence of host specificity of Bartonella infection in rodents. *Comparative Immunology, Microbiology and Infectious Diseases*, 23(4):221–238, 2000.
- [119] Harry H. Low, Francesca Gubellini, Angel Rivera-Calzada, Nathalie Braun, Sarah Connery, Annick Dujeancourt, Fang Lu, Adam Redzej, Rémi Fronzes, Elena V. Orlova, and Gabriel Waksman. Structure of a type IV secretion system. *Nature*, 508(7497):550–553, 2014.
- [120] Gabriel Waksman. From conjugation to T4S systems in Gram-negative bacteria: a mechanistic biology perspective. *EMBO reports*, 20(2):e47012, 2 2019.
- [121] Julieta Aguilar, John Zupan, Todd A. Cameron, and Patricia C. Zambryski. Agrobacterium type IV secretion system and its substrates form helical arrays around the circumference of virulence-induced cells. *Proceedings of the National Academy of Sciences of the United States of America*, 107(8):3758–3763, 2 2010.

Bibliography

- [122] Tiago R.D. Costa, Laith Harb, Pratick Khara, Lanying Zeng, Bo Hu, and Peter J. Christie. Type IV secretion systems: Advances in structure, function, and activation. *Molecular Microbiology*, (October 2020):1–17, 2021.
- [123] Peter J. Christie, Neal Whitaker, and Christian González-Rivera. Mechanism and structure of the bacterial type IV secretion systems. *Biochimica et Biophysica Acta - Molecular Cell Research*, 1843(8):1578–1591, 8 2014.
- [124] Alexander Harms, Marius Liesch, Jonas Körner, Maxime Québatte, Philipp Engel, and Christoph Dehio. A bacterial toxin-antitoxin module is the origin of inter-bacterial and inter-kingdom effectors of Bartonella. *PLoS Genetics*, 13(10), 10 2017.
- [125] Ralf Schulein, Patrick Guye, Thomas A. Rhomberg, Michael C. Schmid, Gunnar Schröder, Annette C. Vergunst, Ilaria Carena, and Christoph Dehio. A bipartite signal mediates the transfer of type IV secretion substrates of Bartonella henselae into human cells. *Proceedings of the National Academy of Sciences of the United States of America*, 102(3):856–861, 1 2005.
- [126] Frédéric V. Stanger, Tjaart A.P. de Beer, David M. Dranow, Tilman Schirmer, Isabelle Phan, and Christoph Dehio. The BID Domain of Type IV Secretion Substrates Forms a Conserved Four-Helix Bundle Topped with a Hook. *Structure*, 25(1):203–211, 1 2017.
- [127] F. Scheidegger, Y. Ellner, P. Guye, T. A. Rhomberg, H. Weber, H. G. Augustin, and Christoph Dehio. Distinct activities of Bartonella henselae type IV secretion effector proteins modulate capillary-like sprout formation. *Cellular Microbiology*, 11(7):1088–1101, 2009.
- [128] Matthias C. Truttmann, Thomas A. Rhomberg, and Christoph Dehio. Combined action of the type IV secretion effector proteins BepC and BepF promotes invasome formation of Bartonella henselae on endothelial and epithelial cells. *Cellular Microbiology*, 13(2):284–299, 2 2011.
- [129] Matthias C. Truttmann, Patrick Guye, and Christoph Dehio. BID-F1 and BID-F2 domains of bartonella henselae effector protein BepF trigger together with BepC the formation of invasome structures. *PLoS ONE*, 6(10):e25106, 10 2011.

- [130] Matthias Selbach, Florian Ernst Paul, Sabine Brandt, Patrick Guye, Oliver Daumke, Steffen Backert, Christoph Dehio, and Matthias Mann. Host Cell Interactome of Tyrosine-Phosphorylated Bacterial Proteins. *Cell Host and Microbe*, 5(4):397–403, 4 2009.
- [131] Isabel Sorg, Christoph Schmutz, Yun Yueh Lu, Katja Fromm, Lena K. Siewert, Alexandra Bögli, Kathrin Strack, Alexander Harms, and Christoph Dehio. A Bartonella Effector Acts as Signaling Hub for Intrinsic STAT3 Activation to Trigger Anti-inflammatory Responses. *Cell Host and Microbe*, 27(3):476–485, 3 2020.
- [132] Melanie L. Yarbrough and Kim Orth. AMPylation is a new post-translational modification. *Nature Chemical Biology*, 5(6):378–379, 2009.
- [133] Dinesh V. Palanivelu, Arnaud Goepfert, Marcel Meury, Patrick Guye, Christoph Dehio, and Tilman Schirmer. Fic domain-catalyzed adenylation: Insight provided by the structural analysis of the type IV secretion system effector BepA. *Protein Science*, 20(3):492–499, 2011.
- [134] Lisa N. Kinch, Melanie L. Yarbrough, Kim Orth, and Nick V. Grishin. Fido, a novel ampylation domain common to fic, doc, and AvrB. *PLoS ONE*, 4(6):e5818, 6 2009.
- [135] A. G. Murzin. OB(oligonucleotide/oligosaccharide binding)-fold: Common structural and functional solution for non-homologous sequences. *EMBO Journal*, 12(3):861–867, 1993.
- [136] Vickery Arcus. OB-fold domains: A snapshot of the evolution of sequence, structure and function. *Current Opinion in Structural Biology*, 12(6):794–801, 12 2002.
- [137] Vishal Agrawal and K. Kishan. OB-fold: Growing Bigger with Functional Consistency. *Current Protein & Peptide Science*, 4(3):195–206, 3 2005.
- [138] Alexander Harms, Frédéric V. Stanger, and Christoph Dehio. Biological Diversity and Molecular Plasticity of FIC Domain Proteins. *Annual Review of Microbiology*, 70:341–360, 9 2016.
- [139] Alexander Wagner, Colin Tittes, and Christoph Dehio. Versatility of the BID domain: Conserved function as Type-IV-secretion-signal and secondarily

Bibliography

- evolved effector functions within bartonella-infected host cells. *Frontiers in Microbiology*, 10(MAY):921, 5 2019.
- [140] R Utsumi, Y Nakamoto, M Kawamukai, M Himeno, and T Komano. Involvement of cyclic AMP and its receptor protein in filamentation of an *Escherichia coli* fic mutant. *Journal of Bacteriology*, 151(2):807–812, 1982.
- [141] M. S. Brown, A. Segal, and E. R. Stadtman. Modulation of glutamine synthetase adenylation and deadenylation is mediated by metabolic transformation of the P II -regulatory protein. *Proceedings of the National Academy of Sciences of the United States of America*, 68(12):2949–2953, 1971.
- [142] H. S. Kingdon, B. M. Shapiro, and E. R. Stadtman. Regulation of glutamine synthetase. 8. ATP: glutamine synthetase adenylyltransferase, an enzyme that catalyzes alterations in the regulatory properties of glutamine synthetase. *Proceedings of the National Academy of Sciences of the United States of America*, 58(4):1703–1710, 1967.
- [143] Mark Hochstrasser. Origin and function of ubiquitin-like proteins. *Nature*, 458(7237):422–429, 3 2009.
- [144] Oliver Kerscher, Rachael Felberbaum, and Mark Hochstrasser. Modification of proteins by ubiquitin and ubiquitin-like proteins. *Annual Review of Cell and Developmental Biology*, 22:159–180, 10 2006.
- [145] Aymelt Itzen, Wulf Blankenfeldt, and Roger S. Goody. Adenylation: Renaissance of a forgotten post-translational modification. *Trends in Biochemical Sciences*, 36(4):221–228, 4 2011.
- [146] Simon Veyron, Gérald Peyroche, and Jacqueline Cherfils. FIC proteins: from bacteria to humans and back again. *Pathogens and disease*, 76(2), 3 2018.
- [147] Craig R. Roy and Shaeri Mukherjee. Bacterial FIC proteins AMP up infection. *Science Signaling*, 2(62), 3 2009.
- [148] Seema Mattoo, Eric Durrant, Mark J. Chen, Junyu Xiao, Cheri S. Lazar, Gerard Manning, Jack E. Dixon, and Carolyn A. Worby. Comparative analysis of *Histophilus somni* immunoglobulin-binding protein A (IbpA) with other Fic domain-containing enzymes reveals differences in substrate and nucleotide specificities. *Journal of Biological Chemistry*, 286(37):32834–32842, 9 2011.

- [149] Junyu Xiao, Carolyn A. Worby, Seema Mattoo, Banumathi Sankaran, and Jack E. Dixon. Structural basis of Fic-mediated adenylylation. *Nature Structural and Molecular Biology*, 17(8):1004–1010, 8 2010.
- [150] Valérie Campanacci, Shaeri Mukherjee, Craig R. Roy, and Jacqueline Cherfils. Structure of the Legionella effector AnkX reveals the mechanism of phosphocholine transfer by the FIC domain. *EMBO Journal*, 32(10):1469–1477, 5 2013.
- [151] Daniel Castro-Roa, Abel Garcia-Pino, Steven De Gieter, Nico A.J. Van Nuland, Remy Loris, and Nikolay Zenkin. The Fic protein Doc uses an inverted substrate to phosphorylate and inactivate EF-Tu. *Nature Chemical Biology*, 9(12):811–817, 12 2013.
- [152] Phi Luong, Lisa N. Kinch, Chad A. Brautigam, Nick V. Grishin, Diana R. Tomchick, and Kim Orth. Kinetic and structural insights into the mechanism of AMPylation by VopS Fic domain. *Journal of Biological Chemistry*, 285(26):20155–20163, 6 2010.
- [153] Tom D. Bunney, Ambrose R. Cole, Malgorzata Broncel, Diego Esposito, Edward W. Tate, and Matilda Katan. Crystal structure of the human, FIC-domain containing protein HYPE and implications for its functions. *Structure*, 22(12):1831–1843, 12 2014.
- [154] Philipp Engel, Arnaud Goepfert, Frédéric V. Stanger, Alexander Harms, Alexander Schmidt, Tilman Schirmer, and Christoph Dehio. Adenylylation control by intra-or intermolecular active-site obstruction in Fic proteins. *Nature*, 482(7383):107–110, 2 2012.
- [155] Frédéric V. Stanger, Björn M. Burmann, Alexander Harms, Hugo Aragão, Adam Mazur, Timothy Sharpe, Christoph Dehio, Sebastian Hiller, and Tilman Schirmer. Intrinsic regulation of FIC-domain AMP-Transferases by oligomerization and automodification. *Proceedings of the National Academy of Sciences of the United States of America*, 113(5):E529–E537, 2 2016.
- [156] Arnaud Goepfert, Frédéric V. Stanger, Christoph Dehio, and Tilman Schirmer. Conserved Inhibitory Mechanism and Competent ATP Binding Mode for Adenylyltransferases with Fic Fold. *PLoS ONE*, 8(5), 5 2013.

Bibliography

- [157] Abel Garcia-Pino, Nikolay Zenkin, and Remy Loris. The many faces of Fic: Structural and functional aspects of Fic enzymes. *Trends in Biochemical Sciences*, 39(3):121–129, 3 2014.
- [158] Arnaud Goepfert, Alexander Harms, Tilman Schirmer, and Christoph Dehio. Type II toxin-antitoxin loci: The fic family. In *Prokaryotic Toxin-Antitoxins*, pages 177–187. Springer-Verlag Berlin Heidelberg, 11 2013.
- [159] Anna K. H. Hirsch, Felix R. Fischer, and Francois Diederich. Phosphate Recognition in Structural Biology. *Angewandte Chemie International Edition*, 46(3):338–352, 1 2007.
- [160] Abel Garcia-Pino, Mikkel Christensen-Dalsgaard, Lode Wyns, Michael Yarmolinsky, Roy David Magnuson, Kenn Gerdes, and Remy Loris. Doc of prophage P1 is inhibited by its antitoxin partner Phd through fold complementation. *Journal of Biological Chemistry*, 283(45):30821–30827, 11 2008.
- [161] C. Dehio, C. Lanz, R. Pohl, P. Behrens, D. Bermond, Y. Piémont, K. Pelz, and A. Sander. *Bartonella schoenbuchii* sp. nov., isolated from the blood of wild roe deer. *International Journal of Systematic and Evolutionary Microbiology*, 51(4):1557–1565, 7 2001.
- [162] Debanu Das, S. Sri Krishna, Daniel McMullan, Mitchell D. Miller, Qingping Xu, Polat Abdubek, Claire Acosta, Tamara Astakhova, Herbert L. Axelrod, Prasad Burra, Dennis Carlton, Hsiu Ju Chiu, Thomas Clayton, Marc C. Deller, Lian Duan, Ylva Elias, Marc André Elsliger, Dustin Ernst, Julie Feuerhelm, Anna Grzechnik, Slawomir K. Grzechnik, Joanna Hale, Gye Won Han, Lukasz Jaroszewski, Kevin K. Jin, Heath E. Klock, Mark W. Knuth, Piotr Kozbial, Abhinav Kumar, David Marciano, Andrew T. Morse, Kevin D. Murphy, Edward Nigoghossian, Linda Okach, Silvy Oommachen, Jessica Paulsen, Ron Reyes, Christopher L. Rife, Natasha Sefcovic, Henry Tien, Christine B. Trame, Christina V. Trout, Henry Van Den Bedem, Dana Weekes, Aprilfawn White, Keith O. Hodgson, John Wooley, Ashley M. Deacon, Adam Godzik, Scott A. Lesley, and Ian A. Wilson. Crystal structure of the Fic (filamentation induced by cAMP) family protein SO4266 (gi|24375750) from *Shewanella oneidensis* MR-1 at 1.6 Å resolution. *Proteins: Structure, Function and Bioinformatics*, 75(1):264–271, 4 2009.

- [163] Lieven Buts, Jurij Lah, Minh Hoa Dao-Thi, Lode Wyns, and Remy Loris. Toxin-antitoxin modules as bacterial metabolic stress managers. *Trends in Biochemical Sciences*, 30(12):672–679, 12 2005.
- [164] Finbarr Hayes. Toxins-antitoxins: Plasmid maintenance, programmed cell death, and cell cycle arrest. *Science*, 301(5639):1496–1499, 9 2003.
- [165] Hyeilin Ham, Andrew R. Woolery, Charles Tracy, Drew Stenesen, Helmut Krämer, and Kim Orth. Unfolded protein response-regulated Drosophila Fic (dFic) protein reversibly AMPylates BiP chaperone during endoplasmic reticulum homeostasis. *Journal of Biological Chemistry*, 289(52):36059–36069, 2014.
- [166] Steffen Preissler, Cláudia Rato, Ruming Chen, Robin Antrobus, Shujing Ding, Ian M. Fearnley, and David Ron. AMPylation matches BiP activity to client protein load in the endoplasmic reticulum. *eLife*, 4(DECEMBER2015), 12 2015.
- [167] Anwesha Sanyal, Andy J. Chen, Ernesto S. Nakayasu, Cheri S. Lazar, Erica A. Zbornik, Carolyn A. Worby, Antonius Koller, and Seema Mattoo. A novel link between fic (filamentation induced by cAMP)-mediated adenylation/AMPylation and the unfolded protein response. *Journal of Biological Chemistry*, 290(13):8482–8499, 3 2015.
- [168] Steffen Preissler, Claudia Rato, Luke A. Perera, Vladimir Saudek, and David Ron. FICD acts bifunctionally to AMPylate and de-AMPylate the endoplasmic reticulum chaperone BiP. *Nature Structural and Molecular Biology*, 24(1):23–29, 1 2017.
- [169] Pavel Kielkowski, Isabel Y. Buchsbaum, Volker C. Kirsch, Nina C. Bach, Micha Drukker, Silvia Cappello, and Stephan A. Sieber. FICD activity and AMPylation remodelling modulate human neurogenesis. *Nature Communications*, 11(1):1–13, 12 2020.
- [170] Kathrin Pieves, Timo Glatzer, Alexander Harms, Alexander Schmidt, and Christoph Dehio. An experimental strategy for the identification of AMPylation targets from complex protein samples. *Proteomics*, 14(9):1048–1052, 5 2014.

Bibliography

- [171] Emil Dedic, Husam Alsarraf, Ditte Hededam Welner, Ole Østergaard, Oleg I. Klychnikov, Paul J. Hensbergen, Jeroen Corver, Hans C. Van Leeuwen, and René Jørgensen. A novel fic (filamentation induced by cAMP) protein from *Clostridium difficile* reveals an inhibitory motif-independent adenylation/AMPylation mechanism. *Journal of Biological Chemistry*, 291(25):13286–13300, 6 2016.
- [172] Matthias Truttmann and Hidde Ploegh. In vitro AMPylation Assays Using Purified, Recombinant Proteins. *BIO-PROTOCOL*, 7(14), 2017.
- [173] Robert W. Pringle. The scintillation counter. *Nature*, 166(4209):11–14, 1950.
- [174] Sean C Taylor, Thomas Berkelman, Geetha Yadav, and Matt Hammond. A defined methodology for reliable quantification of western blot data. *Molecular Biotechnology*, 55(3):217–226, 2013.
- [175] Taxiarchis P. Geladopoulos, Theodore G. Sotiroidis, and Athanasios E. Evangelopoulos. A malachite green colorimetric assay for protein phosphatase activity. *Analytical Biochemistry*, 192(1):112–116, 1991.
- [176] Elia Agustoni, Raphael Dias Teixeira, Markus Huber, Susanne Flister, Sebastian Hiller, and Tilman Schirmer. Acquisition of enzymatic progress curves in real time by quenching-free ion exchange chromatography. *Analytical Biochemistry*, 639(December 2021):114523, 2022.
- [177] Eric R. Geertsma and Raimund Dutzler. A versatile and efficient high-throughput cloning tool for structural biology. *Biochemistry*, 50(15):3272–3278, 4 2011.
- [178] John S. Reece-Hoyes and Albertha J.M. Walhout. Gateway recombinational cloning. *Cold Spring Harbor Protocols*, 2018(1):1–6, 1 2018.
- [179] Nikolaus Dietz, Markus Huber, Isabel Sorg, Arnaud Goepfert, Alexander Harms, Tilman Schirmer, and Christoph Dehio. Structural basis for selective AMPylation of Rac-subfamily GTPases by Bartonella effector protein 1 (Bep1). *Proceedings of the National Academy of Sciences*, 118(12), 3 2021.
- [180] Schrödinger, LLC. The {PyMOL} Molecular Graphics System, Version ~1.8. 11 2015.

- [181] Arlet G. Kurkchubasche, Julie A. Panepinto, Thomas F. Tracy, Gail W. Thurman, and Daniel R. Ambruso. Clinical features of a human Rac2 mutation: A complex neutrophil dysfunction disease. *Journal of Pediatrics*, 139(1):141–147, 2001.
- [182] Daniel R. Ambruso, Cindy Knall, Amy N. Abell, Julie Panepinto, Arlet Kurkchubasche, Gail Thurman, Carolina Gonzalez-Aller, Andrew Hiestler, Martin DeBoer, Ronald J. Harbeck, Ryan Oyer, Gary L. Johnson, and Dirk Roos. Human neutrophil immunodeficiency syndrome is associated with an inhibitory Rac2 mutation. *Proceedings of the National Academy of Sciences of the United States of America*, 97(9):4654–4659, 4 2000.

6 Acknowledgments

6 Acknowledgments

First and foremost, I would like to thank my two supervisors Prof. Christoph Dehio and Prof. Tilman Schirmer for the opportunity to work on this exciting and challenging project and for their guidance during my PhD.

I would also like to thank Timm Maier and Gudula Schmidt for the stimulating discussions and for giving me new ideas and hints while I was working on my project.

I am also very grateful to Niko Dietz and Isa Sorg for always having a helping hand (or an open ear) and teaching me many new tricks that I would never have thought of before.

Special thanks to Elia, Johanna, Raphael, Stefanie, Firas, Lena, Alex, Katja, Jarek, Maren, Carsten, Sabrina, Simon, Selma and to all other former and current members of the Dehio and Schirmer group for their constant support and the great working atmosphere!

My gratitude includes all members of the Infection Biology and Structure Biology focal areas, in particular the Maier group who gave me the feeling of being part of a 3rd research group at times.

Many thanks to Lisa, Kai, Maria, Rike, Ole, Michi and many others who have grown close to my heart since I arrived in Basel! I will always remember our great mountain expeditions and some crazy parties.

Finally, I would like to thank my parents, my aunt Gabi and my grandmother Anna, who have had a big impact on me since my childhood. Everything I have accomplished was only possible thanks to you!

7 Curriculum Vitae

Curriculum Vitae

Personal Information

Name: Markus Huber
Date and Place of Birth: July 15th 1986, Amstetten, Austria
Email: Markus.Max.Huber@protonmail.com

Professional Experience

2022 – present **Scientific Consultant**, Genedata, Switzerland
Tasks: Requirement analysis (complex scientific workflows), customer guidance and consulting (large data management solutions), support and training for delivered solutions, driving data migration projects, scientific and technical support for business development

2016 – 2022 **PHD/Postdoc in the Groups of Christoph Dehio and Tilman Schirmer**, Biozentrum, University of Basel, Switzerland
Tasks: Research in the fields of Infection Biology (Dehio) and Structural Biology (Schirmer, main field) on structure and function of bacterial toxins. Focus on in vitro protein experiments (design, expression, purification, characterization)

2016 **Application specialist at labors.at**, Vienna, Austria
Tasks: Set-up and maintenance of automated analytical tests (blood, urine, feces), Development and administration of In-house and 3rd-party (medat) LIMS solutions

2013 – 2016 **Tutor at the “Vienna Open Lab”**, Austria
Tasks: Conduction of courses in basic chemistry and Molecular Biology (states of matter, DNA extraction, PCR, Gel electrophoresis)

2007 – 2009 **Software developer at “3 Banken IT”**, Linz, Austria
Tasks: Development and maintenance of software (backend and bank internal frontend) for domestic (SEPA) and foreign payments

Education

2016 – 2021 **Ph.D. thesis in Structural Biology**, Biozentrum, University of Basel, Switzerland
Supervised by Prof. Tilman Schirmer and Prof. Christoph Dehio

	<p><i>Thesis title: "Structure and function of Bartonella Effector protein 1: Target and interdomain interactions"</i></p>
2012 – 2015	<p>M.Sc. thesis in Molecular Biology (Cell Biology), University Vienna / MFPL, Austria Supervised by Prof. Friedrich Propst in collaboration with Prof. Robert Konrat</p> <p><i>Thesis title: "Structural features of the MAP1b light chain 1 microtubule binding domain" (http://othes.univie.ac.at/35471/)</i></p>
2009 – 2012	<p>Undergraduate studies in Biology (Molecular Biology), University Vienna / MFPL, Austria</p>
2001 – 2006	<p>HTBLA Leonding, Austria majoring in electronic data processing and organization</p>

Other Experience

Languages	German (native), English (fluent)
Software	MS Windows, MacOS, Linux (including bash), Office (MS, Libre/Open, Google), Adobe Photoshop/Illustrator, GIMP, Latex, C/C++/C# (dwindling), Java (dwindling), SQL/PLSQL, Python, Standard Structural Biology software (CCP4 suite, Phenix suite, Coot, XDS, Pymol, etc.)
Interpersonal	Tutor for graduate students in Infection Biology and Structural Biology, Teacher for kids@science, Sports climbing instructor, Ph.D. representative (social activities)

Oral and Poster Presentation

2021	<p>Poster presentation at the European Workshop on Bacterial Protein Toxins (ETOX), virtual</p> <p><i>Title: Full-length structure of a multi-domain effector protein from Bartonella reveals a new conserved interdomain fold</i></p>
2020	<p>Oral presentation at the AMPylationPLUS conference, virtual</p> <p><i>Title: Structural basis for selective AMPylation of Rac subfamily GTPases by "Bartonella effector protein 1"</i></p>
2020	<p>Poster presentation at the Biozentrum Symposium, Basel, Switzerland</p> <p><i>Title: Online Ion-Exchange Chromatography to Monitor Enzymatic Reactions</i></p>

Markus Huber

2019 **Poster presentation at the European Crystallographic Meeting,**
Vienna, Austria
*Title: The BEP1 Fic-domain: Unravelling the mechanism of narrow target
selectivity towards Rac GTPases*

2019 **Oral presentation at the European Workshop on Bacterial
Protein Toxins (ETOX),** Davos, Switzerland
*Title: The Bep1 Fic-domain: Unravelling the mechanism of narrow target
selectivity towards Rac GTPases*

Publications

2021 ***Acquisition of enzymatic progress curves in real time by
quenching-free ion exchange chromatography,*** Analytical
Biochemistry
<https://doi.org/10.1016/j.ab.2021.114523>

Elia Agustoni, **Markus Huber**¹, Raphael DiasTeixeira¹, Susanne
Flister, Sebastian Hiller, and Tilman Schirmer.

¹ equal contribution

2021 ***Structural basis for selective AMPylation of Rac-subfamily
GTPases by Bartonella effector protein 1 (Bep1),*** PNAS
<https://doi.org/10.1073/pnas.2023245118>

Markus Huber¹, Nikolaus Dietz¹, Isabel Sorg, Arnaud Goepfert,
Alexander Harms, Tilman Schirmer, and Christoph Dehio.

¹ equal contribution